NASA CR-165239

NASA

RECTANGULAR BEAM (5 × 40 cm) MULTIPOLE ION SOURCE

by Curtis M. Haynes

PREPARED FOR

LEWIS RESEARCH CENTER

NATIONAL AERONAUTICS AND SPACE ADMINISTRATION

GRANT 3086

December 1980

Approved by

Harold R. Kaufman

and

Raymond S. Robinson

Department of Physics
Colorado State University
Fort Collins, Colorado

1. Report No.	2. Government Accession No.	3. Recipient's Catalog No.
CR 165239		

4. Title and Subtitle	5. Report Date
Rectangular Beam (5 × 40 cm) Multipole Ion Source	November 1979
	6. Performing Organization Code

7. Author(s)	8. Performing Organization Report No.
Curtis M. Haynes	
	10. Work Unit No.

9. Performing Organization Name and Address	11. Contract or Grant No.
Department of Physics Colorado State University Fort Collins, Colorado 80523	NSG-3086
	13. Type of Report and Period Covered

12. Sponsoring Agency Name and Address	13. Type of Report and Period Covered
National Aeronautics and Space Administration Washington, DC 20546	Contract Report
	14. Sponsoring Agency Code

15. Supplementary Notes

Grant Manager - Michael J. Mirtich, Jr.
NASA Lewis Research Center, Cleveland, Ohio 44135

This report is a reproduction of the M.S. thesis of Curtis M. Haynes

16. Abstract

A 5 × 40 cm rectangular-beam ion source was designed and fabricated. A multipole field configuration was used to facilitate design of the modular rectangular chamber, while a three-grid ion optics system was used for increased ion current densities.

For the multipole chamber, a magnetic integral of 5.6×10^{-5} Tesla-m was used to contain the primary electrons. This integral value was reduced from the initial design value, with the reduction found necessary for discharge stability. The final value of magnetic integral resulted in discharge losses at typical operating conditions which ranged from 600 to 1000 eV/ion, in good agreement with the design value of 800 eV/ion.

The beam current density at the ion optics was limited to about 3.2 mA/cm^2 at 500 eV and to about 3.5 mA/cm^2 at 1000 eV. The design value of 6 mA/cm^2 at 500 eV was not achieved. Some reduction from optimum is usually expected for large ion optics, due to both nonuniform ion current and tolerance effects over the large beam dimensions. The large reduction from 6 to 3.2-3.5 mA/cm^2 probably indicates additional effects due to grid thermal warping which tended to increase accelerator and decelerator grid impingement currents and grid arcing. The current densities of 3.2 and 3.5 mA/cm^2 were obtained at net-to-total voltage ratios of 0.33 and 0.67. The larger current density at 1000 eV and R = 0.67 was close to an impingement limit, but was actually limited by the accelerator power supply capability.

The use of multiple rectangular-beam ion sources to process wider areas than would be possible with a single source (∿40 cm) was also studied. Beam profiles were surveyed at a variety of operating conditions and the results of various amounts of beam overlap calculated. In all cases investigated a very uniform ion beam resulted with the most uniform coverage being obtained using a 0-2 cm overlap. The maximum departure from uniform processing at optimum overlap was found to be ±15%. This small departure was felt to be very good for a chamber length of 45 cm. If a higher degree of uniformity is required in the long dimension the chamber could be made longer to decrease end affects.

17. Key Words (Suggested by Author(s))	18. Distribution Statement
Ion Beams Ion Etching Ion Source Sputtering	Unclassified - Unlimited

N81-24877#

19. Security Classif. (of this report)	20. Security Classif. (of this page)	21. No. of Pages	22. Price*
Unclassified	Unclassified		

* For sale by the National Technical Information Service, Springfield, Virginia 22161

TABLE OF CONTENTS

Chapter		Page
I.	INTRODUCTION	1
II.	ION OPTICS AND SOURCE DESIGN	5
	Design Criteria	5
	Two-grid approach	19
	Three-grid approach	22
	Discharge Chamber Design	25
	Discharge performance considerations	25
	Discharge chamber dimensions	26
	Magnetic field configuration	36
	Anode area limitation	43
	Discharge chamber performance	44
	Cathodes	44
III.	FABRICATION	45
	Grids	45
	Discharge Chamber	45
	Final Assembly	48
IV.	RECTANGULAR ION SOURCE PERFORMANCE	50
	Large Magnetic Integral	50
	Small Magnetic Integral	52
	Discharge-Loss Calculations	55
	High Perveance Grid Operation	58
	Ion Beam Profile	68
V.	USE OF MULTIPLE SOURCES FOR WIDE PROCESSING PATHS	75
IV.	CONCLUSION	94
APPENDIX		96
REFERENCES		98
DISTRIBUTION LIST		100

LIST OF FIGURES

Figure		Page
1-1.	Schematic of overlapping ion beam processing configurations	2
2-1.	Ion optics configurations (from Refs. 22 and 23): (a) Two-grid accelerator geometry; (b) Three-grid accelerator geometry	8
2-2.	Potential variation through the screen and accelerator grids for an ion optics system (from Ref. 22)	9
2-3.	Effect of screen hole diameter on Ar ion beam divergence for a two-grid system (from Ref. 22)	11
2-4.	Effect of accelerator hole diameter ratio on Ar ion beam divergence for a two-grid system (from Ref. 22)	12
2-5.	Effect of screen grid thickness ratio on Ar ion beam divergence for a two-grid system (from Ref. 22)	13
2-6.	Effect of accelerator grid thickness ratio on Ar ion beam divergence for a two-grid system (from Ref. 22)	14
2-7.	Effect of the net-to-total voltage ratio (R) on Ar ion beam divergence for a two-grid system (from Ref. 22)	15
2-8.	Effect of decelerator grid hole diameter on Ar ion beam divergence for a three-grid system (from Ref. 23)	16
2-9.	Effect of decelerator gap ratio on Ar ion beam divergence for a three-grid system (from Ref. 23). R = 0.3	17
2-10.	Effect of net-to-total voltage ratio (R) on minimum Ar ion beam divergence of two and three-grid systems (from Ref. 23)	24
2-11.	Multipole discharge chamber. Dashed line shows assumed primary electron region outer surface	28
2-12.	Theoretical discharge loss versus ion chamber depth for a rectangular source	33
2-13.	Theoretical discharge loss versus required chamber pressure for a stable discharge at various values of n_p/n_m	34
2-14.	Rectangular ion source cross-section	37
2-15.	Magnetic field integral needed in front of an anode to deflect primary electrons	39

Figure Page

2-16. Magnetic field strength for a corner pole piece section... 41

2-17. Magnetic field strength for an end pole piece section (next to the ion optics)..... 42

3-1. Photograph of completed rectangular ion source without ion optics..... 47

3-2. Photograph of completed rectangular ion source with ion optics and ground screen..... 49

4-1. Discharge loss for two screen grid thicknesses at the larger value of magnetic field integral..... 51

4-2. Discharge loss for the two different magnetic field integrals at 2×10^{-4} Torr..... 53

4-3. Discharge loss for the two different magnetic integrals at 3×10^{-4} Torr..... 54

4-4. Discharge loss for various pressures at the smaller magnetic field integral..... 56

4-5. Power supply configurations for the rectangular ion source..... 57

4-6. Discharge loss for the two different power supply configurations and the smaller magnetic field integral.. 59

4-7. Discharge loss versus beam current for different total voltages (V_T), 360 mA-equiv. Ar flow rate..... 60

4-8. Discharge loss for $V_T \sim 1500$ V and F = 360 mA-equiv..... 61

4-9. Discharge loss for $V_T \sim 1000$ V and F = 360 mA-equiv..... 62

4-10. Discharge loss for $V_T \sim 750$ V and F = 360 mA-equiv..... 63

4-11. Discharge loss versus beam current for different total voltages (V_T), 800 mA-equiv. Ar flow rate..... 64

4-12. Discharge loss for $V_T \sim 1500$ V and F = 800 mA-equiv..... 65

4-13. Discharge loss for $V_T \sim 1000$ V and F = 800 mA-equiv..... 66

4-14. Discharge loss for $V_T \sim 750$ V and F = 800 mA-equiv..... 67

4-15. Ion beam current density profile taken along the 40 cm direction at a distance of 10 cm from the grids..... 72

4-16. Ion beam current density profile taken across the 5 cm direction at a distance of 10 cm from the grids..... 73

Figure Page

4-17. Ion beam current density profiles taken across the 5 cm direction at a distance of 10 cm from the grids at high total beam currents..... 74

5-1. Probe placement for beam profile measurements..... 76

5-2. Integrated beam current measured along the 40 cm direction..... 78

5-3. Ion source integrated beam current profile with the grid ends separated by 1.0 cm..... 79

5-4. Ion source integrated beam current profile at no overlap.. 80

5-5. Overlapped ion source integrated beam current profile at 1.0 cm overlap..... 81

5-6. Overlapped ion source integrated beam current profile at 2.0 cm overlap..... 82

5-7. Integrated beam current profile for the best overlap position at 1×10^{-4} Torr and R = 0.90..... 83

5-8. Integrated beam current profile for the best overlap position at 6×10^{-5} Torr and R = 0.90..... 85

5-9. Integrated beam current profile for the best overlap position at 6×10^{-4} Torr and R = 0.90..... 86

5-10. Integrated beam current profile for the best overlap position at 6×10^{-5} Torr and R = 0.67..... 87

5-11. Integrated beam current profile for the best overlap position at 1×10^{-4} Torr and R = 0.67..... 88

5-12. Integrated beam current profile for the best overlap position at 6×10^{-4} Torr and R = 0.67..... 89

5-13. Integrated beam current profile for the best overlap position at 6×10^{-5} Torr and R = 0.50..... 90

5-14. Integrated beam current profile for the best overlap position at 1×10^{-4} Torr and R = 0.50..... 91

5-15. Integrated beam current profile for the best overlap position at 6×10^{-4} Torr and R = 0.50..... 92

LIST OF TABLES

Table Page

4-1. Maximum Normalized Perveance per Hole for Various Grid Potentials for a Flow Rate of 360 mA-equiv..... 69

4-2. Maximum Normalized Perveance per Hole for Various Grid Potentials for a Flow Rate of 800 mA-equiv..... 70

5-1. Maximum Deviation in Integrated Beam Current for Overlapped Rectangular Ion Sources..... 84

I. INTRODUCTION

Ion beam machining is a technique that is widely used for material processing. Broad-beam, electron-bombardment ion sources have been used for these industrial applications because they are capable of uniform, high density ion beams that are readily controlled. A wide range of working gases, both inert and reactive, may also be used with broad-beam ion sources in these applications.

In the past, cylindrical ion sources similar to those developed for the space electric propulsion program[1] have been used for material processing. However, because of the circular ion beam cross-section, the batch method of material sputtering must normally be used for processing with such a source. However, if a uniform rectangular ion beam were used for material processing, this processing could be done continuously. For example, by means of a conveyor belt passing through the uniform ion beam at a constant speed (u), samples would receive a constant ion dose. Also, rectangular beams could be overlapped to effectively produce one ion beam larger than the beam that could be generated by a single ion source. This concept is indicated in Fig. 1-1 where u is the material speed through the ion beam.

A 40 × 5 cm rectangular ion beam was selected to both fit in the existing vacuum facility and to be long enough to demonstrate capability for wide path processing. A uniform ion beam was of particular interest for the 40 cm direction so that materials passing through the ion beam in the short dimension would receive equal ion doses regardless of the path location. A high beam current density was required to decrease processing time and a well-collimated beam would tend to decrease the contamination of both the substrate and the ion source.

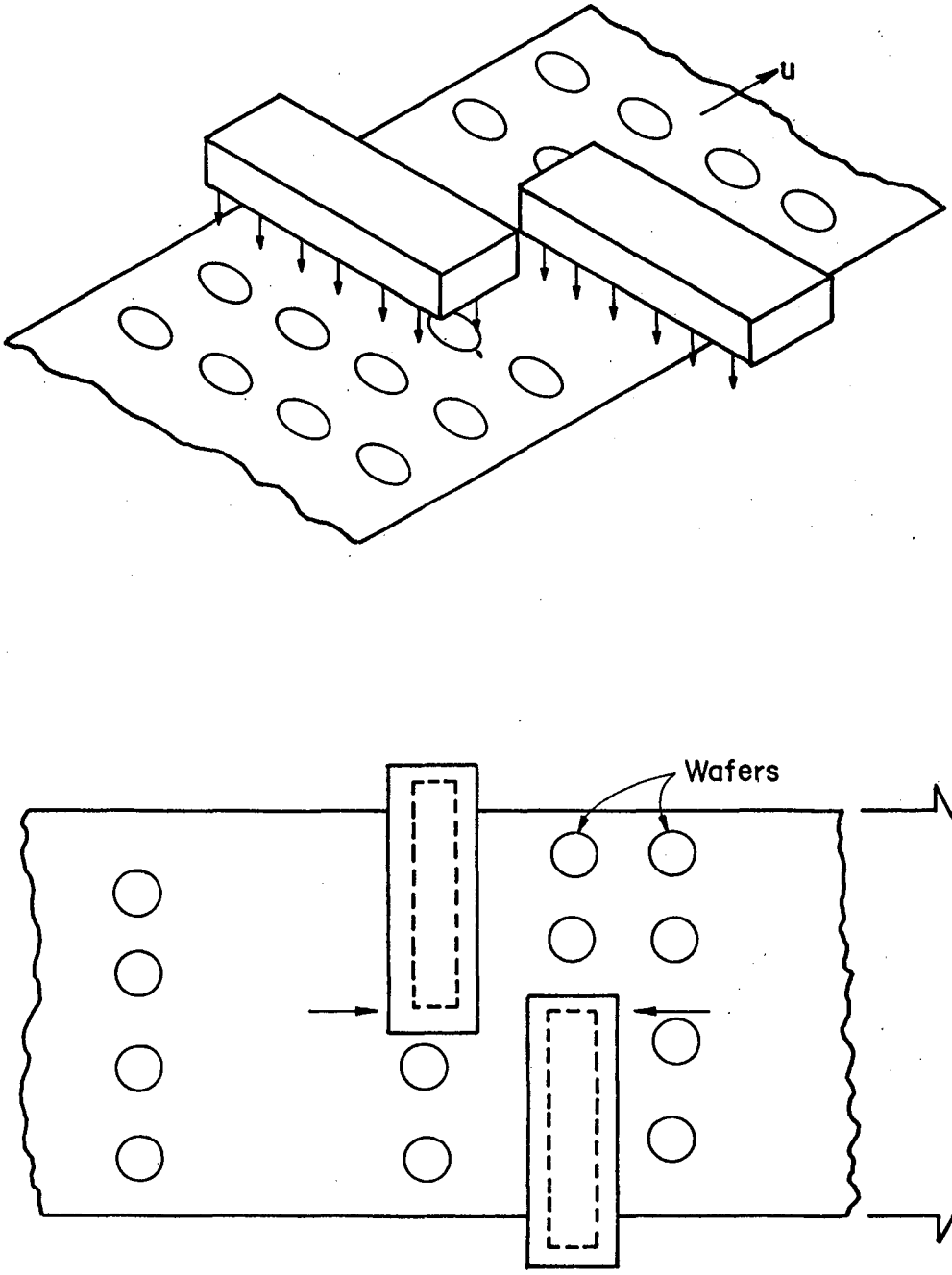

Fig. 1-1. Schematic of overlapping ion beam processing configurations.

Both two and three-grid ion optics systems were considered. The multipole type electron-bombardment ion source was selected for the following reasons. First, the multipole discharge chamber shape is not constrained by any need for a magnetic field throughout the discharge chamber. That is, the multipole approach is essentially a discharge-chamber wall design, as opposed to the discharge-chamber volume design used in most other approaches. A multipole discharge chamber may therefore be easily adapted to a rectangular shape with essentially no magnetic circuit design changes. Second, the multipole chamber has proven to be reliable,[1] requiring a minimum of maintenance for continued operation. Third, this type of chamber design is relatively inexpensive to construct and use. Fourth, the multipole ion chamber is capable of producing very uniform, high density, well collimated ion beams for industrial use.[2,3]

Past experience with cylindrical multipole electron-bombardment ion source fabrication[1,2,4] has produced a body of knowledge that has largely supplanted the previous cut-and-try approach to ion source design.[1] This enhanced understanding of plasma processes was used, along with experimental ion optics data,[5-8] to design and fabricate a rectangular ion source capable of operating over a wide range of conditions suitable for various processing applications.[9]

The performance of the ion source was measured for different operating conditions. Two values of magnetic field integrals for primary electron containment (as well as different power supply configurations) were investigated and discharge losses compared. The extracted ion beam was studied at various total voltages and pressures. Ion beam profiles were taken and compared for uniformity.

As a final section in this thesis, the use of multiple ion sources for wide path processing was investigated by combining beam profiles which were overlapped by different amounts. The overlap positions were optimized and compared for different operating conditions.

II. ION OPTICS AND SOURCE DESIGN

Design Criteria

A uniform rectangular ion beam is desirable for continuous processing of wide paths. Rectangular-beam sources may also be placed side by side for processing areas even wider than possible using a single ion source. A well-collimated ion beam is also desirable. In this way large ion-source-to substrate distances might be maintained that will tend to decrease the rate of contamination of both the ion source and the substrate material being sputtered. High current densities are also advantageous for increasing the processing speeds of materials.

A grid ion extraction area of 40 × 5 cm was selected as the largest that could be conveniently used with the available 46 cm diameter vacuum facility and existing power supplies. A 500 eV ion beam energy was selected as a design criterion although energies as high as 1000 eV and as low as 250 eV were experimentally investigated for ion source performance. A 500 eV ion beam energy is a good compromise between material removal and heating and/or damage to the substrate. The sputter yields of materials such as PbTe, GaAs, Ge, Si and SiC increase rapidly with ion energy up to about 300-500 eV.[4,10,11] However, at higher ion energies the sputter yields increase much more slowly. It is generally easier to obtain a given current density at higher ion energies than at lower ion energies. At the design value of 500 eV the source was optimized to assure a high current density.

Ion Optics Design

Space charge solutions for an accelerator system have been found by solving Poisson's equation,

$$\nabla^2 V = -\rho/\varepsilon_o \ , \tag{2-1}$$

where V is the electrostatic potential between two grids and ρ is the charge density of the charged particle flow. The solution is obtainable for flow between two planar electrodes with zero electric field at the plane of charged particle origin with no particle reflection and is called Child's Law,

$$j = \frac{4\varepsilon_o}{9}\left(\frac{2q}{m}\right)^{1/2}\frac{\Delta V^{3/2}}{\ell^2} \ , \tag{2-2}$$

where j is the current density, q/m is the particle charge to mass ratio, ΔV is the potential difference between the planar electrodes, and ℓ is the separation of these same two planes. In most ion optics, the ions are accelerated in discrete beamlets, with each beamlet passing through a single circular aperture of the ion optics. This beamlet current per hole (J_B) may be approximated with the Child's Law current density (j) by

$$J_B = (\pi/4)\ d^2\ j \ , \tag{2-3}$$

where d is the diameter of the aperture. Substituting this expression into Child's Law results in

$$J_B = \frac{\pi\varepsilon_o d^2}{9}\left(\frac{2q}{m}\right)^{1/2}\ \frac{V^{3/2}}{\ell^2} \ . \tag{2-4}$$

Experimental data from accelerator grid systems for comparison has shown that the best approximation is obtained when d is the screen hole diameter (d_s), V is the total voltage (V_t) and ℓ is the effective acceleration distance (ℓ_e). See Fig. 2-1 and 2-2 for definitions of these parameters. Substituting these new variables and rearranging terms in Eq. (2-4) result in

$$\frac{J_B}{V_t^{3/2}}\left(\frac{\ell_e}{d_s}\right)^2 = \frac{\pi\varepsilon_o}{9}\left(\frac{2q}{m}\right)^{1/2}, \tag{2-5}$$

where the left hand side is the normalized perveance per hole and has a maximum theoretical value of 6.79×10^{-9} $A/V^{3/2}$ for Ar working gas. The effective acceleration length (ℓ_e) for circular apertures is defined[5] as

$$\ell_e^2 = \ell_g^2 + \frac{d_s^2}{4}, \tag{2-6}$$

where ℓ_g is the grid separation distance (see Fig. 2-1). The normalized perveance per hole is the measure of an accelerator system's ability to extract the maximum ion current per hole for the minimum total accelerating voltage.[6] The normalized perveance is used herein to estimate the performance a particular grid set can offer for ion beam extraction.

An accelerator hole diameter equal to the screen hole diameter will result in substantial accelerator grid impingement being encountered at a normalized perveance of about 6.79×10^{-9} $A/V^{3/2}$ for a single aperture utilizing Ar working gas (value from Eq. (2-5)). Lower values of normalized perveance are usually of interest in practical applications, however. For example, higher beam collimation is usually obtained at

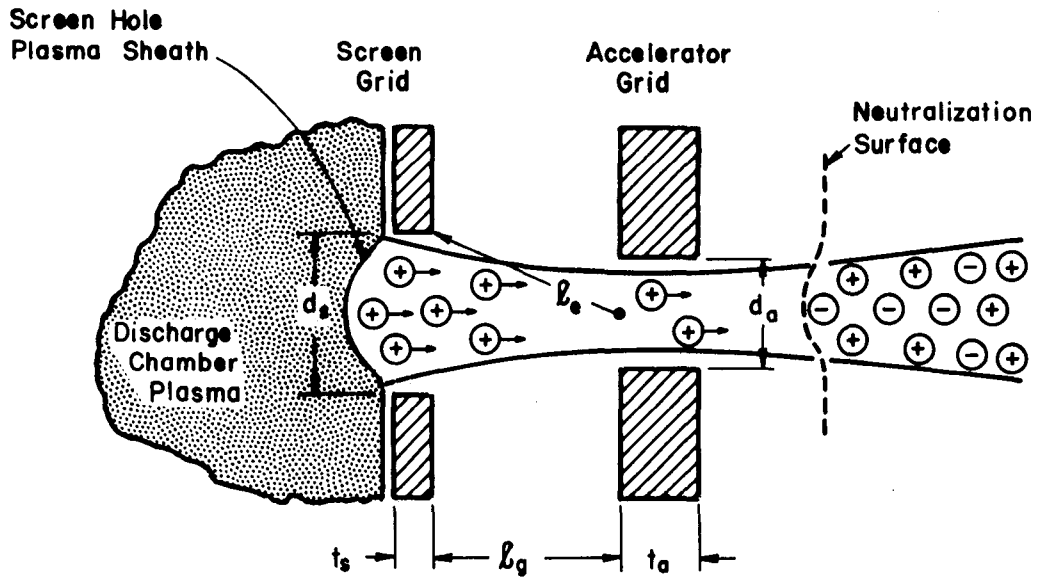

(a) Two-grid accelerator geometry.

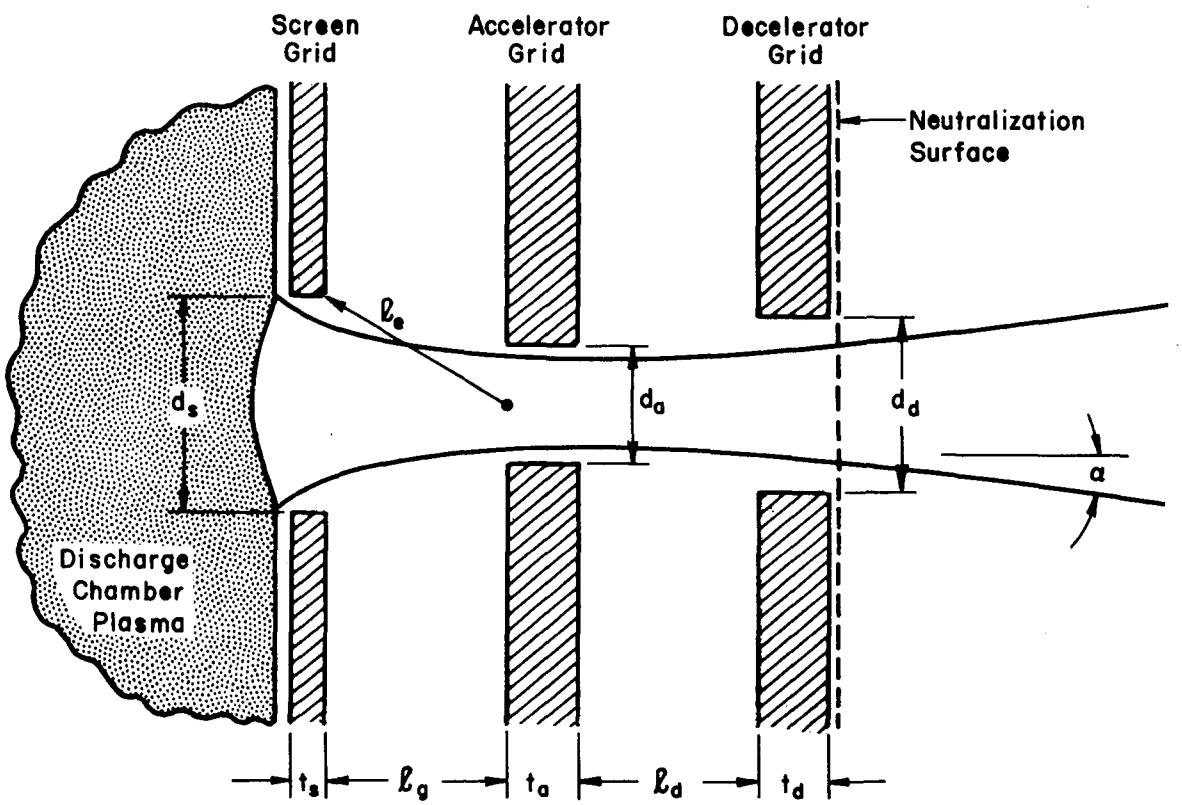

(b) Three-grid accelerator geometry.

Fig. 2-1. Ion optics configurations (from Ref. 22 and 23).

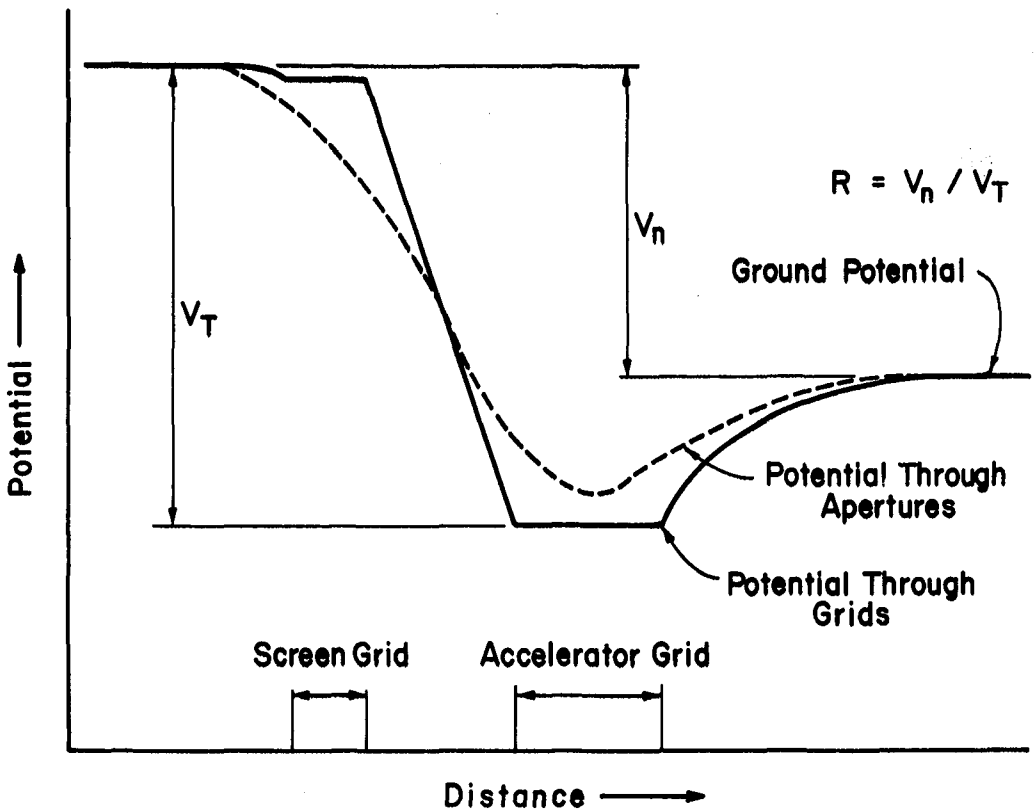

Fig. 2-2. Potential variation through the screen and accelerator grids for an ion optics system (from Ref. 22).

lower normalized perveances. Also, the ratio of neutral loss to extracted beam current is increased by using smaller accelerator holes, but smaller accelerator holes also result in grid impingement limiting the beamlet current to lower values.

Two and three-grid ion optics (Fig. 2-1) have been experimentally investigated by Aston.[6,7] The ion optics data of Aston are presented graphically in Figs. 2-3 through 2-9, in terms of the ion beam divergence angle α (see Fig. 2-1) and the normalized perveance (Eq. (2-5)). The design used herein was largely based on the experimental results shown in Figs. 2-3 through 2-9.

For industrial ion source applications a highly collimated ion beam is generally desired. Similar values of the ion beam divergence half-angle α (defined herein as the angle enclosing 95% of the total integrated beam current[6]) were therefore selected when comparing the current capabilities of different designs. A minimum half-angle of 10 degrees is a moderate value for this design if 500 eV ions are assumed.

For any ion optics considered, a suitable grid material should be used. The material chosen should have a low sputter yield, a low thermal expansion coefficient to minimize misalignment during operation, and the material should be easy to machine. Molybdenum and graphite were both considered.

Many ion sources used as thrusters in electric space propulsion are equipped with molybdenum dished grids. These grids are capable of maintaining larger span-to-gap ratios than flat carbon grids, due to a decreased sensitivity to thermal expansion.[4,12] Although molybdenum is very strong and has a fairly low coefficient of thermal expansion, the costs of fabrication for dished grids are quite high. Also, there is no

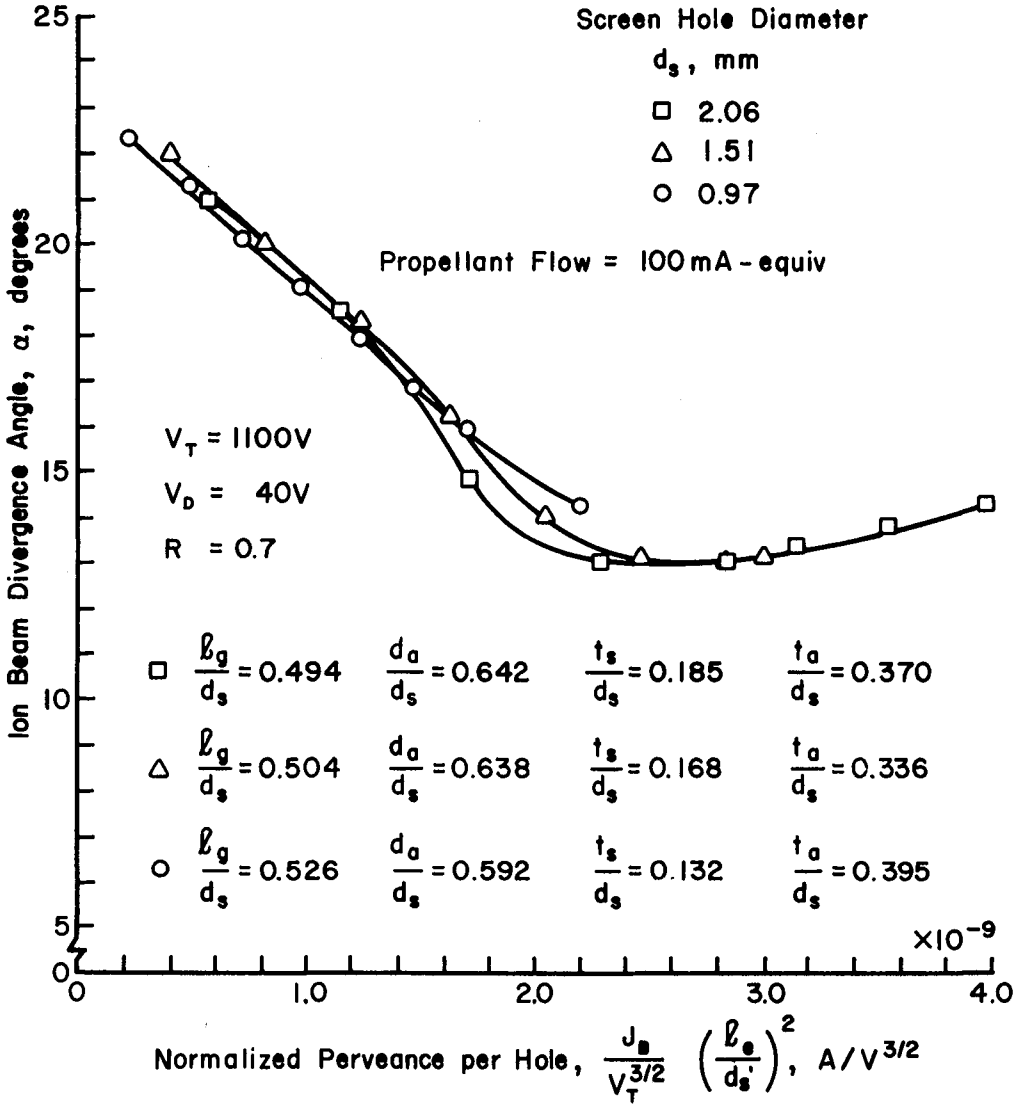

Fig. 2-3. Effect of screen hole diameter on Ar ion beam divergence for a two-grid system (from Ref. 22).

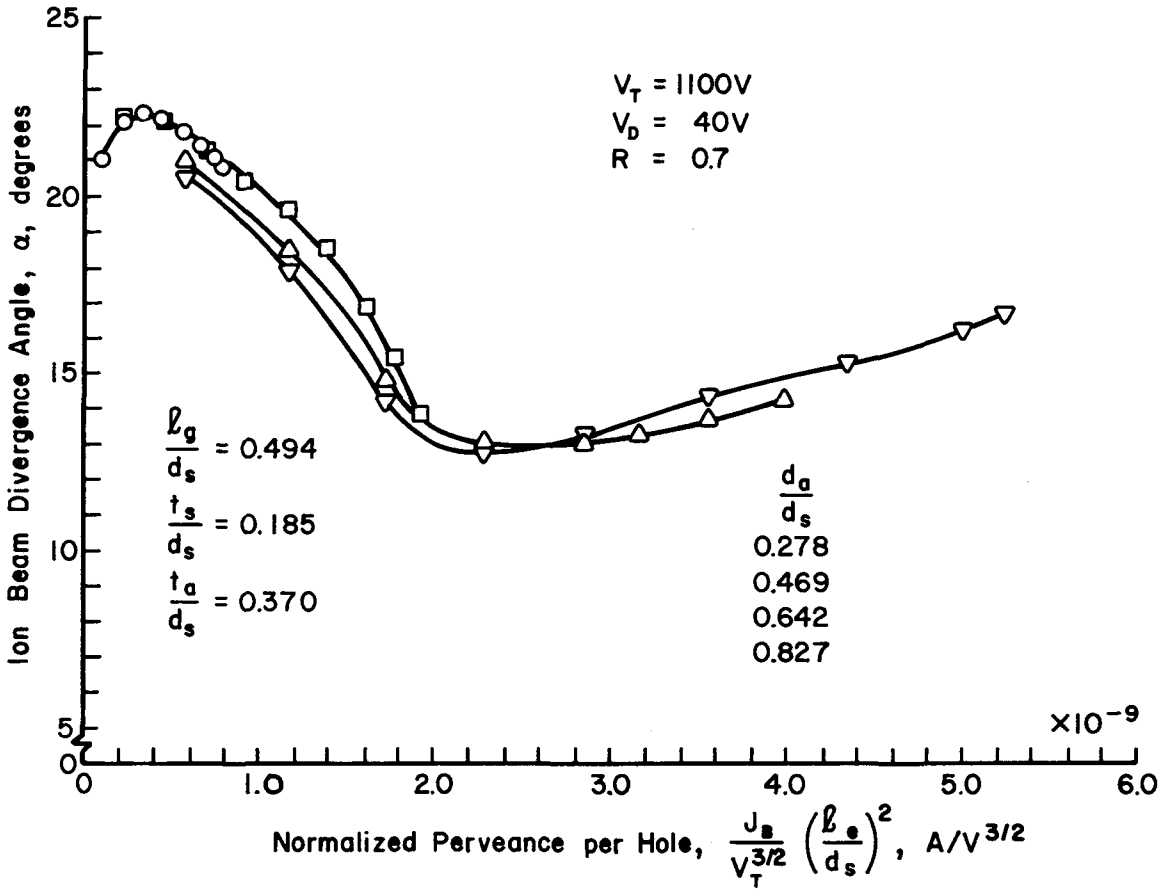

Fig. 2-4. Effect of accelerator hole diameter ratio on Ar ion beam divergence for a two-grid system (from Ref. 22).

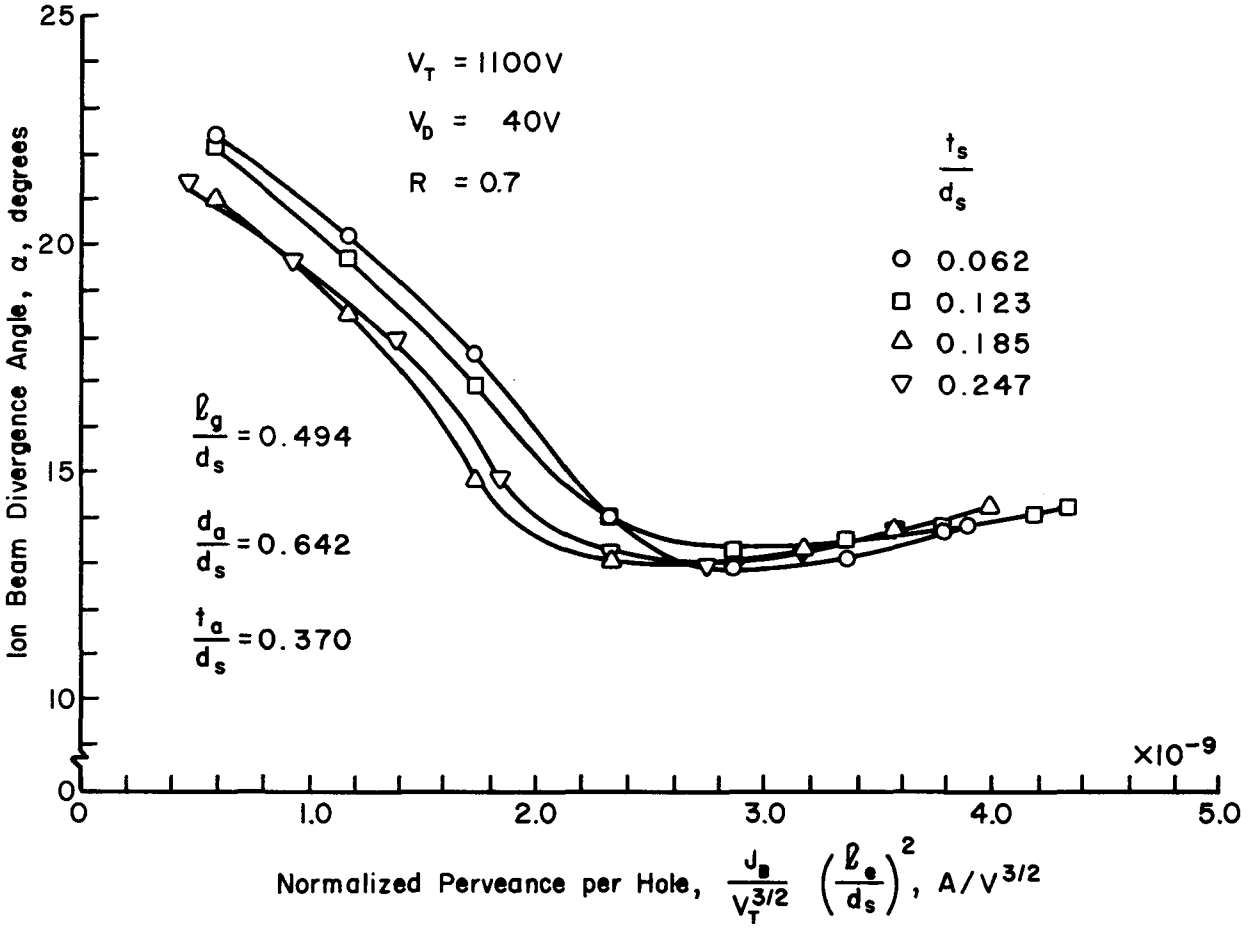

Fig. 2-5. Effect of screen grid thickness ratio on Ar ion beam divergence for a two-grid system (from Ref. 22).

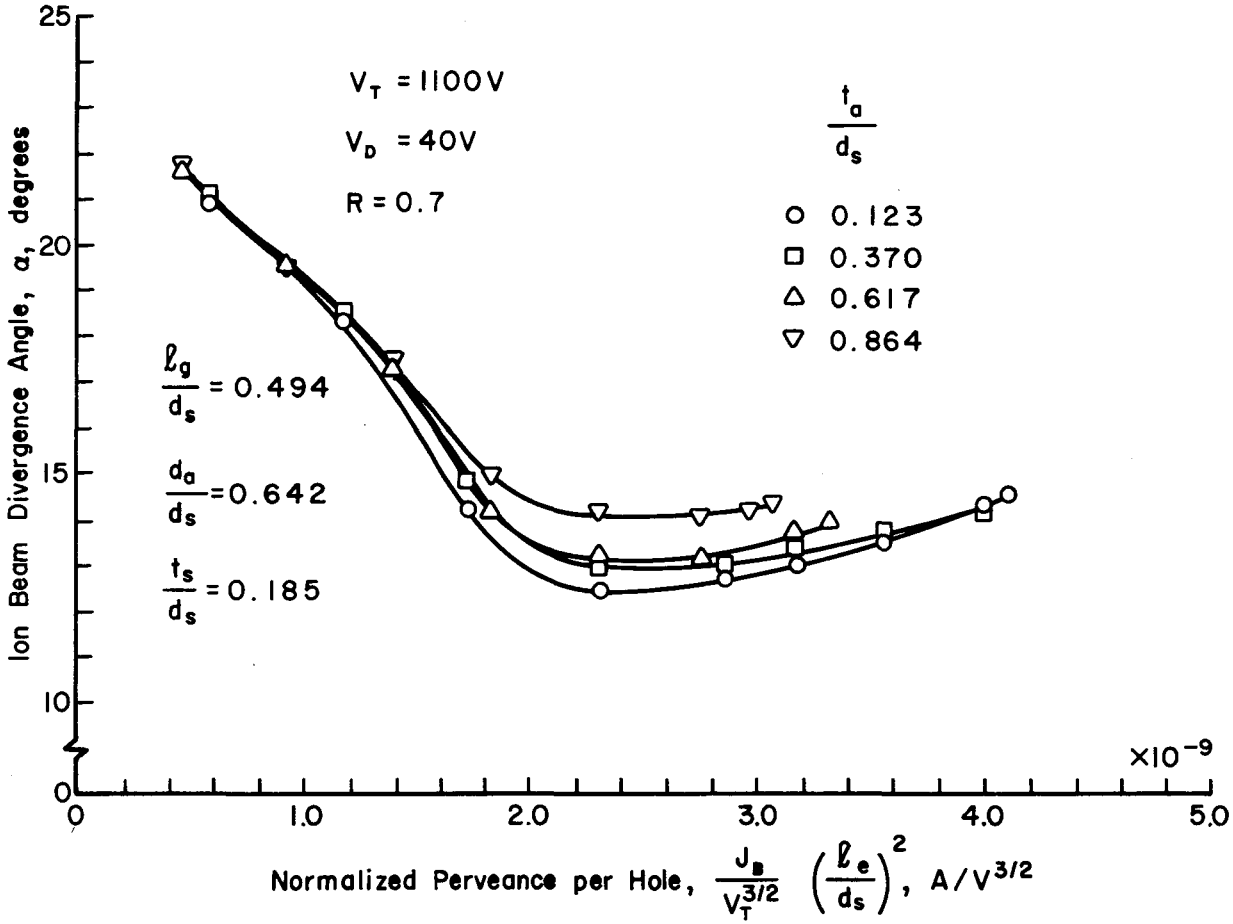

Fig. 2-6. Effect of accelerator grid thickness ratio on Ar ion beam divergence for a two-grid system (from Ref. 22).

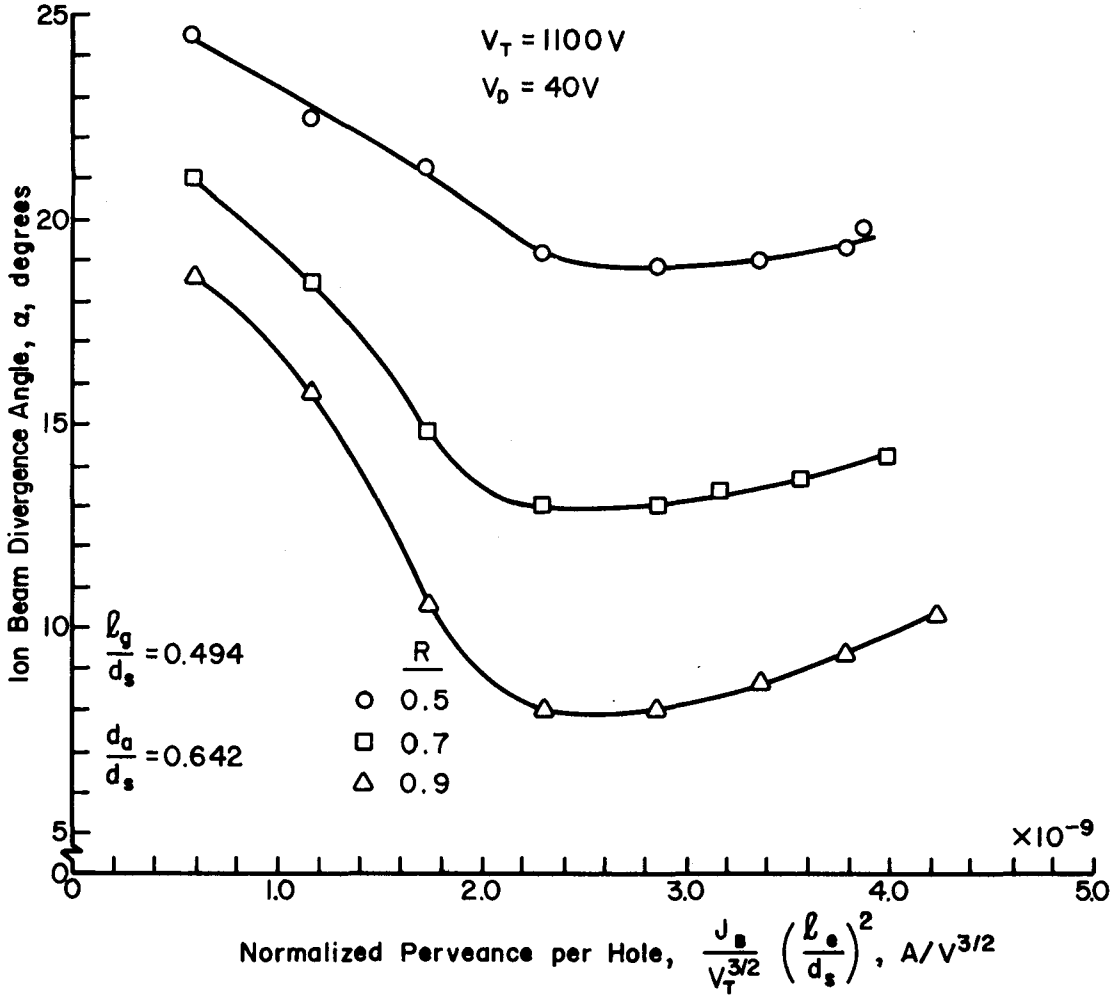

Fig. 2-7. Effect of the net-to-total voltage ratio (R) on Ar ion beam divergence for a two-grid system (from Ref. 22).

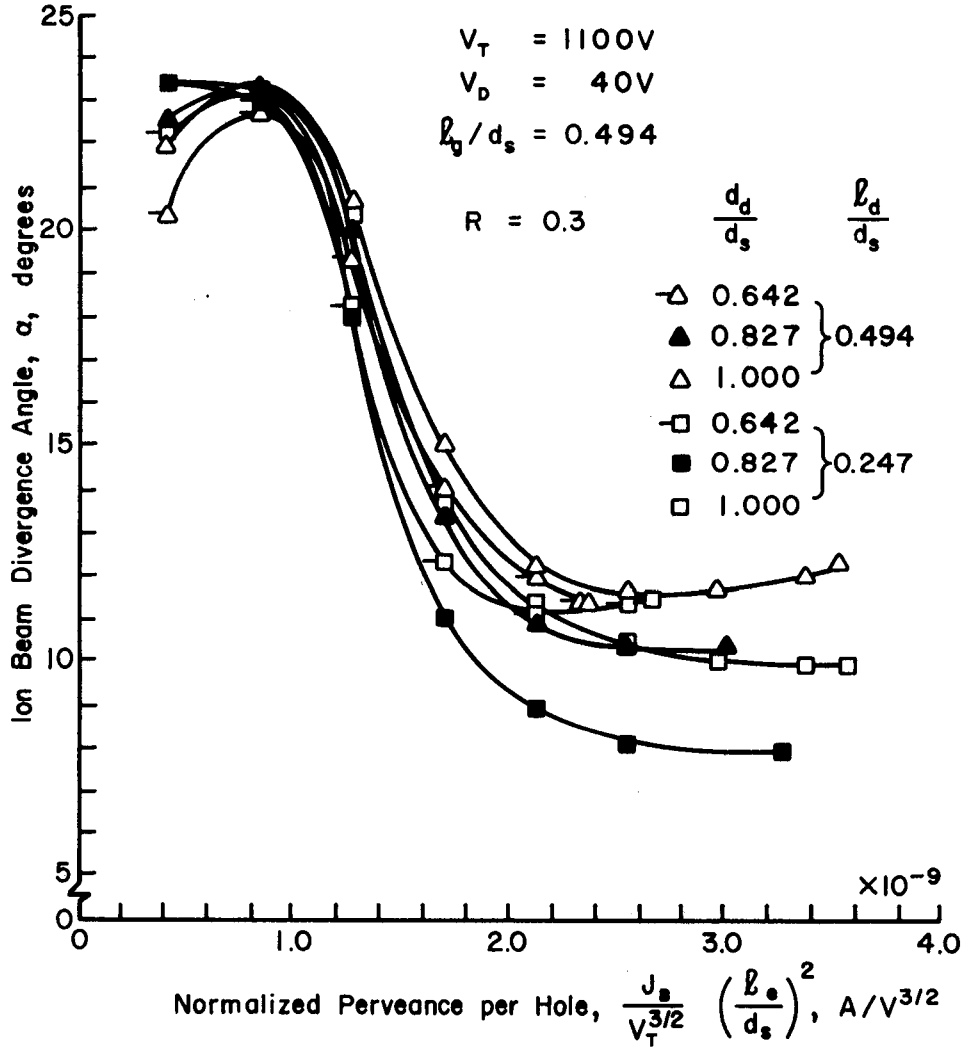

Fig. 2-8. Effect of decelerator grid hole diameter on Ar ion beam divergence for a three-grid system (from Ref. 22).

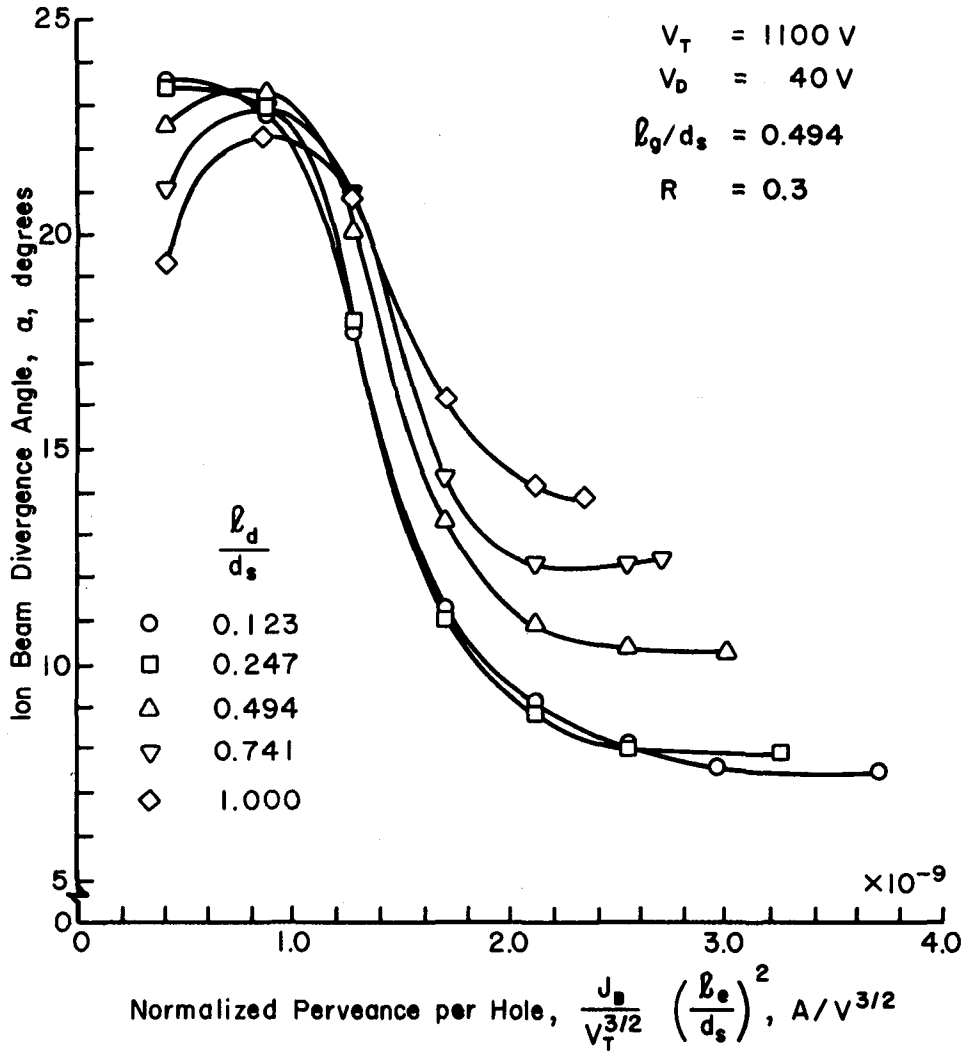

Fig. 2-9. Effect of decelerator gap ratio on Ar ion beam divergence for a three-grid system (from Ref. 23). R = 0.3

established dishing technique for molybdenum grids in a rectangular beam configuration.

It was felt that carbon was an adequate choice for the span-to-gap requirements of the rectangular beam. Pyrolytic graphite has a lower coefficient of expansion across the plane and a higher thermal conductivity across the thickness than does ordinary high density graphite, but pyrolytic graphite is considerably more expensive than ordinary graphite and does not appear necessary for this application. Pyrolytic graphite also tends to warp in larger sizes due to stresses generated in the deposition process. Therefore, high density conventional graphite was the grid material used.

Grids made from high density conventional graphite are substantially weaker than molybdenum and cannot offer the superior span-to-gap ratio that can be used with dished molybdenum. Graphite grids have been successfully operated at a span-to-gap ratio of about 100:1 for circular beams.[4] A grid for a rectangular beam, however, is supported essentially in only one direction. A span-to-gap ratio of 50:1 was therefore selected for the 5 cm direction. This span-to-gap ratio and the 5 cm width correspond to a 1 mm gap. This gap is felt to be sufficiently small to permit high ion current densities to be generated.

In general, many small apertures in the ion optics screen grid will result in more beam current extraction than will a few large apertures. This need for many apertures can be understood from Eq. (2-5). The screen hole diameter (d_s) may be as small as possible as long as the effective acceleration length (ℓ_e) is also decreased to keep their ratio the same. If the ratio (ℓ_e/d_s) remains unchanged the same current extraction is possible for smaller holes. From the viewpoint of

Poisson's equation, then, a maximum current density results from closely spaced grids with many small holes. However, experimentally a lower limit on the screen hole diameter is found at about 2 mm.[8] Although it is not understood why, smaller holes result in less current capacity. As shown in Fig. 2-3, 2.06 mm diameter holes show a maximum normalized perveance of about 4.0×10^{-9} $A/V^{3/2}$, compared to 0.97 mm diameter holes which gave a maximum normalized perveance of about 2.2×10^{-9} $A/V^{3/2}$. A screen hole diameter of 2 mm was therefore chosen as the minimum practical size for large-beam ion optics.

The number of apertures in the screen grid can also be increased by using a closer spacing between the apertures. The limiting condition for reducing the spacing is that the remaining material between screen apertures must be sufficient for mechanical strength. A screen open area fraction of 0.58 was selected to provide the minimum required strength. This open area fraction corresponds to a center-to-center spacing of 2.5 mm for 2 mm diameter screen holes, with the holes arranged in a hexagonal array.

Two and three-grid approaches have been considered for the rectangular beam ion optics design. In summary, a two-grid approach resulted in a design value ion current density of about 2 mA/cm^2 whereas the three-grid approach resulted in about 6 mA/cm^2 with a wider range of net-to-total voltage ratios possible. The three-grid approach was therefore selected for this design. A more detailed comparison of these two designs is given in the next two sections.

Two-grid approach. The screen hole diameter and center-to-center hole spacing were 2 mm and 2.5 mm respectively, as mentioned previously. The accelerator hole diameter should be large for high current

extraction but small to reduce neutral gas flow from the source. Also, it should be consistent with a moderate beam divergence, assumed to be 10 degrees or less in this analysis. Figure 2-4 shows the effect of various accelerator hole diameter ratios (d_a/d_s) on Ar ion beam divergence and on maximum normalized perveance per hole. As will be shown in connection with the discussion of the R effect a higher value of R can be used to reduce the divergence to 10 degrees. For the range of accelerator hole diameter ratios investigated, the change in ion beam divergence is not significant. However, the maximum obtainable normalized perveance does change considerably. The larger accelerator hole diameter ratio (0.827) gives the larger normalized perveance ($\sim 5.2 \times 10^{-9}$ A/V$^{3/2}$) and was chosen for this two-grid approach. Notice that this diameter ratio can be used for minimum ion beam divergence at a reduced normalized perveance. The value of 5.2×10^{-9} A/V$^{3/2}$ is also about 77% of the 6.79×10^{-9} A/V$^{3/2}$ value expected for $d_a \approx d_s$. These numbers are only of qualitative interest for the data shown, though, because none of the operation (Figs. 2-4, 2-4 and 2-6) is at or below the assumed maximum divergence of 10 degrees at a net-to-total voltage ratio (R) of 0.7.

Equation (2-5) shows that more current may be extracted as the grid separation is made smaller. The minimum grid spacing is determined by the maximum permissible electric field and/or maximum span-to-gap ratio. As discussed earlier a maximum span-to-gap ratio for the 5 cm dimension was taken to be 50:1. The corresponding gap between grids is therefore about 1 mm.

A conservative maximum electric field (obtained with H_g) is about 2000 V/mm.[12,13] Experience has shown that the maximum electric field

should be as high, or higher with Ar.[4] A conservative maximum total voltage should thus be about 2000 V for the selected 1 mm gap.

Changes in grid thickness over a moderate range were not found to significantly affect ion beam divergence, as shown in Figs. 2-5 and 2-6. Figure 2-5 shows effects on ion beam divergence due to changes in screen grid thickness while Fig. 2-6 shows effects due to changes in the accelerator grid thickness.

A reduced screen grid thickness, though, has been found to decrease the discharge power requirements.[12] An explanation of this phenomenon is offered in Ref. 8. The screen grid thickness was specified to be 0.5 mm as a compromise between the discharge power loss and mechanical strength. Accelerator grids with thickness ratios (t_a/d_s) of 0.617 and less show lower beam divergence angles and higher maximum normalized perveance values (Fig. 2-6). Therefore, a 1 mm thick accelerator grid ($t_a/d_s = 0.5$) was chosen.

For thruster applications the accelerator hole diameter and thickness are much more important because the neutral loss is a more critical parameter in electric space propulsion. For ground applications, the neutral loss is of interest but is usually not critical. Smaller holes and a thicker grid tend to decrease the neutral loss from the chamber. For those applications where the neutral loss is important, the accelerator configuration can be further optimized.[6,13]

For the two-grid approach, Fig. 2-7 shows that a high net-to-total voltage ratio (R) is required for a divergence angle less than 10 degrees using the 1 mm spacing selected in this design. Interpolation of data at R = 0.7 and R = 0.9 result in a minimum net-to-total voltage ratio of about 0.86 for a 10 degree divergence angle. The normalized perveance

at this point is about 2.24×10^{-9} $A/V^{3/2}$ for Ar working gas. If the net-to-total voltage ratio (R) is increased to 0.9 a maximum normalized perveance for the same 10 degree divergence is about 3.36×10^{-9} $A/V^{3/2}$. Using Eq. (2-5) and the other parameters mentioned earlier, net-to-total voltage ratios of 0.86 and 0.90 result in 1.1 and 1.6 mA/cm^2 ion beam current densities, respectively, for a maximum divergence angle of 10 degrees.

Thus two-grid operation with less than a 10 degree divergence angle is not practical for $R < 0.86$, while electron backstreaming can be expected for an R much greater than 0.9. It is true that changing the grid spacing would change the current density. But if operation is possible at the desired divergence, going to larger spacings usually results in little or no gain in current density. Something under 2 mA/cm^2 should therefore be expected with two-grid ion optics regardless of design details.

Three-grid approach. The screen hole diameter (d_s), Fig. 2-1, and center-to-center hole spacing were again assumed to be 2 mm and 2.5 mm for the same reasons that were discussed previously.

The effects of the accelerator and decelerator hole diameters are coupled. The major effect of a larger accelerator hole diameter in a two-grid system is to increase the maximum extracted beam current (Fig. 2-4). For a three-grid system, an increase in the accelerator hole diameter can also significantly increase ion beam divergence, particularly at low R values. The decelerator hole diameter can limit the maximum beam current if it is too small, or it can increase ion beam divergence if it is too large (Fig. 2-8). A satisfactory design compromise was found to be an accelerator hole diameter ratio (d_a/d_s) of

0.64 and a decelerator hole diameter ratio (d_a/d_s) of 0.83.[7] Divergence was also found to decrease as the accelerator-decelerator gap was decreased (Fig. 2-9). But the span-to-gap limitation discussed previously limited this gap to the same 1 mm value as the screen-accelerator gap.

The screen and accelerator grid thicknesses remained 0.5 mm and 1.0 mm for the same reasons as those given for the two-grid design. The decelerator grid thickness was also found to have little effect on the divergence characteristics of the three-grid system.[7] Therefore, a 1 mm thick decelerator grid was selected for this three-grid design.

Figure 2-10 shows the advantage in minimum ion beam divergence that a three-grid approach has over the two-grid approach. The three-grid system exhibits a minimum divergence angle less than 10 degrees for net-to-total voltage ratios (R) greater than about 0.3 ($\ell_g/d_s = \ell_d/d_s = 0.494$) whereas the two-grid system must be operated at net-to-total voltage ratios (R) ≥ 0.86 to attain a divergence angle of 10 degrees or less.

For a 10 degree ion beam divergence and a net-to-total voltage ratio of 0.32 (Fig. 2-10) a maximum normalized perveance of 2.6×10^{-9} $A/V^{3/2}$ is found from Fig. 2-8. Using Eq. (2-5), this corresponds to a beam current density of about 6 mA/cm^2 at 500 eV (Ar) for this three-grid design. This is more than a factor of 3 increase in current density over the two-grid system. The three-grid design may also be operated over a much larger range of net-to-total voltage ratios (R) as seen in Fig. 2-10. Practical considerations such as any nonuniformity of the ion beam profile or thermal distortion of large ion optics will tend to reduce the current capacity from the calculated values

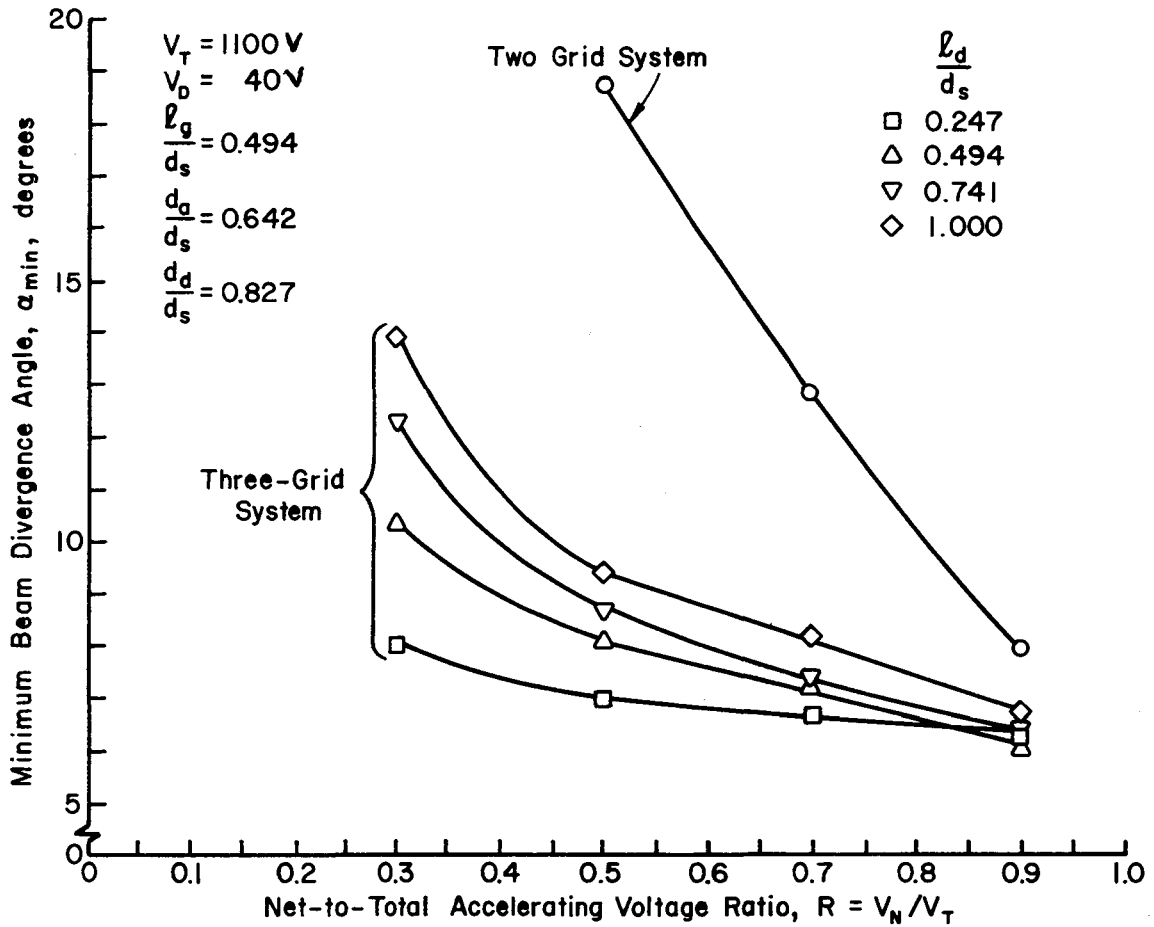

Fig. 2-10. Effect of net-to-total voltage ratio (R) on minimum Ar ion beam divergence of two and three-grid systems (from Ref. 23).

given herein. The relative advantage of the three-grid design over the two-grid design, however, should be about the same.

A three-grid design was therefore selected for rectangular ion beam extraction. Flat high density conventional graphite was selected for the grid material. For the final design, the screen grid was made 0.5 mm thick with 2 mm diameter holes on 2.5 mm centers in a hexagonal array. The accelerator grid was made 1 mm thick with 1.3 mm diameter holes. The decelerator grid was also made 1 mm thick with 1.6 mm diameter holes. A spacing of 1 mm was used between each pair of grids. The maximum total (screen-accelerator) voltage is about 2000 V with the 1 mm spacing. With a net voltage of 500 V, the minimum net-to-total voltage ratio (R) should be at least as small as 0.3. Smaller values of R could be used if larger divergence angles could be tolerated. For example, if the R value is 0.25 for a net voltage of 500 V and a total voltage of 2000 V a minimum half-angle divergence of 12 degrees is possible. The gain in current density would be about 30% for this lower R value at 500 eV.

In comparison with a two-grid system the third grid on a three-grid system, usually held at ground potential, should eliminate most substrate contamination due to sputtered grid material. Most sputtered grid material in a two-grid system results from high energy charge-exchange ions that impinge on the accelerator grid because this grid is held at a negative potential. With the grid facing the substrates at ground potential, most of this cause of contamination is eliminated.

Discharge Chamber Design

Discharge performance considerations. The discharge chamber selected for use with the ion optics described above was a multipole

configuration with permanent magnets. This type of chamber has the demonstrated ability to operate reliably for long periods of time over a wide range of operating conditions, while a high current density ion beam is being extracted.[14,15] In addition, the use of permanent magnets results in no magnet power supply being required. Although discharge losses are not a major concern for ground-based applications, the multipole ion source also provides comparatively low discharge losses.[15]

Discharge chamber dimensions. The dimensions selected for the discharge chamber were consistant with the 5 × 40 cm ion extraction area. The dimensions were also chosen to permit operation of the ion source in a vacuum facility of moderate size. Ion beam uniformity in the 5 cm beam dimension was not a significant concern because motion of the substrates in this direction would result in an integrated dose that is independent of the specific beam profile. If the pole pieces were too close to the edge of the beam, however, the current density might fall off excessively, resulting in a poorly defined ion beam edge. A 2.5 cm recess of pole pieces from the beam edges (Fig. 2-14) was felt to be adequate and perhaps somewhat over conservative in avoiding this large current density decrease. A 2.5 cm pole piece recess in the 5 cm beam direction dictated a 10 cm chamber width.

The long dimension of the discharge chamber was selected to be 45 cm with a 2.5 cm recess at both ends of the 40 cm beam length. It was not clear if this recess was large enough to give adequate beam uniformity in the 40 cm beam direction. Experimental results (see Section V), however, showed that the 2.5 cm recess gave a high degree of uniformity in the 40 cm direction.

The depth of an ion source is generally a compromise between discharge loss and the discharge chamber pressure required for operation. This pressure is, of course, a major factor in gas flow and pumping requirements. A shallow chamber tends to reduce discharge losses, but the required chamber pressure is reduced as the chamber is made deeper.

The primary electron region must be defined for the following analysis of ion chamber depth variation. The magnetic field strength in a multipole design decreases very rapidly (see Figs. 2-16 and 2-17) with increasing distance from the pole pieces. As a result of this decrease the magnetic field may be neglected in most of the discharge chamber volume. The primary electrons thus have access to most of the discharge chamber volume enclosed by the anodes and the ion optics. The primary electron region is therefore assumed to be defined by the ion optics and the dashed surface just inside the anodes and pole pieces indicated in Fig. 2-11.

A neutral loss theory developed by other workers[12,17,18] for the discharge chamber was used to determine the relationship between discharge chamber depth and internal chamber pressure. This neutral loss theory predicts a neutral loss rate assuming zero pressure external to the discharge chamber which can be expressed as the minimum neutral pressure required for stable chamber operation. This neutral loss theory is derived by equating the loss and production rates of ions within the chamber. The production rate is proportional to the neutral density so that the derivation gives the minimum neutral density required for that ion production rate. The assumption is made that all ionizations are caused by primary electrons emitted from the cathode. The ion production rate is thus given by

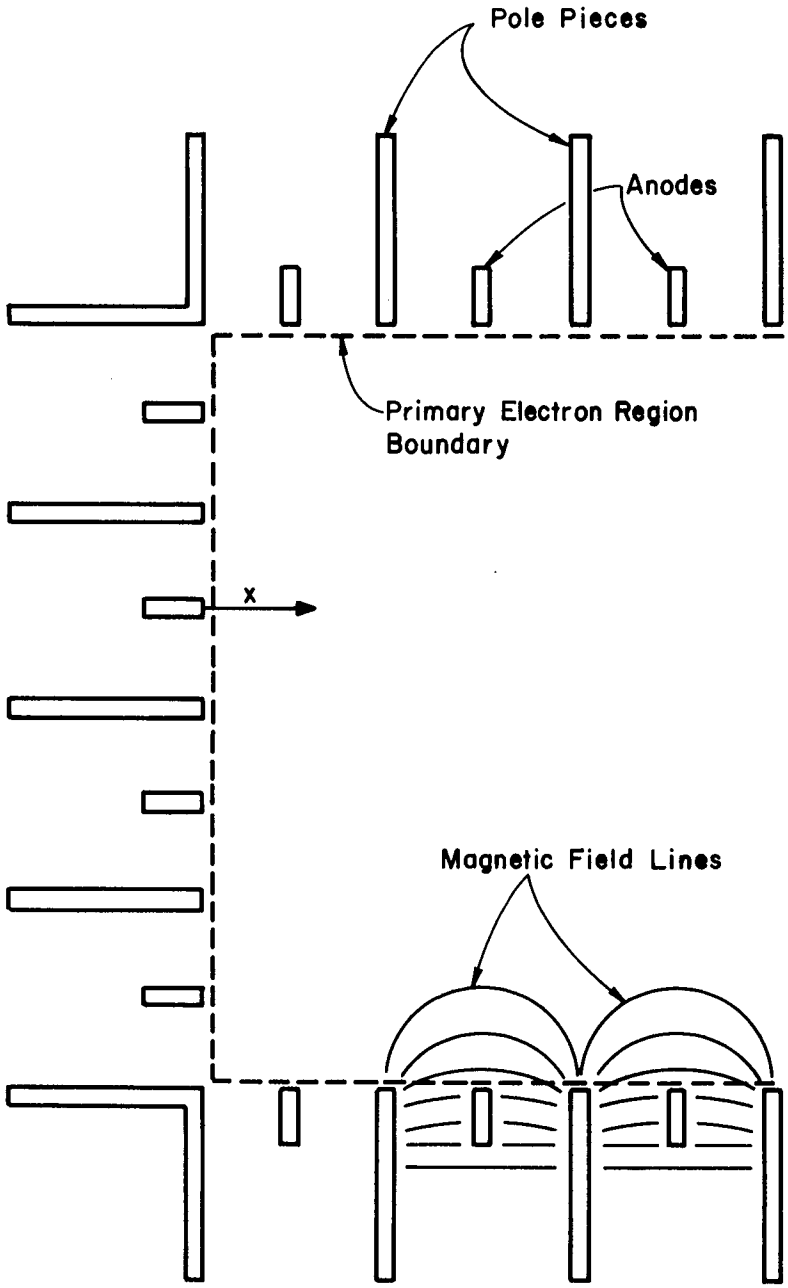

Fig. 2-11. Multipole discharge chamber. Dashed line shows assumed primary electron region outer surface.

$$\dot{N}_i = n_p v_p n_o \sigma \Omega_p \ , \tag{2-7}$$

where n_p and v_p are the number density and the velocity of the primary electrons, n_o is the neutral atom density in the ion chamber (Ar in this investigation), σ is the ionization cross section, and Ω_p is the primary electron region volume. The assumption that all ions are produced by only primary electrons was substantiated experimentally[18] as a limiting condition at high gas utilizations.

The ion loss rate is given by

$$\dot{N}_i = n_i v_i A_p \ , \tag{2-8}$$

where n_i is the ion number density, v_i is the directed ion velocity toward the walls and A_p is the primary electron region surface area (surface defined by ion optics and dashed line in Fig. 2-11). The directed ion velocity is that velocity which meets Bohm's criterion for a stable sheath,[19]

$$v_i(\text{at sheath}) \geq (kT_m/m_i)^{\frac{1}{2}} \ , \tag{2-9}$$

where k is Boltzmann's constant, m_i is the ionic mass and T_m is the Maxwellian electron temperature. In the neutral loss theory, the ion loss and production rates are equated to find the neutral density required for chamber operation at a maximum gas utilization condition,[17,18]

$$n_o = (m_e/2m_i)^{\frac{1}{2}}/\sigma(\Omega_p/A_p) \ . \tag{2-10}$$

As indicated above, the assumption of all ionizations resulting from primary electrons is consistent with operation near the high gas utilization limit. Therefore, the primary electron energy was substituted for the product of Maxwellian temperature and Boltzmann's constant in Eq. (2-9).

The Maxwellian electron population, however, does contribute substantially to the Bohm velocity. The modified Bohm criterion, derived by Masek,[20] for primary and Maxwellian electron contributions can be expressed as

$$v_i = v_p\left(\frac{m_e}{2m_i}\right)^{\frac{1}{2}}\left(\frac{T_m}{E_p}\right)^{\frac{1}{2}}\left(1 + \frac{n_p}{n_m}\right)^{\frac{1}{2}} \tag{2-11}$$

where n_m is the Maxwellian number density and E_p is the primary electron energy. Both T_m and E_p are expressed in units of electron volts. This modified Bohm criterion (Eq. (2-11)) may replace Eq. (2-9) in the neutral loss theory so that the following equation can be obtained in place of Eq. (2-10),[17]

$$n_o = \frac{(m_e/2m_i)^{\frac{1}{2}}}{\sigma(\Omega_p/A_p)}\left(\frac{T_m}{E_p}\right)^{\frac{1}{2}}\frac{(1 + n_p/n_m)^{3/2}}{n_p/n_m} . \tag{2-12}$$

It has been found[13] that smaller ion sources characteristically have higher Maxwellian electron temperatures ($\sim$10 eV for a 15 cm diameter[14]) than do larger ion sources ($\sim$4 eV for 30 cm diameter[4]). Because this rectangular ion source is about 10 cm in the short dimension a Maxwellian electron temperature of 10 eV was assumed. The primary electron energy has often been found to correspond closely to the discharge voltage. Primary electrons are emitted from the thermionic cathode and must fall through roughly the discharge potential in passing through the

cathode sheath. In the absence of probe data, the monoenergetic primary electrons are assumed to have an energy numerically equal to the discharge potential in volts. A 40 V discharge potential is used because lower voltages often result in an unstable discharge[13] and higher voltages usually result in significant fractions of doubly charged ions[14] which erode cathodes more rapidly and increase the damage depth for processing semiconductors. The primary to Maxwellian number density ratio (n_p/n_m) is less well known in the absence of probe data. Values range from about 0.03 for a 30 cm diameter cylindrical ion source[2] to about 0.1 for a 15 cm diameter source.[14] This ratio (n_p/n_m) may even be larger for smaller ion sources. Using the estimated values mentioned above and assuming that the internal chamber pressure is only due to the neutral gas contribution, the chamber pressure becomes (for Ar working gas)

$$p = \frac{2.82\times10^{-4}}{\Omega_p/A_p} \frac{(1 + n_p/n_m)^{3/2}}{n_p/n_m} \quad . \tag{2-13}$$

The chamber wall temperature (T_o) was assumed to be 550°K and the pressure is in Newtons/m^2. Using 45 and 10 cm for the length and width of the rectangular chamber a simplified equation for the required internal chamber pressure for a stable discharge results.

$$p(\text{Torr}) = [5.10\times10^{-5} + \frac{1}{D} (4.24\times10^{-4})] \frac{(1 + n_p/n_m)^{3/2}}{n_p/n_m} \tag{2-14}$$

The ion chamber depth (D) is expressed in cm.

A discharge loss parameter was found experimentally[13] which may be used to estimate a particular discharge loss associated with a certain ion chamber depth and may be expressed

$$\text{eV/ion} = 48.9\ (A_p/A_s)\ . \tag{2-15}$$

A_s is defined as the effective open area for ion extraction and the constant factor (48.9) was determined from previous multipole chamber data.[14] Using the 5 × 40 cm beam extraction area mentioned earlier (Ion Optics Design section) with an open area fraction of 0.58, the discharge loss may also be expressed in terms of the chamber depth as

$$\text{eV/ion} = 48.61\ D + 404.1\ . \tag{2-16}$$

Again D is in units of cm. The discharge loss versus chamber depth curve is shown in Fig. 2-12.

In order to determine a rough estimate or at least a range of ion chamber depths for this design, Eq. (2-14) and Eq. (2-16) may be equated for different chamber depths. The resulting equation is

$$\text{eV/ion} = \frac{2.06\times10^{-2}}{p\,\dfrac{n_p/n_m}{(1 + n_p/n_m)^{3/2}} - 5.10\times10^{-5}} + 404.1\ , \tag{2-17}$$

and may be used to determine a reasonable range of chamber depths. The pressure is expressed in Torr and is plotted with discharge loss for different values of n_p/n_m in Fig. 2-13. It should be kept in mind that

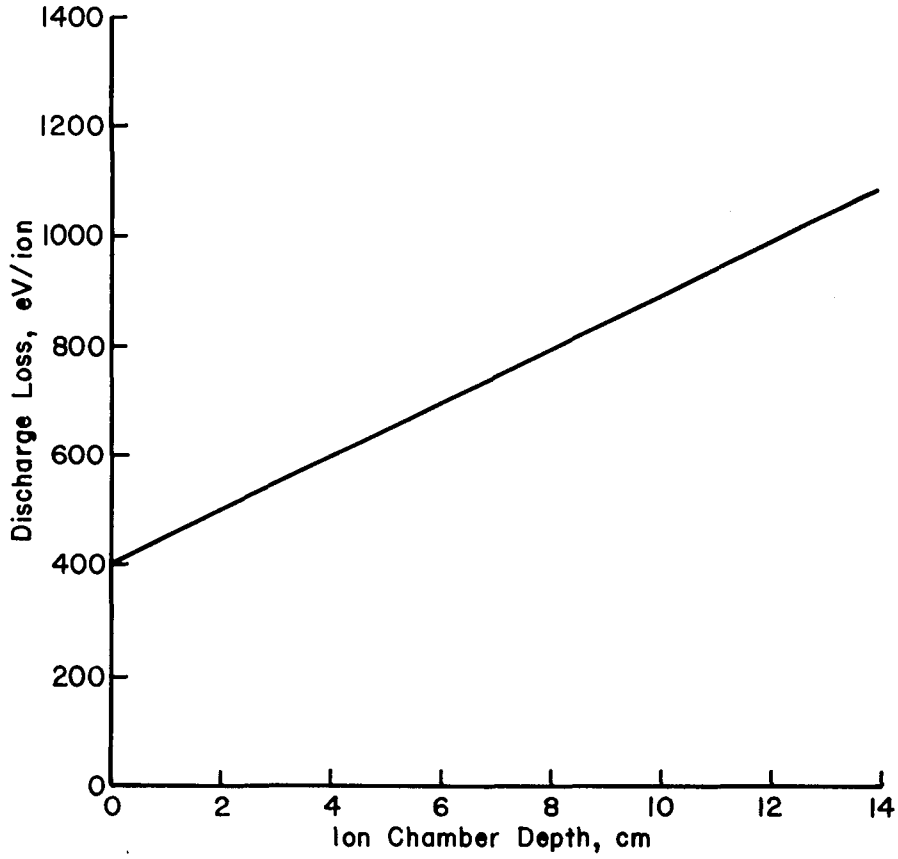

Fig. 2-12. Theoretical discharge loss versus ion chamber depth for a rectangular source.

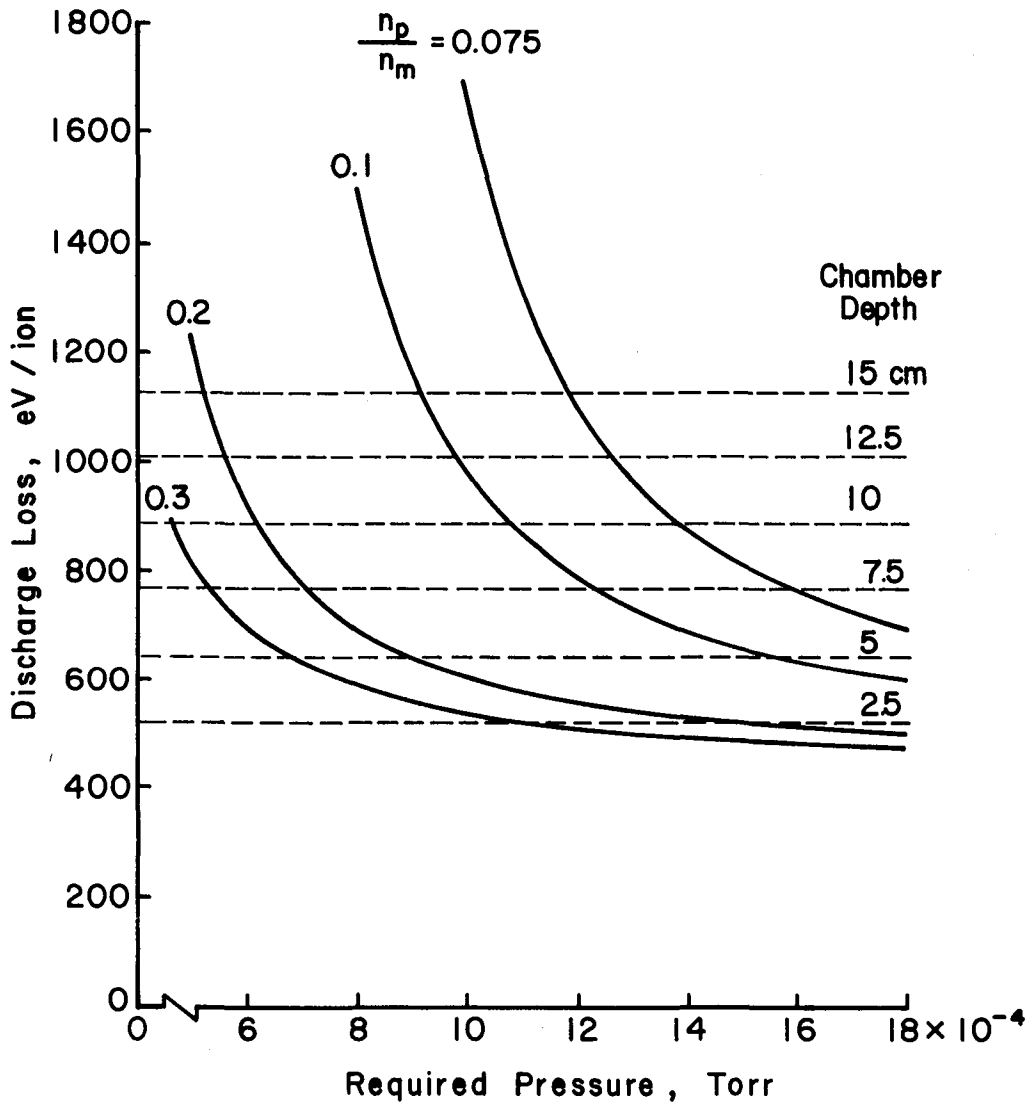

Fig. 2-13. Theoretical discharge loss versus required chamber pressure for a stable discharge at various values of n_p/n_m.

the curves in Fig. 2-13 assume that the minimum permissible pressure is used for each chamber depth.

The chamber depth selected represents a compromise between discharge loss and the permissible chamber pressure. The inverse relation for these two parameters is shown in Fig. 2-13 for several values of n_p/n_m. For each curve the discharge loss begins to increase rapidly as the chamber depth is made larger than about 10 cm. The discharge loss is not reduced much however, if the chamber depth is made smaller than about 5 cm. A large chamber depth is desired for a low chamber pressure, which, in turn, is desired for decreased sample and source contamination. Low discharge losses are desired for reduced power supply requirements and reduced facility heating problems. With no specific value required for pressure the range of 5 to 10 cm appeared of most interest for the chamber depth.

Multipole sources are essentially modular designs with a magnetic pole and an associated anode constituting one module. These modules were made 2.5 cm wide herein for ease of anode insulator feedthrough placement and sputter shielding. More importantly, though, the permanent magnets available were magnetized to about 1 Tesla if the magnet length-to-diameter ratio is no less than about 4. Because Alnico V magnets 0.64 mm in diameter were readily available and because at least a 1 Tesla field for each magnet was desired the gap chosen was 2.5 cm. Considering both the 2.5 cm modular pole piece size and the 5 to 10 cm depth range of interest, a chamber depth of two to four modules was decided upon.

The refractory cathode wire should be far enough into the ion chamber to prevent primary electrons from escaping directly to

the anodes. Since the fringe field is negligible several cm from the pole piece edge (Fig. 2-16 and 2-17) it was decided that cathode placement should be at least one module width (2.5 cm) from a pole piece. The cathode should also be several cm from the ion optics to both reduce local heating of the ion optics and to avoid a nonuniform ion production profile. For these reasons a minimum depth of 7.5 cm (3 modules) was selected although a 5 cm depth (2 modules) might have been acceptable.

In summary, the chamber depth (7.5 cm) was selected as a compromise between discharge loss and pressure and refractory cathode heating. The chamber width (10 cm) and length (45 cm) were selected to insure beam uniformity for the 5 × 40 cm beam area. A cross-section of this final design for the rectangular beam ion source is shown in Fig. 2-14.

Magnetic field configuration. The pole piece design selected used soft iron lengths 1.5 mm thick, 2.5 cm wide and spaced 2.5 cm apart (Fig. 2-14). The width and spacing are not felt to be important variables. However, as mentioned earlier the spacing should be at least 2.5 cm in order to utilize 1 Tesla permanent magnets (length to diameter ratio of at least 4) and to make room for available insulators and sputter shields for anode supports between pole pieces. Also, if the width and spacing were larger the outside dimensions of the ion source would be larger for the same working volume.

A very important parameter for the magnetic field design is the magnetic field integral needed to deflect primary electrons from the discharge plasma. Robinson derived an expression for this required field integral.[15]

$$\int_o^d B dx = 6.74 \times 10^{-6} E_p^{1/2} \qquad (2\text{-}18)$$

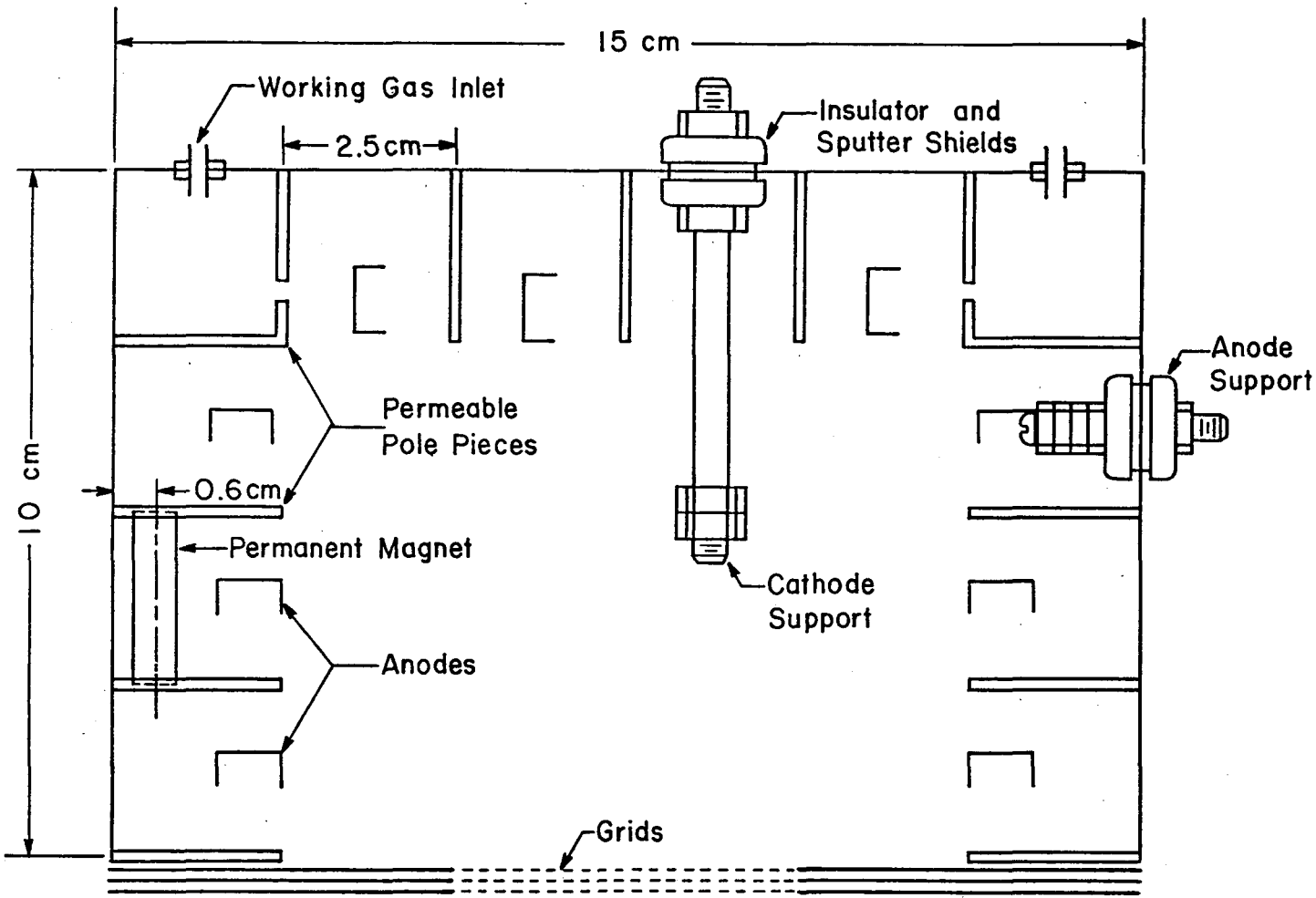

Fig. 2-14. Rectangular ion source cross-section.

E_p is the primary electron energy in electron volts and the left-hand side is in SI units (Tesla-m). The integral limits are from the inner chamber pole piece edges to some distance (d) into the discharge chamber where the magnetic intensity becomes negligible. This derivation (Eq. (2-18)) assumes a line of electron motion parallel to the dashed line in Fig. 2-11, i.e., an angle of incidence of 90 degrees for electron travel toward an anode from the discharge chamber. The assumptions that the magnetic induction ($\vec{B}$) is normal to the anode and the magnitude of $\vec{B}$ varies only with distance from the anode were used. The derivation of Eq. (2-18) also assumes that the radius of curvature of the anode (in a cylindrical ion source) is large compared to the depth of the fringe field which clearly makes this derivation (Eq. (2-18)) applicable to a linear type anode. Figure 2-15 is a plot of the magnetic field required to deflect primary electrons which have various incident energies.

Using an upper limit of 50 V for the discharge voltage, a required magnetic field integral of about 4.8×10^{-5} Tesla-m should be used for containment of primary electrons. However, a higher value was felt to be useful to reduce discharge losses. Robinson used an integral 50% higher than the calculated value for a 30 cm diameter ion source and obtained low discharge losses.[4] Therefore, a higher magnetic integral of 7.3×10^{-5} Tesla-m was tested in an attempt to lower discharge losses. Experimental magnetic measurements, together with trial-and-error arrangements of 6.4 mm diameter, 2.5 cm long Alnico V magnets, showed that five magnets per section (45 cm long) gave the flux necessary to generate a magnetic field integral of about 5.6×10^{-5} Tesla-m from the inside edge of a pole piece section. However, six magnets per section were used in the first version to increase the magnetic field

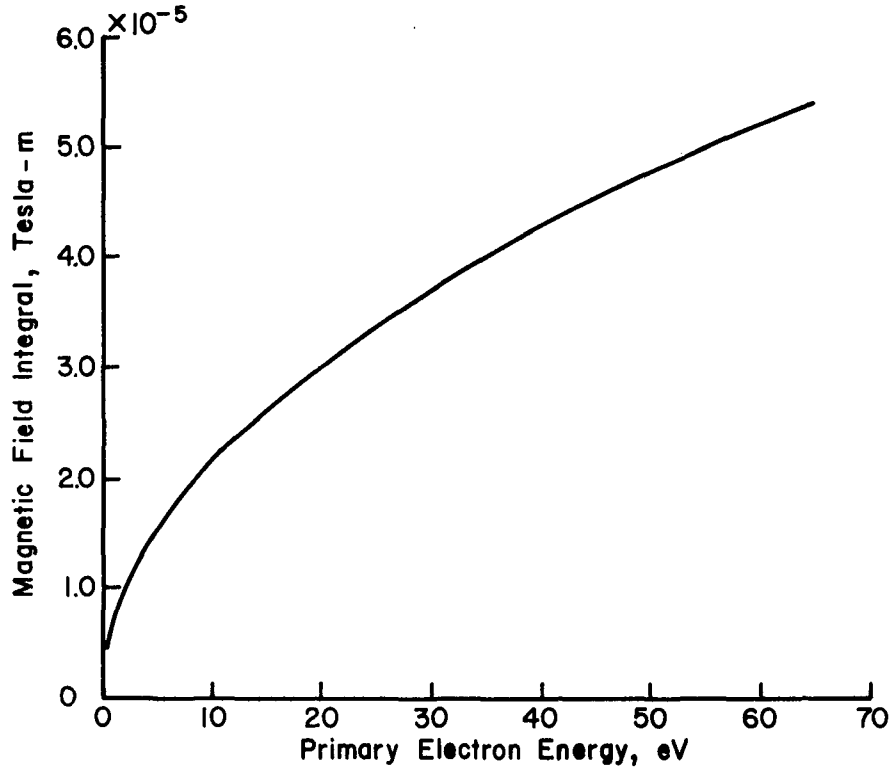

Fig. 2-15. Magnetic field integral needed in front of an anode to deflect primary electrons.

integral to the desired 7.3×10^{-5} Tesla-m. Because initial testing showed that the discharge plasma was not stable (discussed in Section IV), the final magnetic field integral selected was 5.6×10^{-5} Tesla-m which required only five magnets per section. Since the anode between a pole piece module could easily be adjusted in the direction normal to the magnetic field (x direction in Fig. 2-11), each anode was located to give an effective magnetic field integral of about 5.6×10^{-5} Tesla-m above that anode. A typical magnetic intensity variation with distance from the pole piece is shown for a corner section (Fig. 2-16) and for an end pole piece section next to the ion optics (Fig. 2-17). Most of the differences between Figs. 2-16 and 2-17 are associated with the difference of a corner location from other locations. This difference in magnetic field strength for corner pole pieces necessitates the recessed location of corner anodes in order to obtain the same magnetic field integral. Notice that in both cases (Figs. 2-16 and 2-17) the magnetic intensity decreases very rapidly and is negligible a few cm from the inner pole piece edge which is an important characteristic of the multipole design.

Cold rolled, low carbon steel, 1.5 mm thick, was selected as pole piece material because of its low reluctance and strength properties.

A magnetic field above about 1 Tesla can approach saturation in low carbon steel.[21] Since standard Alnico V permanent magnets are magnetized to about 1 Tesla there was no concern for saturation of the 1.5 mm thick pole piece as long as magnets on opposite pole piece sides were offset (Fig. 2-14).

The uniformity of the magnetic field between adjacent pole pieces was assumed because the reluctance of steel is much lower than for the

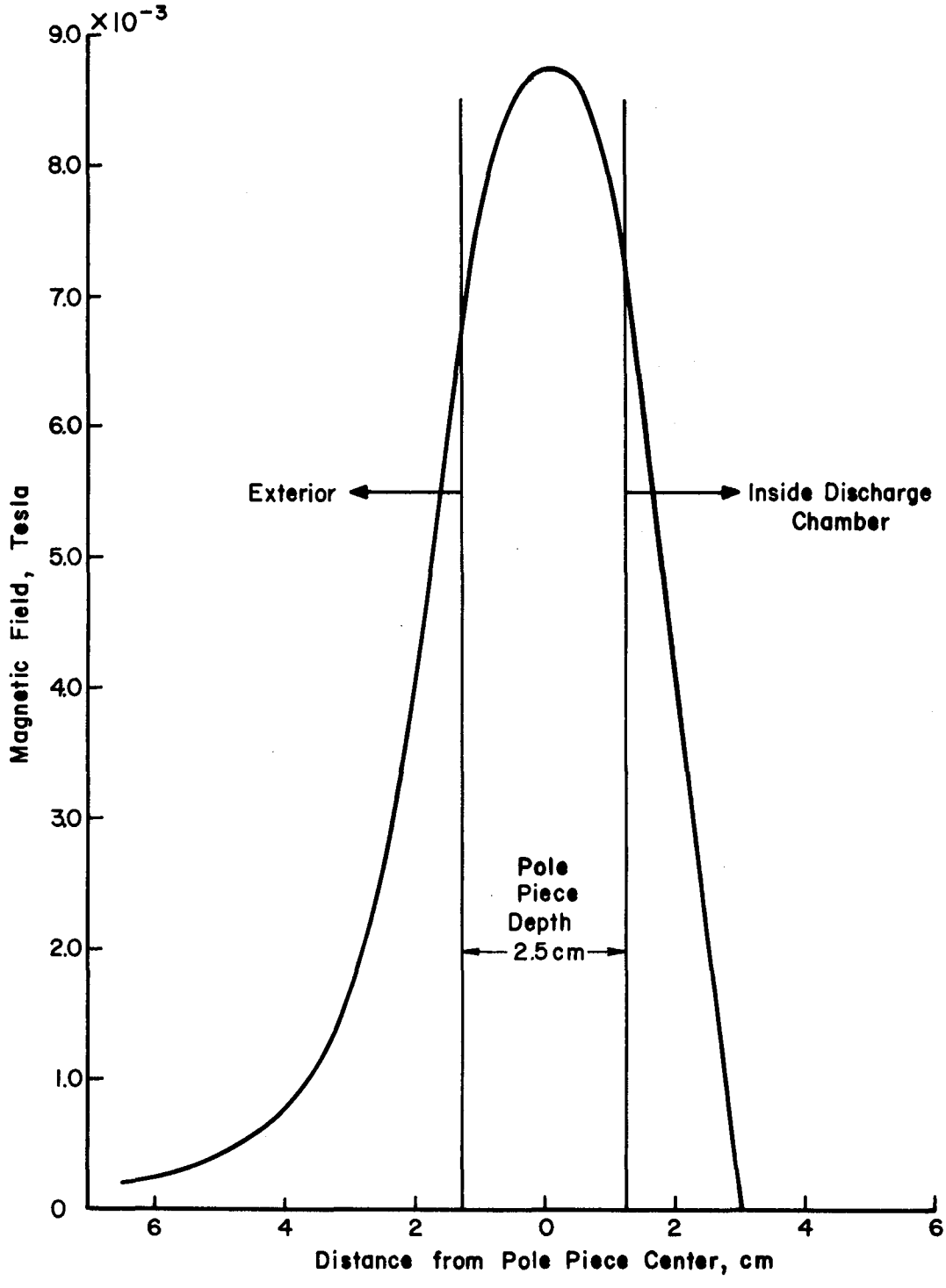

Fig. 2-16. Magnetic field strength for a corner pole piece section.

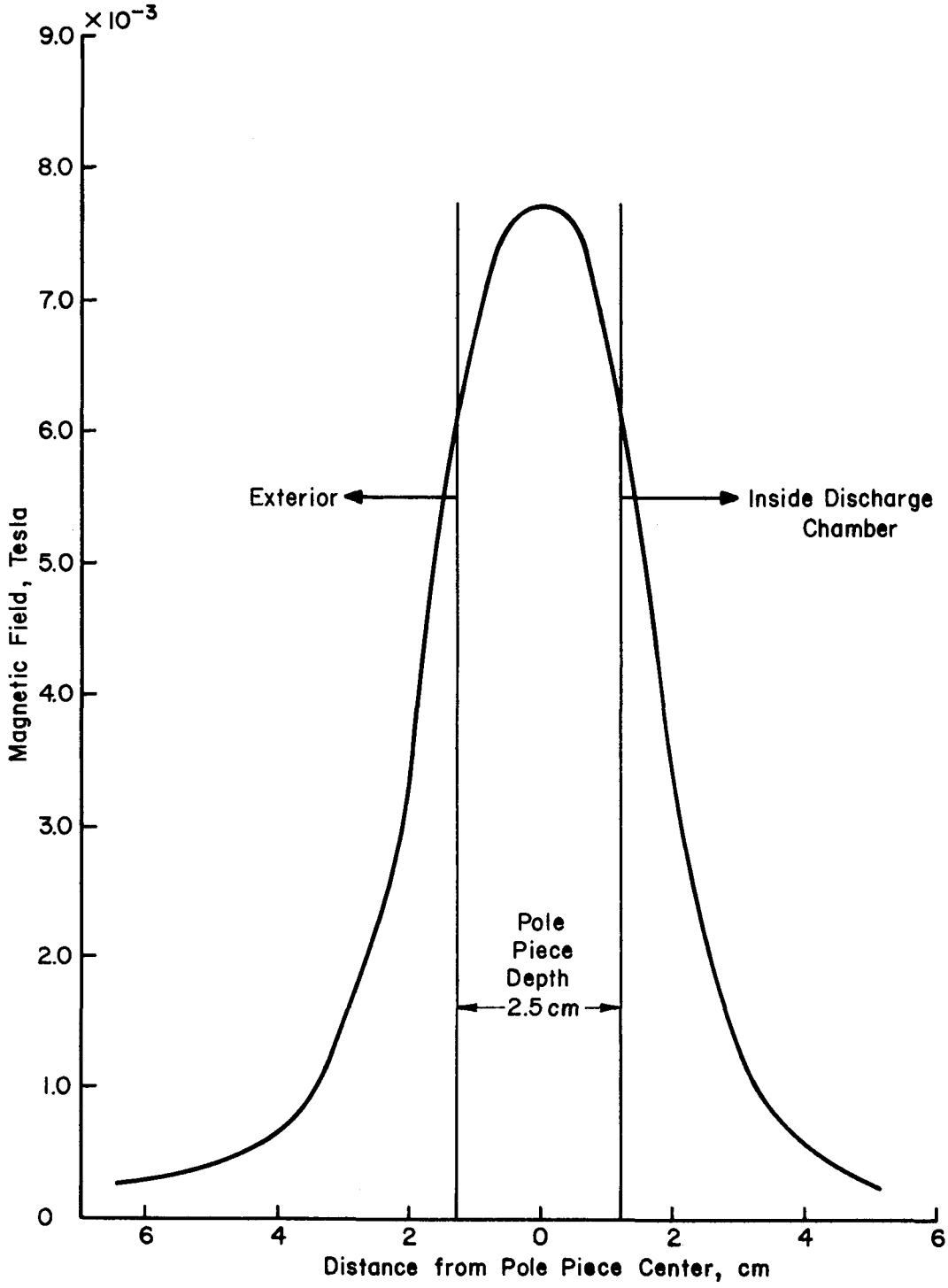

Fig. 2-17. Magnetic field strength for an end pole piece section (next to the ion optics).

2.5 cm air gap. Offsetting the permanent magnets also tended to minimize non-uniformity within the air gap. Robinson showed experimentally that the magnetic field variation between a single pair of adjacent pole pieces spaced 2.5 cm apart was uniform to within about 20%.[4]

Anode area limitation. A minimum effective anode collection area is required for stable ion source operation and for ease of initial discharge start-up.[13] The effective area for current collection is that area which makes the anode accessible to electrons from the discharge chamber which travel along magnetic field lines. The dashed line in Fig. 2-11 is assumed to represent the area of interest for a multipole ion source. Assuming a zero electric field by the anode the minimum anode area required for a stable discharge is approximately[13]

$$A_a = 13\, K_{ab} A_s e \int B dx / (k T_e m_i)^{\frac{1}{2}} , \qquad (2\text{-}19)$$

where K_{ab} is the anode-to-beam current ratio (I_B+I_D/I_B) and $\int Bdx$ has the value found previously (5.6×10^{-5} Tesla-m).

Using the ion beam current density (6 mA/cm^2) theoretically obtainable from the ion optics, a total beam current of 1.2 A is estimated which can be maintained by about a 24 A discharge current. A discharge loss of 800 eV/ion and a discharge potential of 40 V were used for the discharge current estimation. For Ar working gas, a Maxwellian electron temperature of 10 eV and a fringe-field integral of 5.6×10^{-5} Tesla-m, the required anode area given by density-gradient diffusion (Eq. (2-19)) is 0.089 m^2. The actual anode area for the rectangular ion source with dimensions of 45 × 10 × 7.5 cm is 0.101 m^2 (with one possible anode omitted to allow for cathode supports - see Fig. 2-14).

Discharge chamber performance. Using Eq. 2-16, a discharge loss of 800 eV/ion is estimated.[13,14] Reduction of either the depth (7.5 cm) or the width (10 cm) of the discharge chamber would decrease the discharge loss, but could also cause other problems, as indicated previously.

The neutral loss at the "knee" was estimated[13] to be about 340 mA-equiv. through a 1 mm thick accelerator grid with 1.3 mm diameter holes. The corresponding utilization would thus be the beam current divided by the sum of that beam current and 340 mA.

Cathodes. The total beam current for 6 mA/cm^2 is about 1.2 A, so that this value of neutralizer emission should be provided. Approximately a 10 cm length of 0.25 mm diameter tantalum should be adequate for this emission.[12] Two 5 cm lengths across the narrow beam dimension should thus be a reasonable neutralizer design.

For 800 eV/ion and a 50 V discharge, the discharge current should approach 24 A. It is clear that a refractory cathode should not have a total length much less than the discharge chamber length. Running a cathode the length of the discharge chamber would have the further advantage of promoting beam uniformity in that direction. For the level of emission required, a 40 cm total length should have a diameter (tungsten or tantalum) of 0.76-1.3 mm.[12] Although hollow cathodes would involve considerably more work (particularly to achieve beam uniformity in the long dimension) they would have some obvious power advantages over such a large refractory cathode. A refractory cathode, though, was used for the initial investigation reported herein.

III. FABRICATION

Grids

A drilling template for multiaperture electrodes was designed and fabricated to give the capability of making grids with different hole sizes and 2.5 mm center-to-center hole spacing. The template was made of hardened steel with 7199 locator holes 0.18 cm in diameter. A small locator pin in the drill-press bed, together with the locator holes, gave the proper hole spacing for the grids. With the grid holes located from beneath, 2.0, 1.6, and 1.3 mm drills could all be used with the same template. Tungsten-carbide drills and end mills were used for carbon drilling to minimize the dulling that often occurs with inert impurities in commercial carbon.

Six alignment holes were drilled through all three grids. Mica spacers were used between the grids to give the desired separation. (The use of mica is adequate for an experimental installation, but a production device should use more permanent aluminum-oxide insulators.) Two holes were drilled on the end of the screen grid so the three-grid system could be mounted directly to the ion source.

Discharge Chamber

The discharge chamber pole pieces were made of rectangular pieces of low carbon cold-rolled steel. All nine side pole pieces were 45 cm × 2.5 cm × 1.6 mm thick. The two corner pole pieces were made 45 cm × 5 cm × 1.6 mm thick and bent in the long dimension by 90 degrees. Holes for permanent magnet installation were milled 0.8 mm into the pole pieces, 6.4 mm from the outside edge. Magnet holes in opposite sides of the pole pieces were offset to avoid pole piece saturation. Five evenly

spaced 1.6 cm diameter holes were drilled in both corner pole pieces for working gas inlets into the discharge chamber. Figures 2-14 and 3-1 show most of these fabrication details.

Magnets were Alnico V, magnetized after cutting to length. Magnet dimensions were 6.4 mm diameter and 2.5 cm long. The magnets were placed between the pole pieces in such a manner that magnetic polarities of adjacent pole pieces were opposite. The three groups of pole pieces and magnets (back and two sides) were held together with two stainless steel threaded rods and nuts placed through each group. A box made from 1.6 mm thick stainless steel was fabricated to fit around the outside edge of the pole pieces for neutral gas and plasma containment.

The anodes, 42 cm long, were made from 0.5 mm thick stainless steel sheet, which was bent into channel form for rigidity and ease of attachment to supports. Each of the nine anodes was held in the center of the two adjacent pole pieces by two anode supports equally spaced from the anode ends. Each support consisted of ceramic insulators, sputter shields and a bolt with spacer nuts which facilitated anode position inside the discharge chamber. This configuration is depicted in Fig. 2-14. Three supports with insulators and sputter shields were mounted on the back plate for the 40 cm long cathode heater wire.

Two small bolts were spot welded into the downstream pole pieces to hold the grids in place when the chamber was set on its end. This means of screen grid attachment gave both direct electrical connection of the screen grid to the ion source and a tight mechanical fit to minimize neutral gas loss.

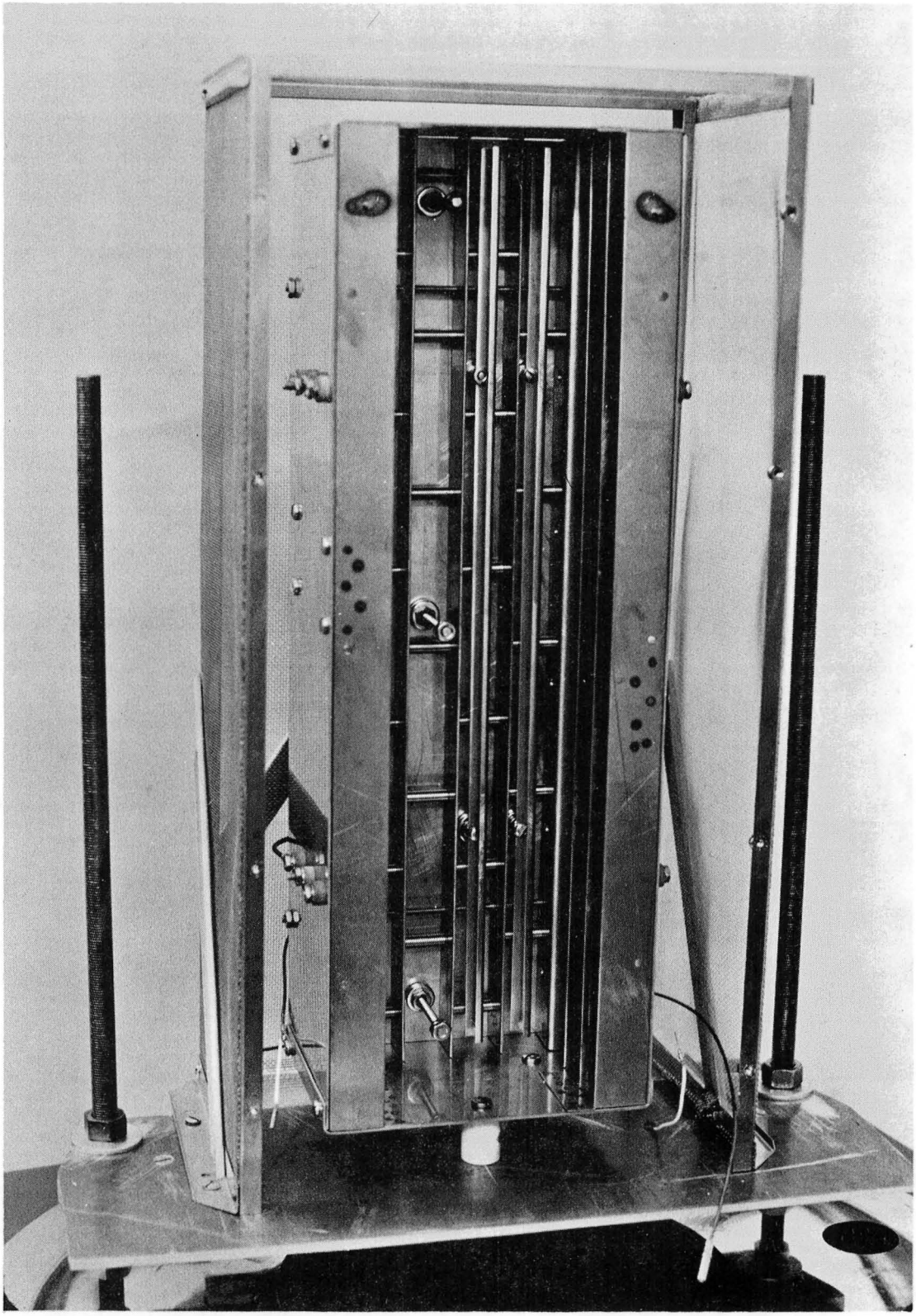

Fig. 3-1. Photograph of completed rectangular ion source without ion optics.

Final Assembly

Three ceramic insulators were used to support the ion source and grids vertically. A ground screen of 1.4 mm stainless-steel screen, square mesh, was built around the source and grids to keep the charge-exchange plasma electrons from the ion source positive potential. A sheet of formed stainless steel was placed around the decelerator grid for ease of source disassembly. The completed ion source, with ion optics and ground screen assembly is shown in Fig. 3-2.

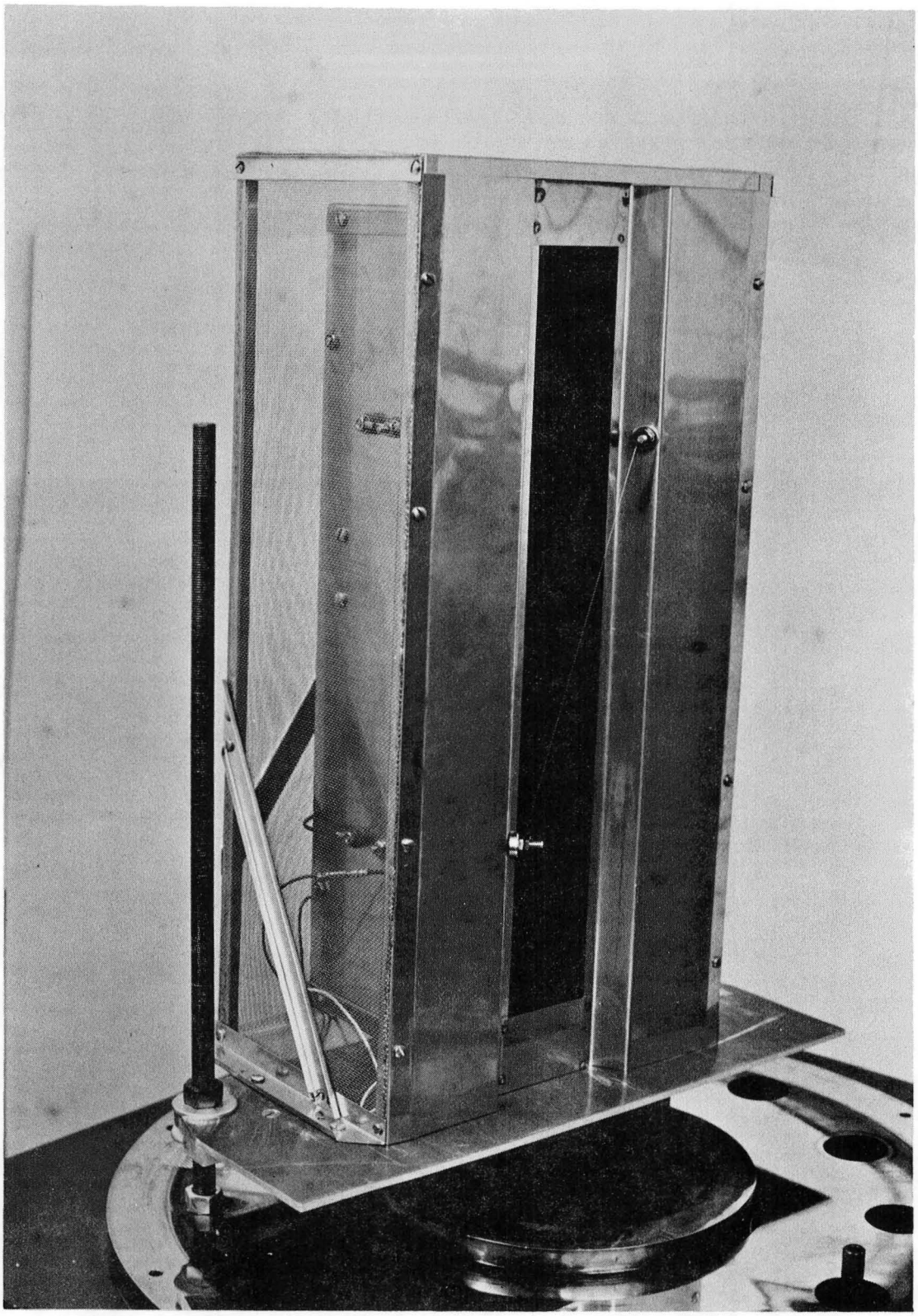

Fig. 3-2. Photograph of completed rectangular ion source with ion optics and ground screen.

IV. RECTANGULAR ION SOURCE PERFORMANCE

The rectangular ion source was operated with two different effective magnetic field integrals, 7.3 and 5.6 × 10^{-5} Tesla-m as discussed in Section II. These integrals were calculated from the pole piece inner edges to the discharge chamber center. Three graphite grids spaced 1.0 mm apart with 1.0 mm thick accelerator and decelerator grids were fixtured to the ion source. The screen grid used was originally 1 mm thick, then milled to about 0.5 mm thick. The screen and accelerator potentials were varied from 250 to 1000 and -120 to -1000 V, respectively. The decelerator grid was held at ground potential unless decelerator grid impingement was measured. Then the decelerator grid potential was held at -12 V for low energy (∿5 eV) neutralizer electron reflection. Ar working gas flow rates ranged from 360 to 1200 mA-equiv. for discharge loss calculations which resulted in background pressures of 2 to 9 × 10^{-4} Torr. The magnitude of resulting beam currents was usually limited by both high background pressure in the bell-jar facility used which caused arcing between the grids and by power supply limitations. The ion beam was probed with a Faraday probe assembly consisting of 20 Ta elements shielded with a screen mesh for electron reflection.

Large Magnetic Integral

For these tests the grid potentials were 500, -250 and 0 V for the screen, accelerator and decelerator. The magnetic integral of 7.3 × 10^{-5} Tesla-m appeared to be sufficient when a 1.0 mm thick screen grid was used. Discharge losses were reduced considerably when the screen was reduced to 0.5 mm as shown in Fig. 4-1. However, at the same time, severe problems developed in maintaining the discharge while high voltage was applied to the ion optics. These problems were most

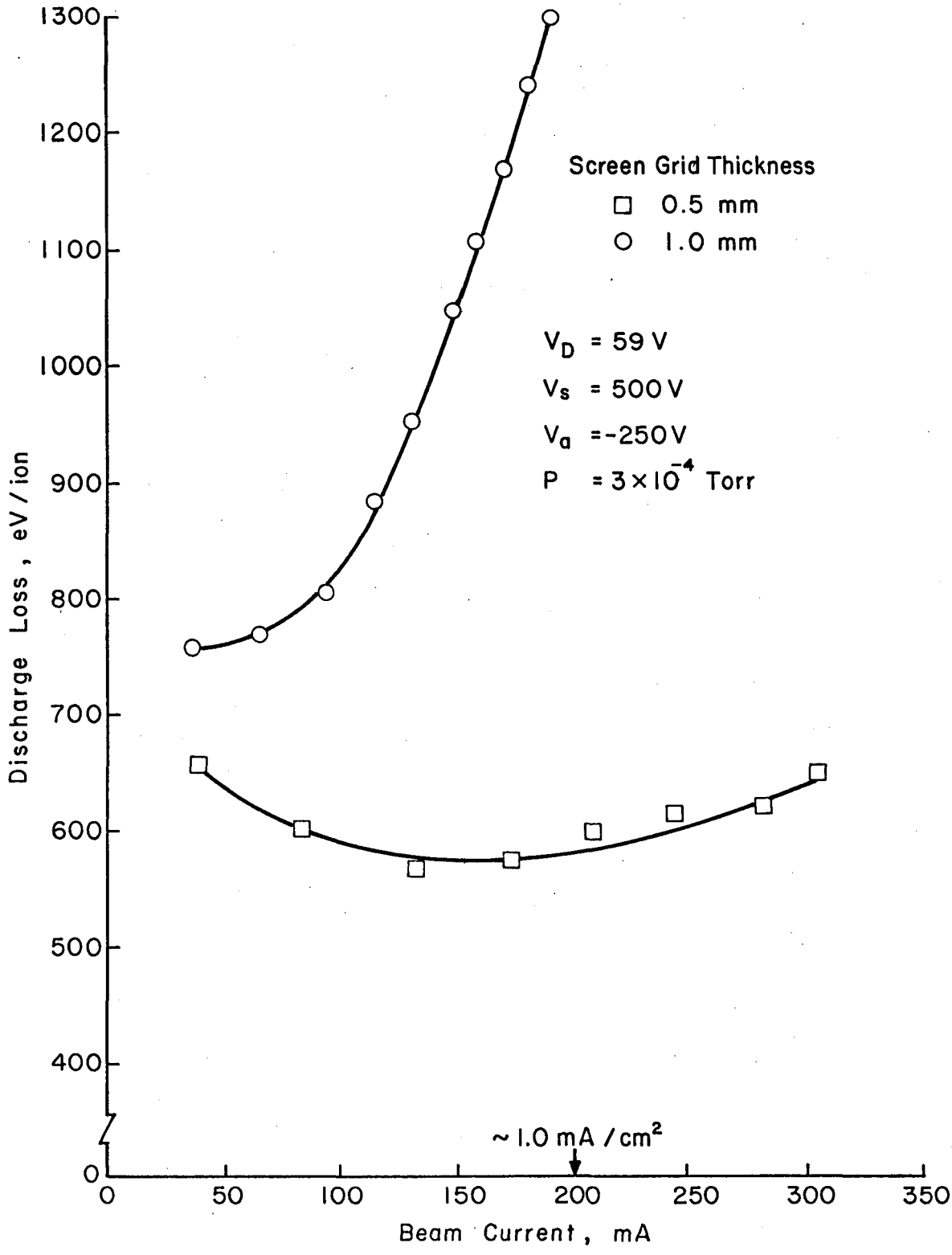

Fig. 4-1. Discharge loss for two screen grid thicknesses at the larger value of magnetic field integral.

noticeable at lower pressures, i.e., 2-5 × 10^{-4} Torr bell jar pressure. The ion source would not run stably at pressures below 2 × 10^{-4} Torr. Another feature of these problems was that the discharge would become stable if the accelerator grid was in a high impingement regime.

At 3 × 10^{-4} Torr the ion source operated at a discharge current, I_D, of 2 A and less, and a discharge voltage, V_D, of 59 V. But when sufficiently warmed (about 1/2 hour of operation before testing), higher I_D resulted in an oscillation mode in which the I_D was on about 16 sec., off about 10 sec. and then on again. As the I_D was increased, the oscillation period became shorter. However, when the accelerator grid was in the high impingement region, greater than 50 mA, the oscillation would cease and the discharge would stabilize. Stabilization also occurred when the high voltage was turned off. When data could be taken, the discharge losses with a 0.5 mm screen grid were calculated for 2 and 3 × 10^{-4} Torr as seen in Figs. 4-2 and 4-3. At higher pressures, 5-10 × 10^{-4} Torr, and higher, I_D became more stable, but frequent arcs occurred between the grids. Grid spacings were increased (1.5 mm) and decreased (0.56 mm) but oscillation was still evident.

Small Magnetic Integral

The magnetic field integral was then effectively decreased to 5.6 × 10^{-5} Tesla-m by extending the linear anodes into the discharge chamber another 2.5 mm from their original positions. After initial outgassing, the source operated stably from pressures of 6 × 10^{-5} to 1 × 10^{-3} Torr. The discharge was stable up to discharge currents developed by maximum cathode power available from the heater power supply. Pressures tested extensively were 1 × 10^{-4} Torr and higher. Figures 4-2 and 4-3 also show the discharge loss at two different pressures,

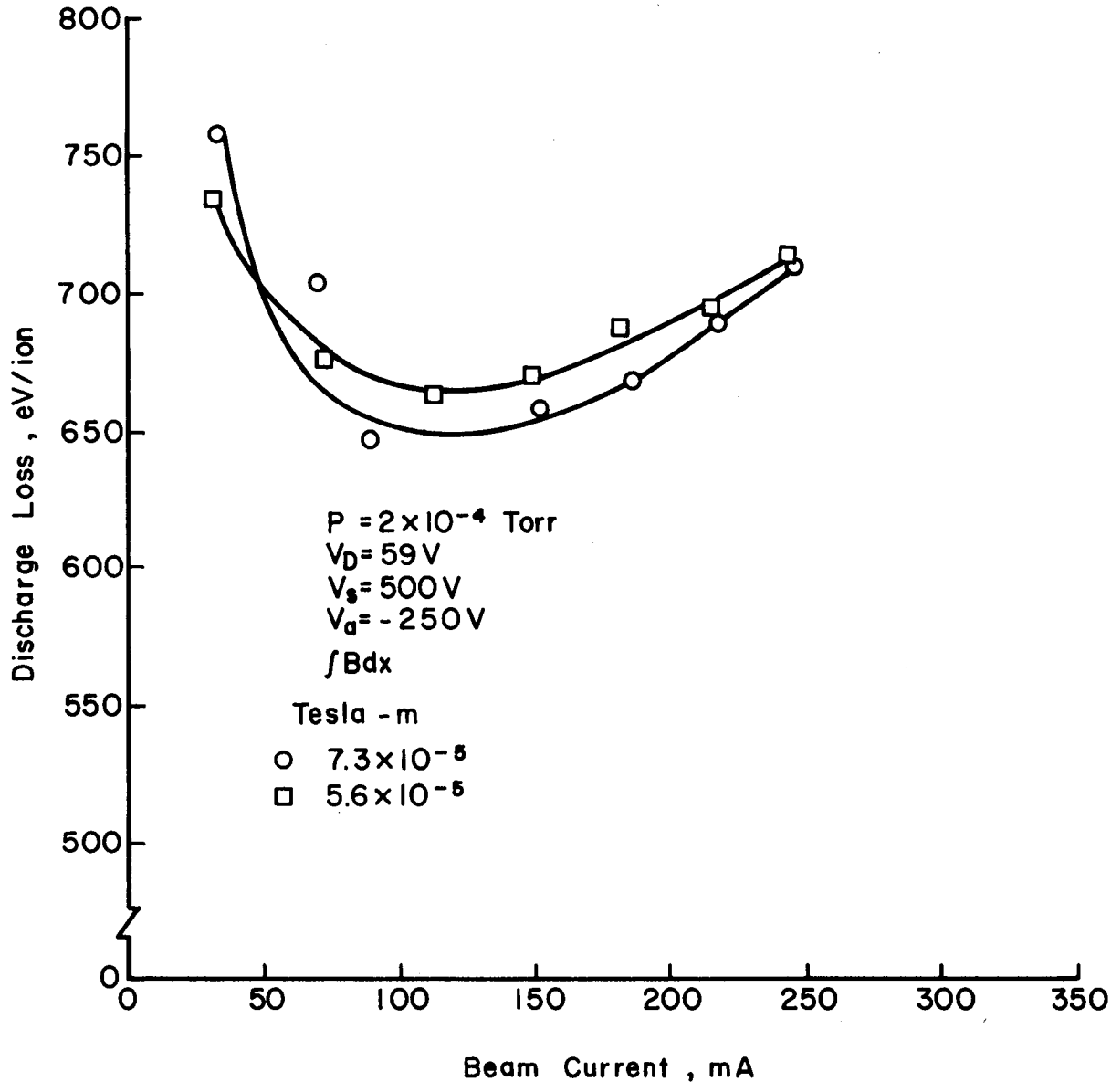

Fig. 4-2. Discharge loss for the two different magnetic field integrals at 2×10^{-4} Torr.

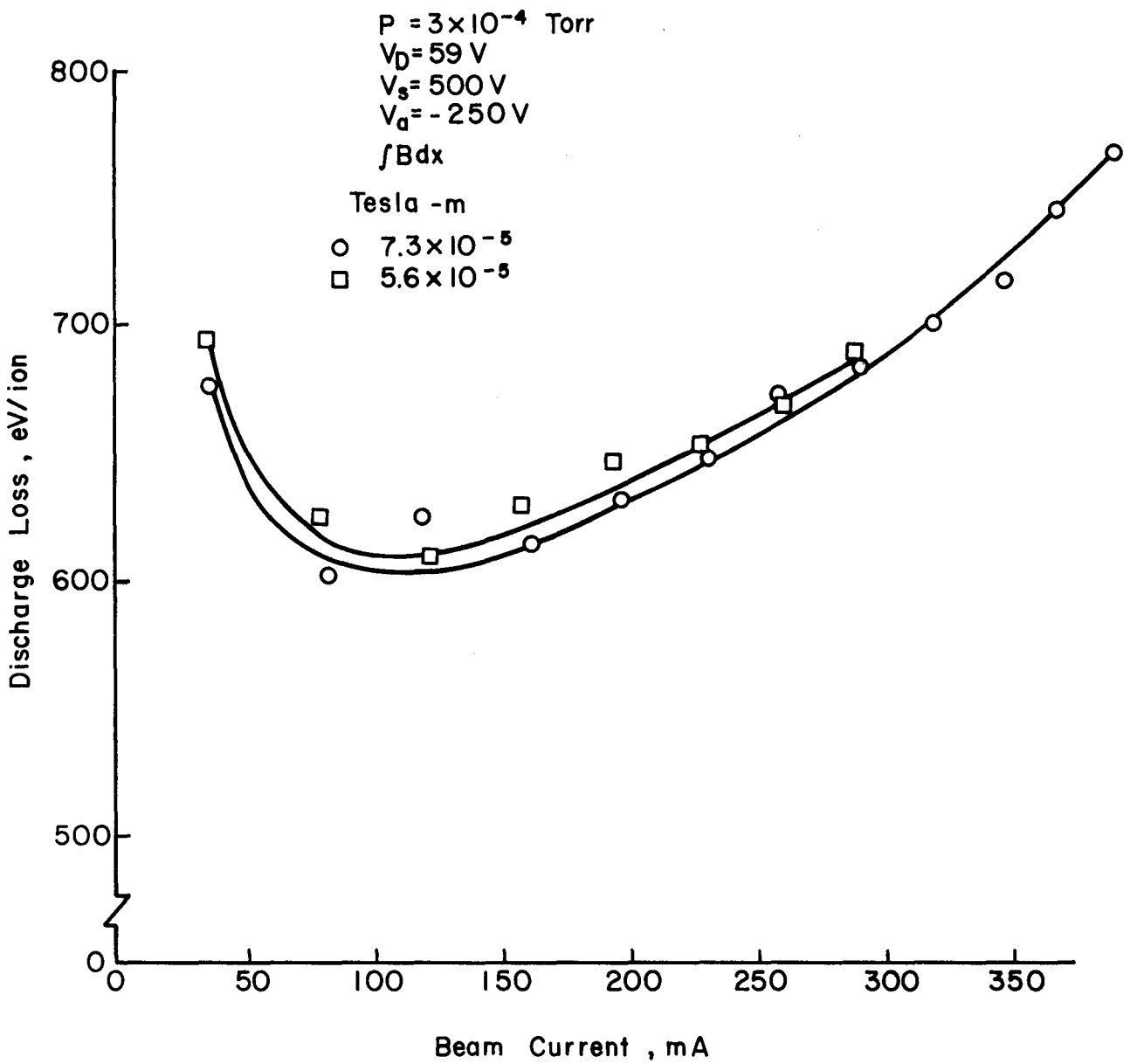

Fig. 4-3. Discharge loss for the two different magnetic field integrals at 3×10^{-4} Torr.

2 and 3×10^{-4} Torr, for the magnetic integral of 5.6×10^{-5} Tesla-m with a 0.5 mm thick screen grid. Although the small magnetic integral gives a higher loss, the curves for the two magnetic integrals are very close to each other. As mentioned earlier, the stability of the plasma inside the chamber was a serious concern for an integral of 7.3×10^{-5} Tesla-m.

Figure 4-4 shows a series of performance curves taken with a magnetic integral of 5.6×10^{-5} Tesla-m and a screen grid thickness of 0.5 mm. Ar flow rates varied from 360 mA-equiv. for 2×10^{-4} Torr to about 1200 mA-equiv. for 9×10^{-4} Torr. All data shown in Fig. 4-4 corresponded to stable operation.

Discharge-Loss Calculations

The ion source was connected to the supporting power supplies in two different manners in order to establish the correct discharge voltage for discharge loss calculations. The alternative connections were possible because a DC cathode heater was used. The two configurations studied are shown in Fig. 4-5 with a connection from the (-)DC Arc supply to the (-)DC Cath supply for configuration A and a connection from the (-)DC Arc supply to the (+)DC Cath supply for configuration B. This procedure changes the DC Arc reference of the (-)DC Cath in A to the (+)DC Cath in B. Configuration A has an effective discharge voltage less than 50 V if the DC Arc supply is set at 50 V, and B has an effective discharge voltage greater than 50 V for the same condition. Data were taken at both configurations with the following corrections:

$$\text{Configuration A:} \quad V_{panel} = V_D + (V_C/2)$$

$$\text{Configuration B:} \quad V_{panel} = V_D - (V_C/2)$$

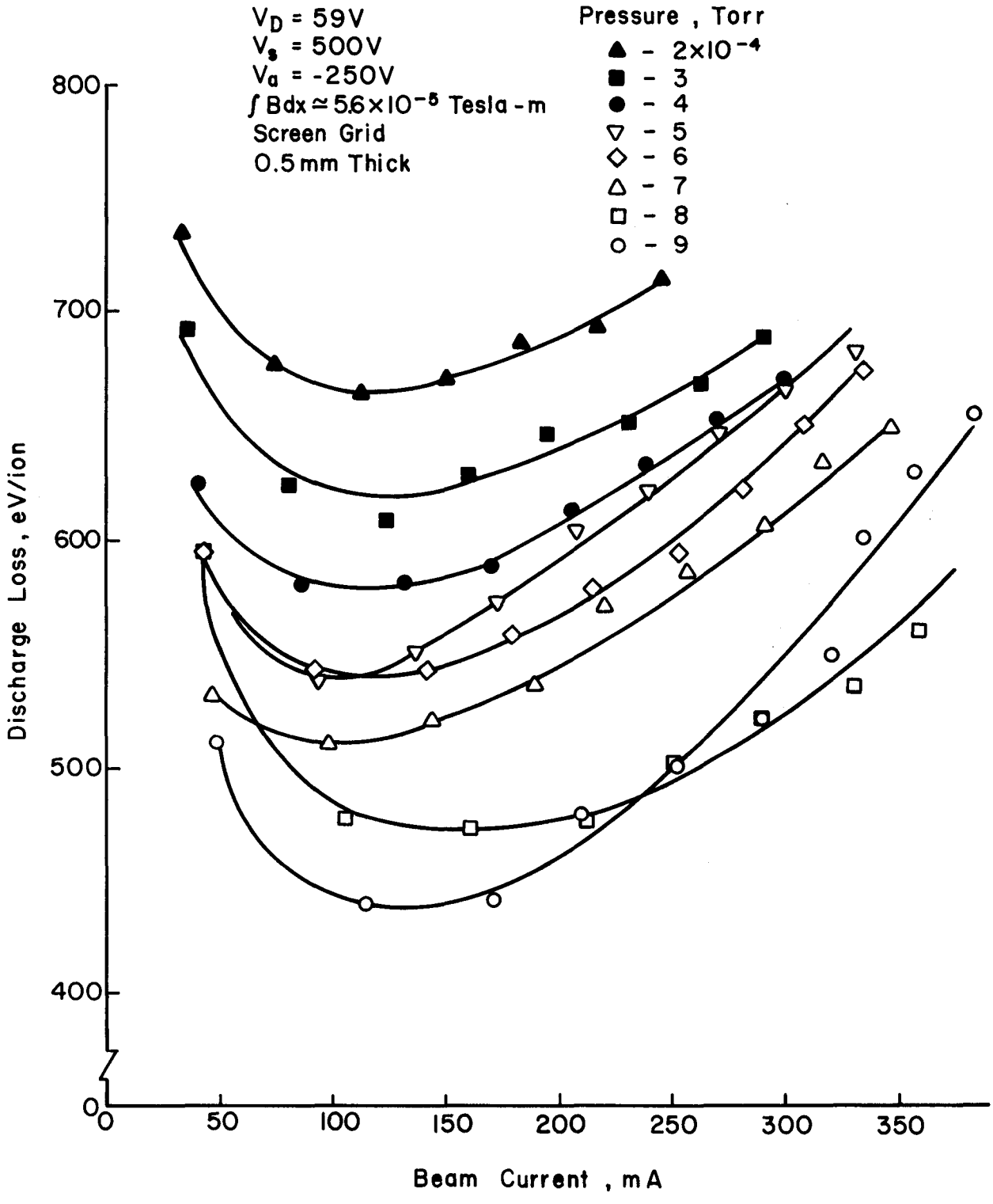

Fig. 4-4. Discharge loss for various pressures at the smaller magnetic field integral.

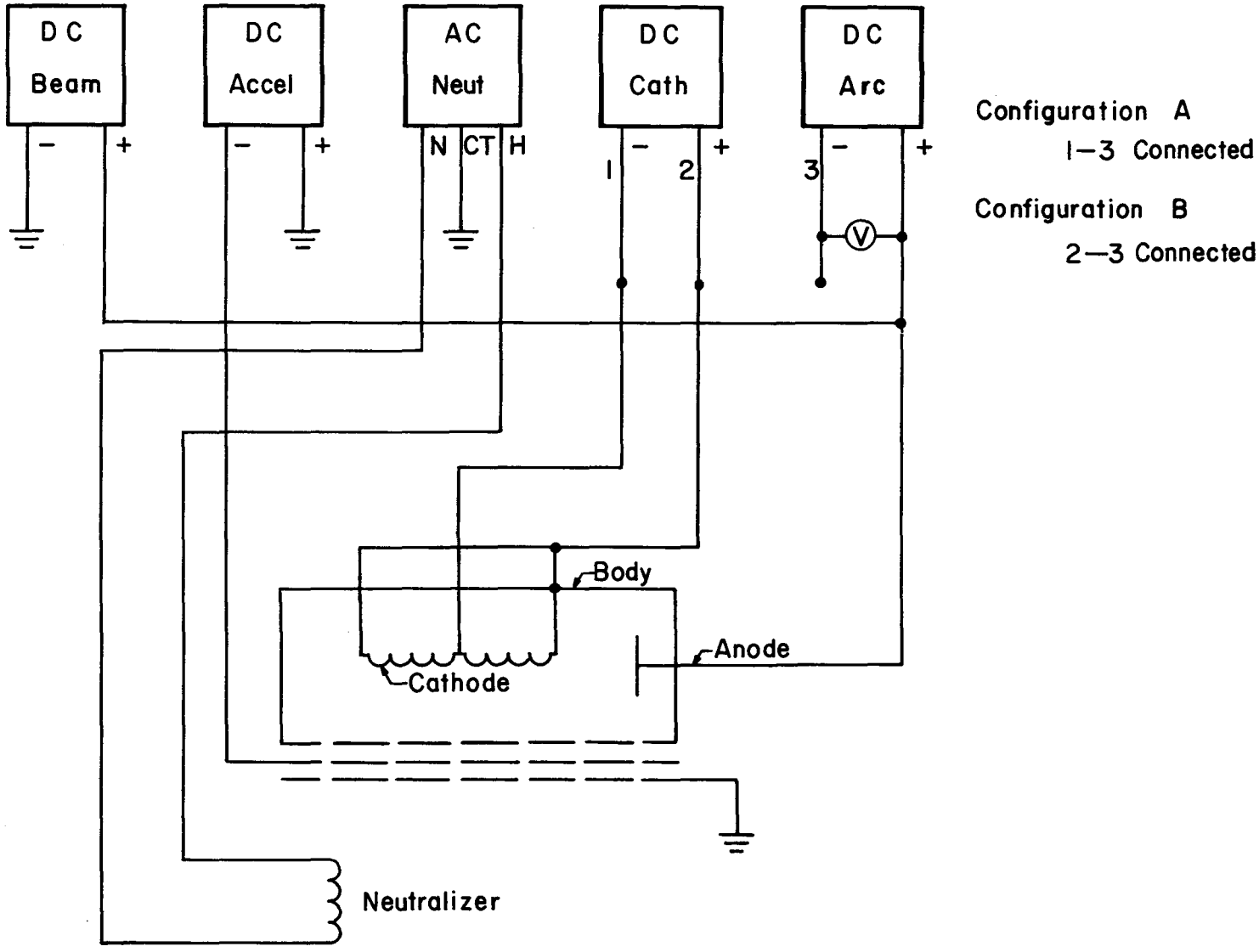

Fig. 4-5. Power supply configurations for the rectangular ion source.

Both configurations resulted in about the same discharge losses, as indicated in Fig. 4-6. All discharge voltages reported in preceding figures are adjusted according to the power supply configuration used.

High Perveance Grid Operation

For these tests Ar flow rates were 360 and 800 mA-equiv. The three-grid accelerator system was aligned and held together with mica. For initial testing small mica washers were used with each alignment screw with the screws only finger tight. However, this method of grid positioning proved inadequate. Data were not repeatable probably because of grid misalignment which resulted from thermal stresses. The grid alignment screws were then tightened with tools and spaced with 1 mm thick mica cut the length of the grids. Discharge losses are shown in Fig. 4-7 to 4-14 for various screen and accelerator grid potentials. The decelerator grid was held at -12 V to reflect neutralizer electrons. This made possible the accurate measurement of ion impingement on the decelerator grid for discharge correction.

Discharge loss trends for different total voltages are shown in Figs. 4-7 and 4-11. The discharge loss tends to increase as the total potential between the screen and accelerator grids is decreased. Limits on maximum attainable beam current are due to power supply limitations.

Discharge loss trends for different screen and accelerator potentials while the total voltage between these two grids was held constant are shown in Figs. 4-8 through 4-10 for an Ar flow of 360 mA-equiv. and in Fig. 4-12 through 4-14 for an 800 mA-equiv. flow. To the first approximation, ion extraction from a discharge plasma is determined by total voltage (Eq. (2-5)). A closer examination, though, will usually show some adverse effect of large decelerations (low R values). Data at

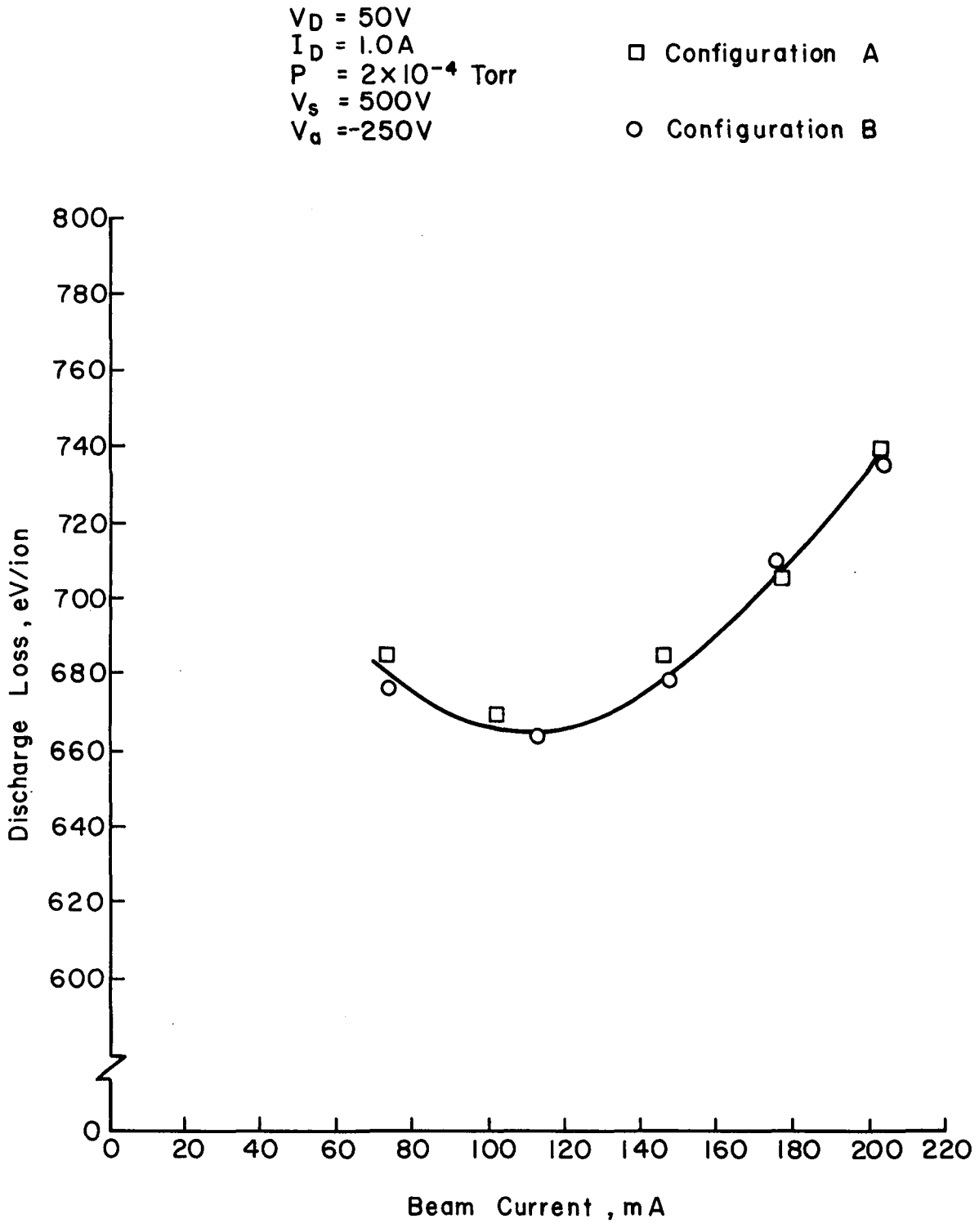

Fig. 4-6. Discharge loss for the two different power supply configurations and the smaller magnetic field integral.

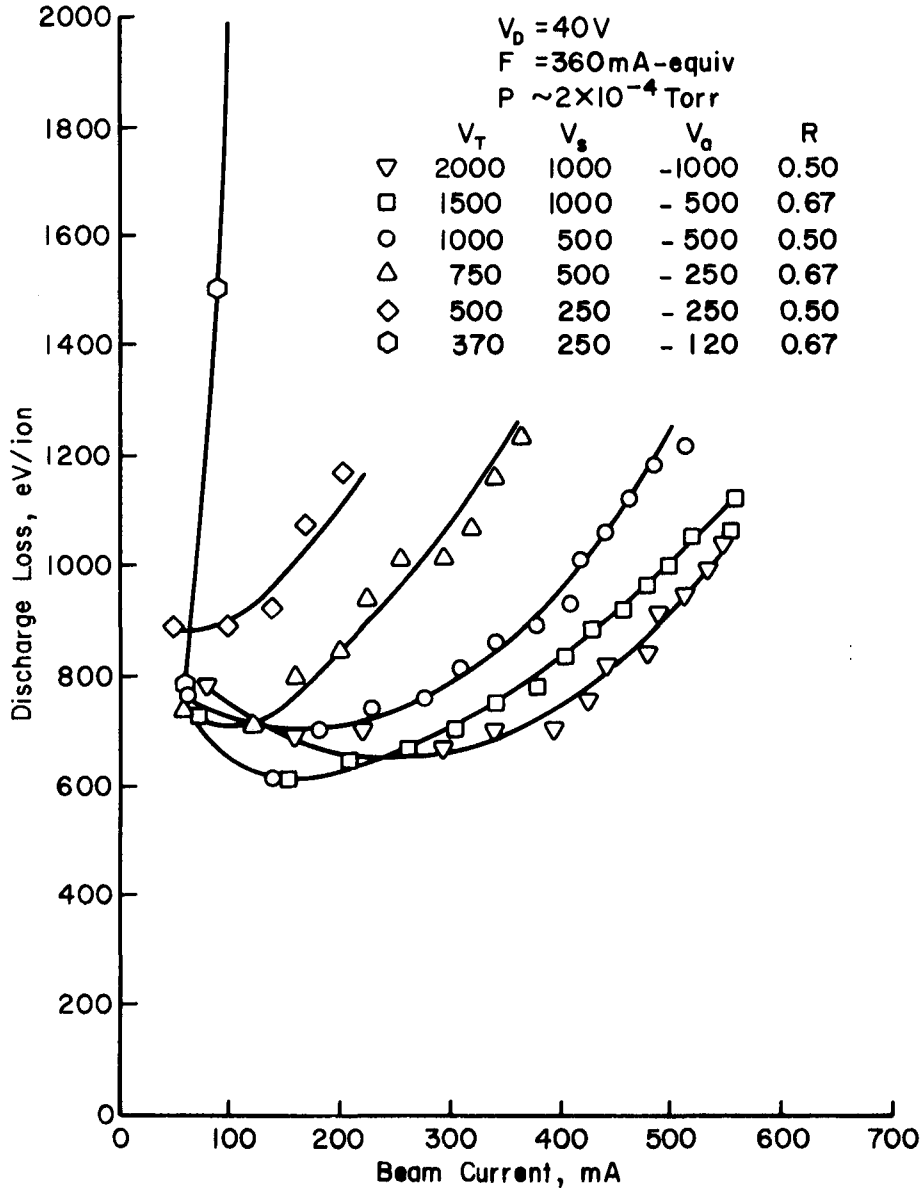

Fig. 4-7. Discharge loss versus beam current for different total voltages (V_T), 360 mA-equiv. Ar flow rate.

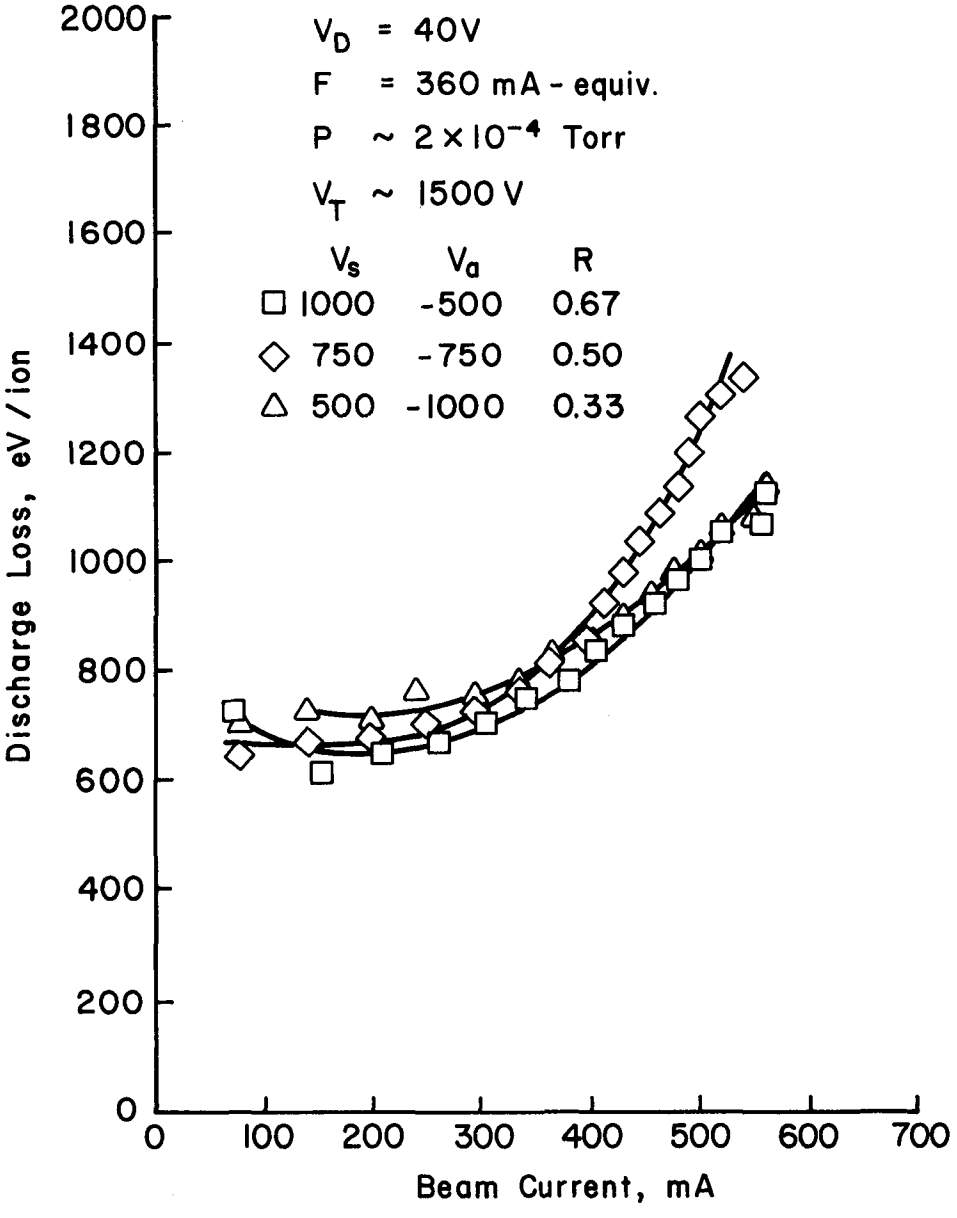

Fig. 4-8. Discharge loss for $V_T \sim 1500$ V and F = 360 mA-equiv.

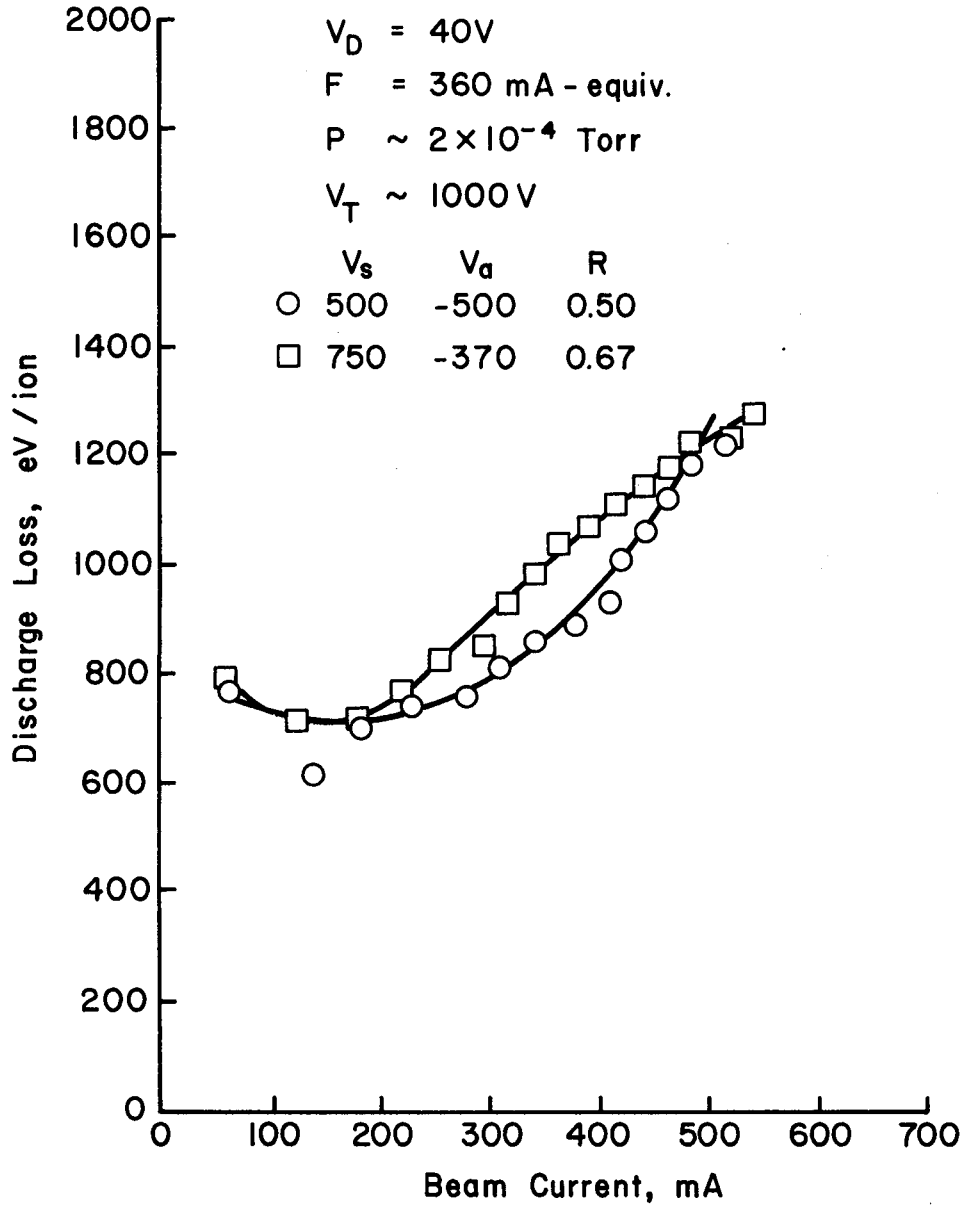

Fig. 4-9. Discharge loss for $V_T \sim 1000$ V and F = 360 mA-equiv.

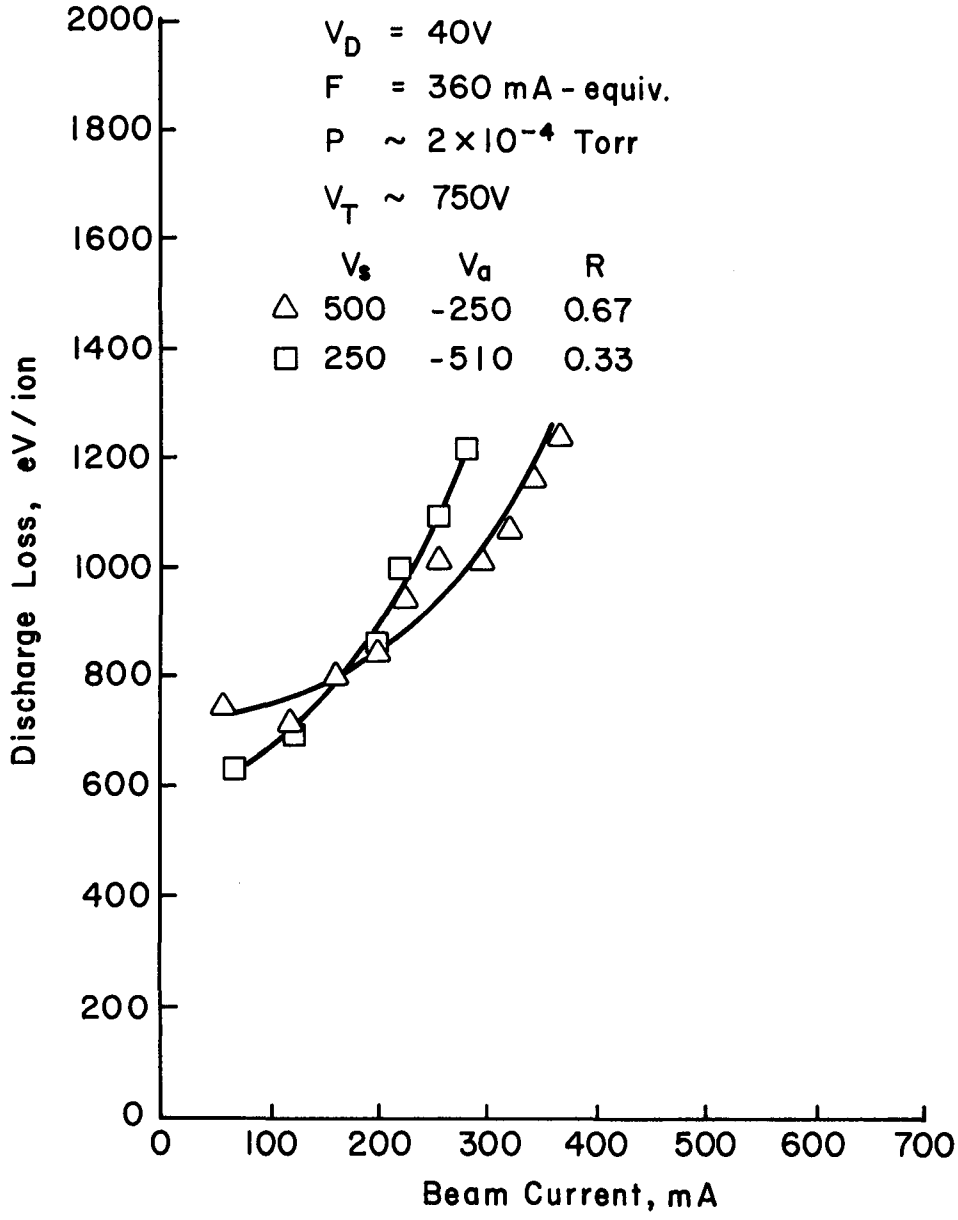

Fig. 4-10. Discharge loss for $V_T \sim 750$ V and F = 360 mA-equiv.

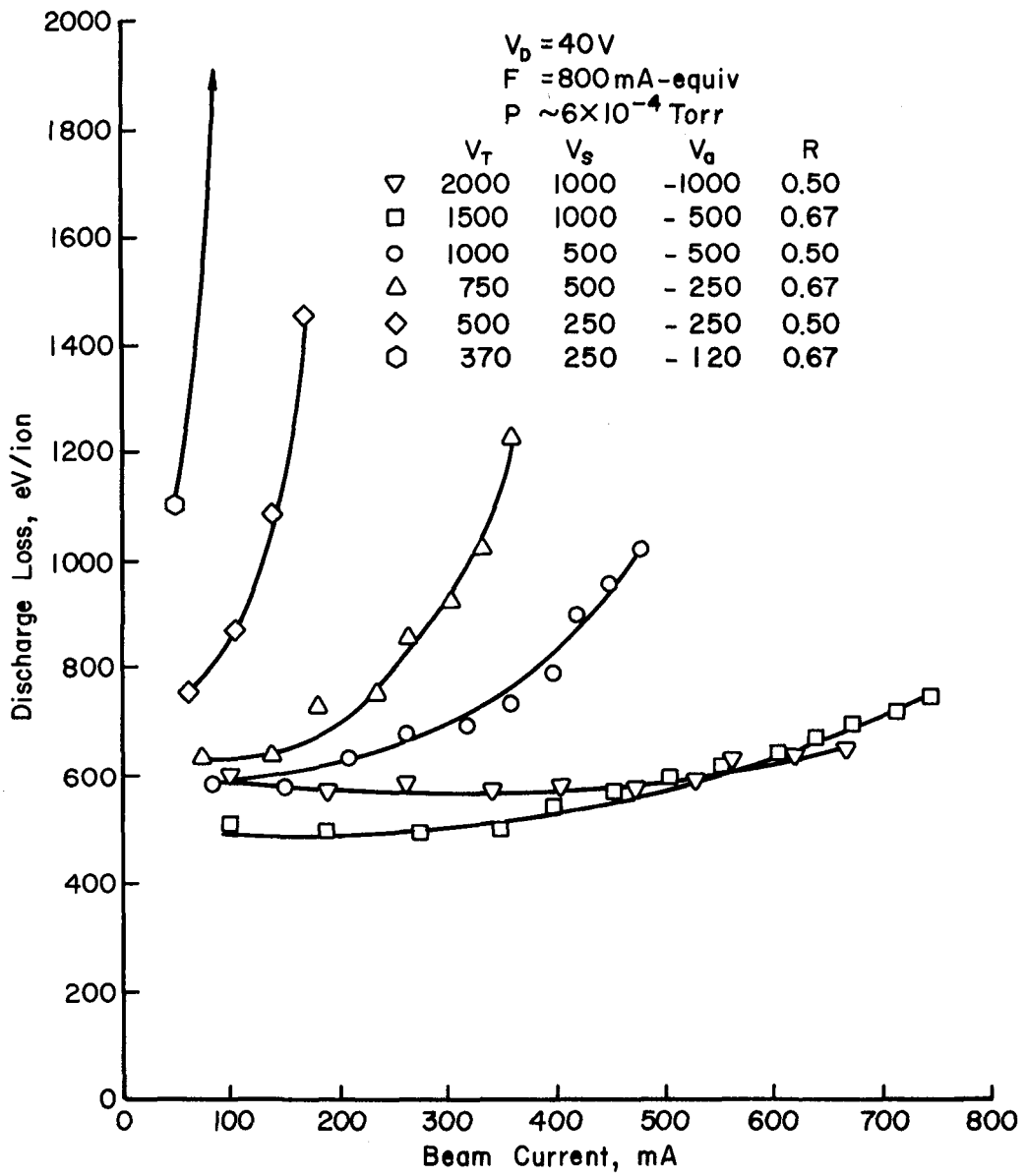

Fig. 4-11. Discharge loss versus beam current for different total voltages (V_T), 800 mA-equiv. Ar flow rate.

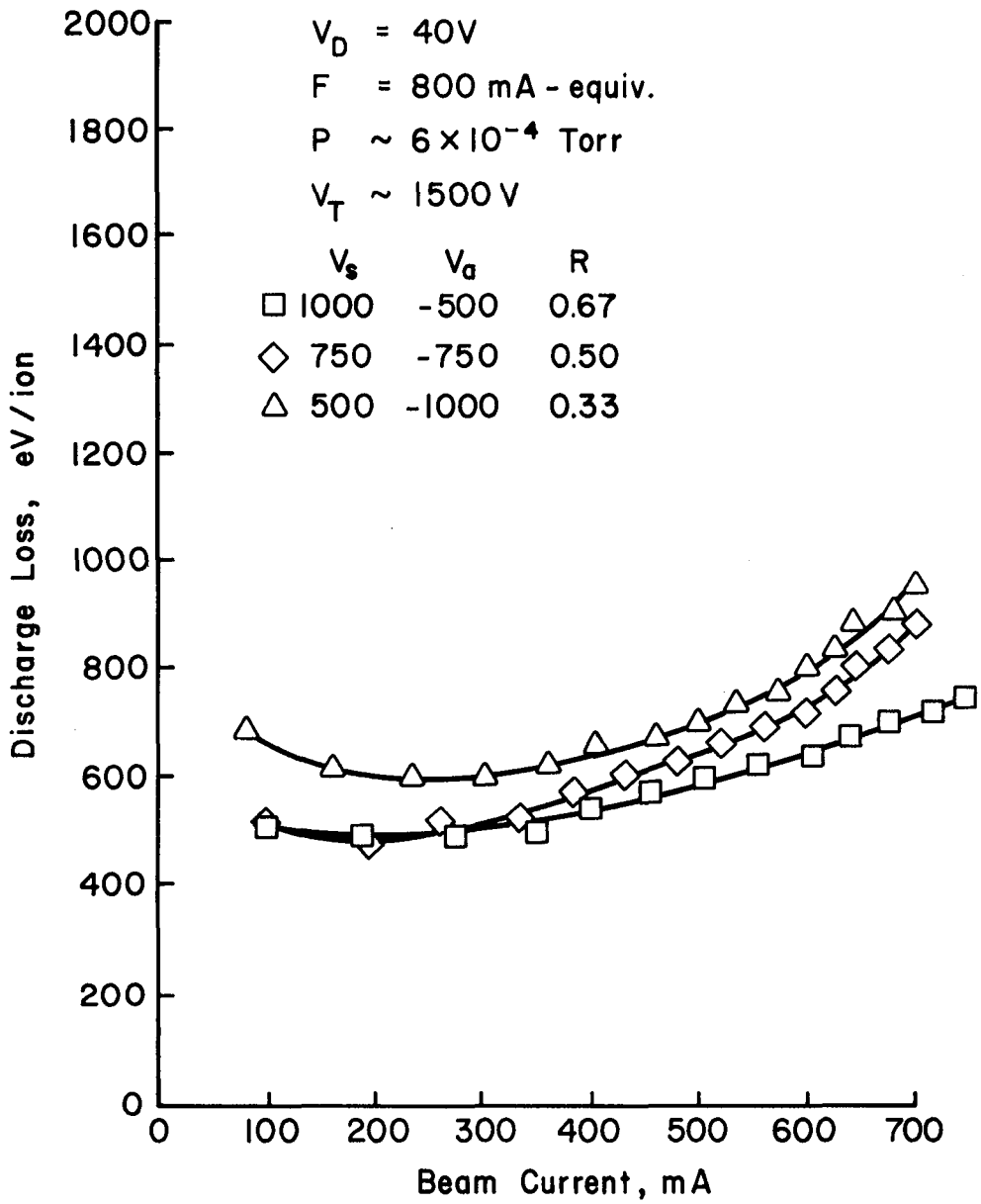

Fig. 4-12. Discharge loss versus beam current for $V_T \sim 1500$ V and F = 800 mA-equiv.

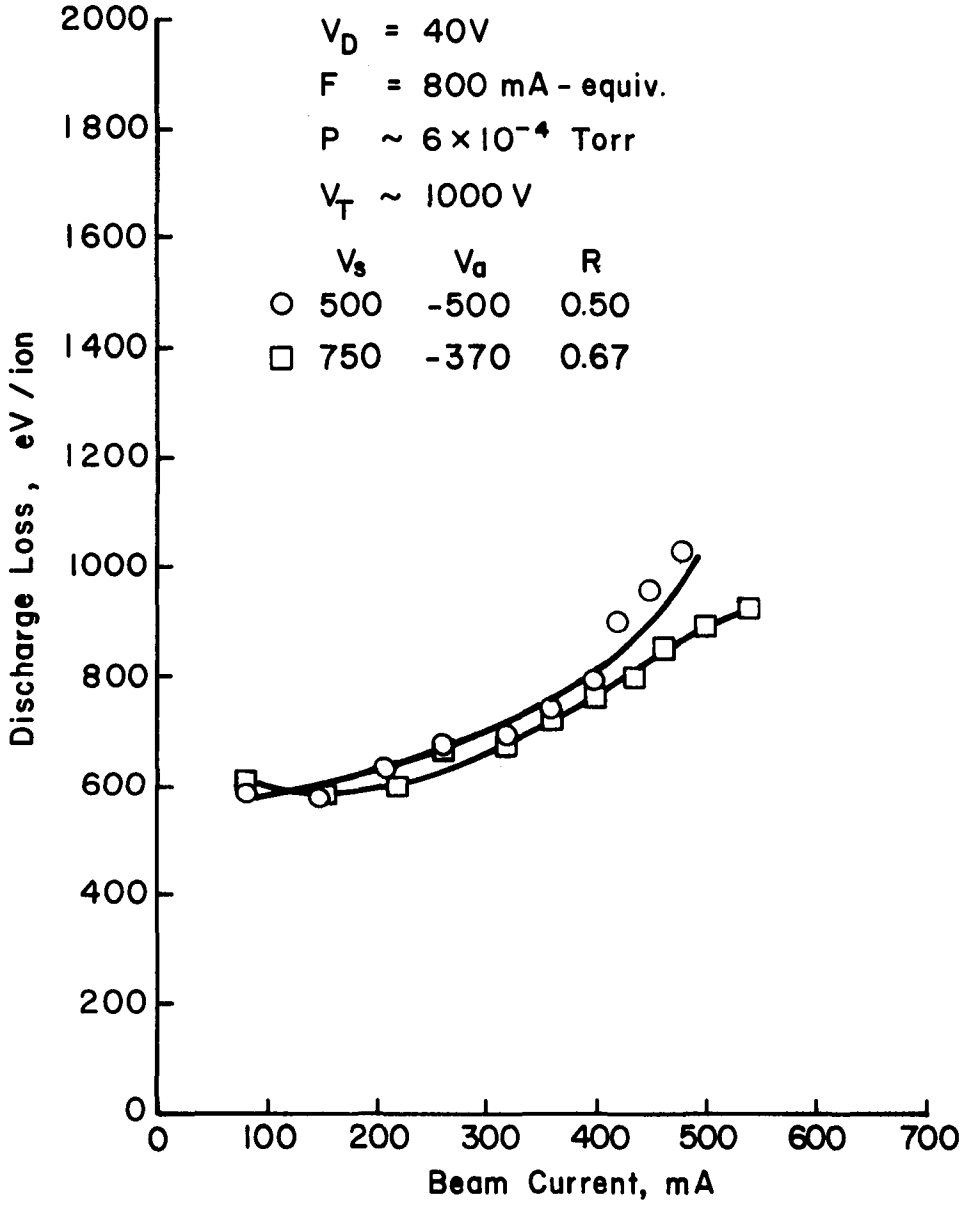

Fig. 4-13. Discharge loss versus beam current for $V_T \sim 1000$ V and F = 800 mA-equiv.

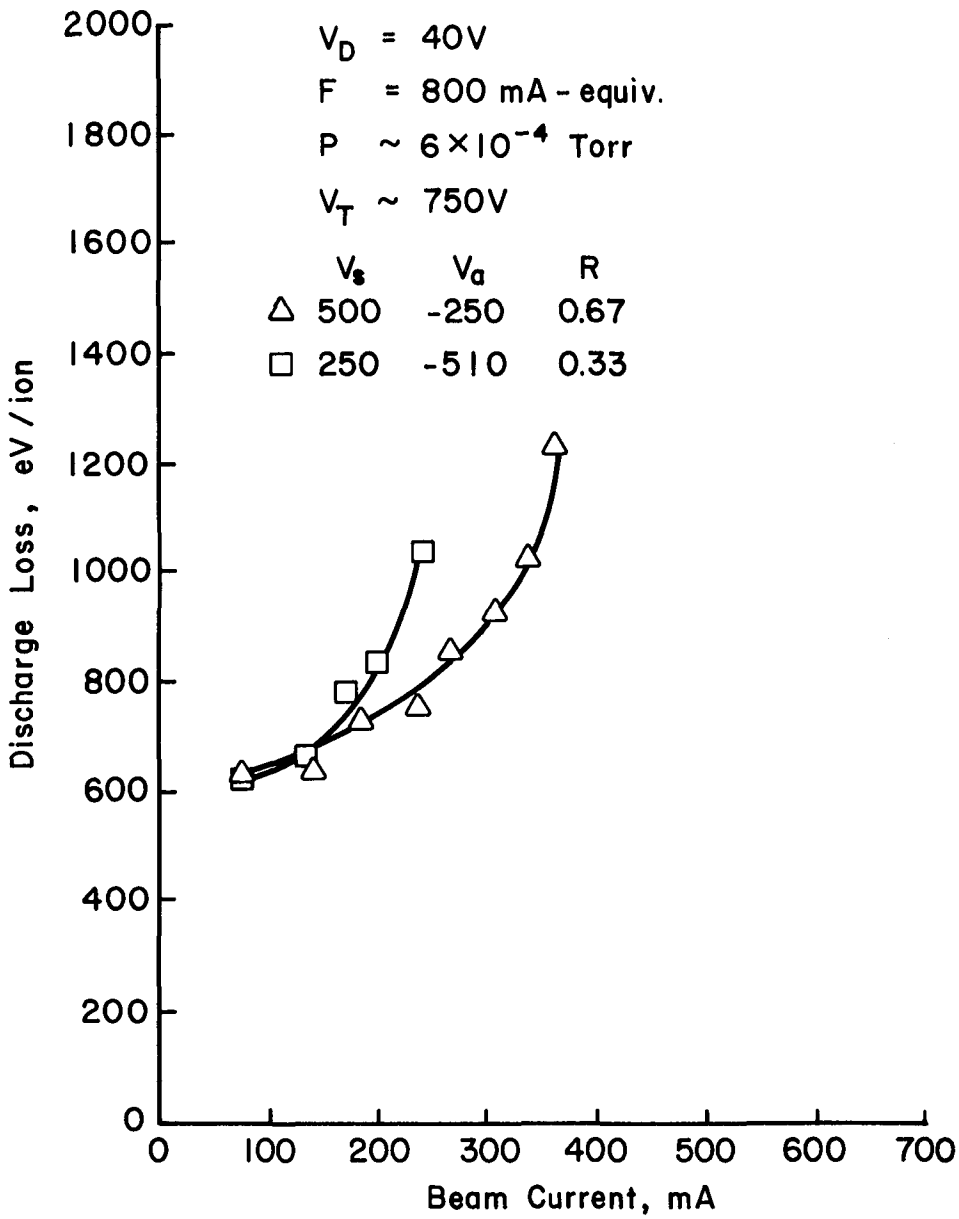

Fig. 4-14. Discharge loss versus beam current for $V_T \sim 750$ V and F = 800 mA-equiv.

a flow rate of 800 mA-equiv. (Figs. 4-12 through 4-14) show that discharge losses tend to increase slightly as the screen voltage is decreased. Data for a 360 mA-equiv. flow rate (Fig. 4-8 through Fig. 4-10) are more ambiguous.

Maximum perveance calculations (Eq. (2-5)) for the data shown in Figs. 4-7 through 4-14 are presented in Tables 4-1 and 4-2. The three-grids optics system appears to be capable of about 2.2×10^{-9} $A/V^{3/2}$ at an R value of about 0.67. The maximum expected normalized perveance per hole was about 2.6×10^{-9} $A/V^{3/2}$ from Fig. 2-10 for an R value of 0.32. Accelerator and decelerator grid impingement currents were subtracted from the total beam currents for perveance calculations. Thermal expansion appeared to be a major reason for the lower experimental perveance. Grid disassembly after prolonged operation showed translation misalignment as much as 20% of the accelerator hole diameter. When misaligned, accelerator grid impingement currents as high as 100 mA and decelerator currents up to 50 mA were observed. After grid realignment these impingement currents decreased for a short time and then increased, showing a clear need for a better grid mounting in a production application. The few mounts used for the ion optics probably also resulted in warping that caused increased grid spacings between the mounts, also indicating a need for more mounts.

Ion Beam Profile

The Ar^+ ion beam was probed at various positions in the 40 cm direction with a Faraday probe consisting of 20 elements lined up at equal intervals in the 5 cm direction. Each of the 20 Ta elements biased to 18 V had an area of 0.32 cm^2 exposed to the ion beam. The elements were surrounded by a wire mesh screen with a -24 V potential

Table 4-1. Maximum Normalized Perveance per Hole for Various Grid Potentials for a Flow Rate of 360 mA-equiv.

Normalized Perveance per Hole ($A/V_t^{3/2}$)	V_s(V)	V_a(V)	I_B(mA)
1.03×10^{-9}	250	-120	53
2.11	250	-250	170
1.52	250	-510	230
2.18	500	-250	323
2.02	500	-500	459
1.26	500	-1000	527
1.86	750	-370	501
1.22	750	-750	511
1.28	1000	-500	534
0.77	1000	-1000	497

Table 4-2. Maximum Normalized Perveance per Hole for Various Grid Potentials for a Flow Rate of 800 mA-equiv.

Normalized Perveance per Hole ($A/V_t^{3/2}$)	V_s(V)	V_a(V)	I_B(mA)
0.72×10^{-9}	250	-120	37
1.37	250	-250	110
1.28	250	-510	193
1.84	500	-250	272
1.71	500	-500	390
1.51	500	-1000	630
1.76	750	-370	475
1.52	750	-750	635
1.66	1000	-500	693
0.93	1000	-1000	610

for electron deflection. The beam was fairly uniform in the 40 cm direction as seen in the profile in Fig. 4-15. Figures 4-16 and 4-17 show typical profiles in the 5 cm direction for various beam currents. Charge-exchange corrections used in these beam profiles were found by integrating both profiles (5 and 40 cm directions) with distance and comparing to the measured beam current. The charge-exchange fractions (that is, the fractions of I_B which have undergone charge-exchange) for pressures of 0.6, 1.0 and 6.0×10^{-4} Torr were found to be 0.15, 0.22 and 0.57.

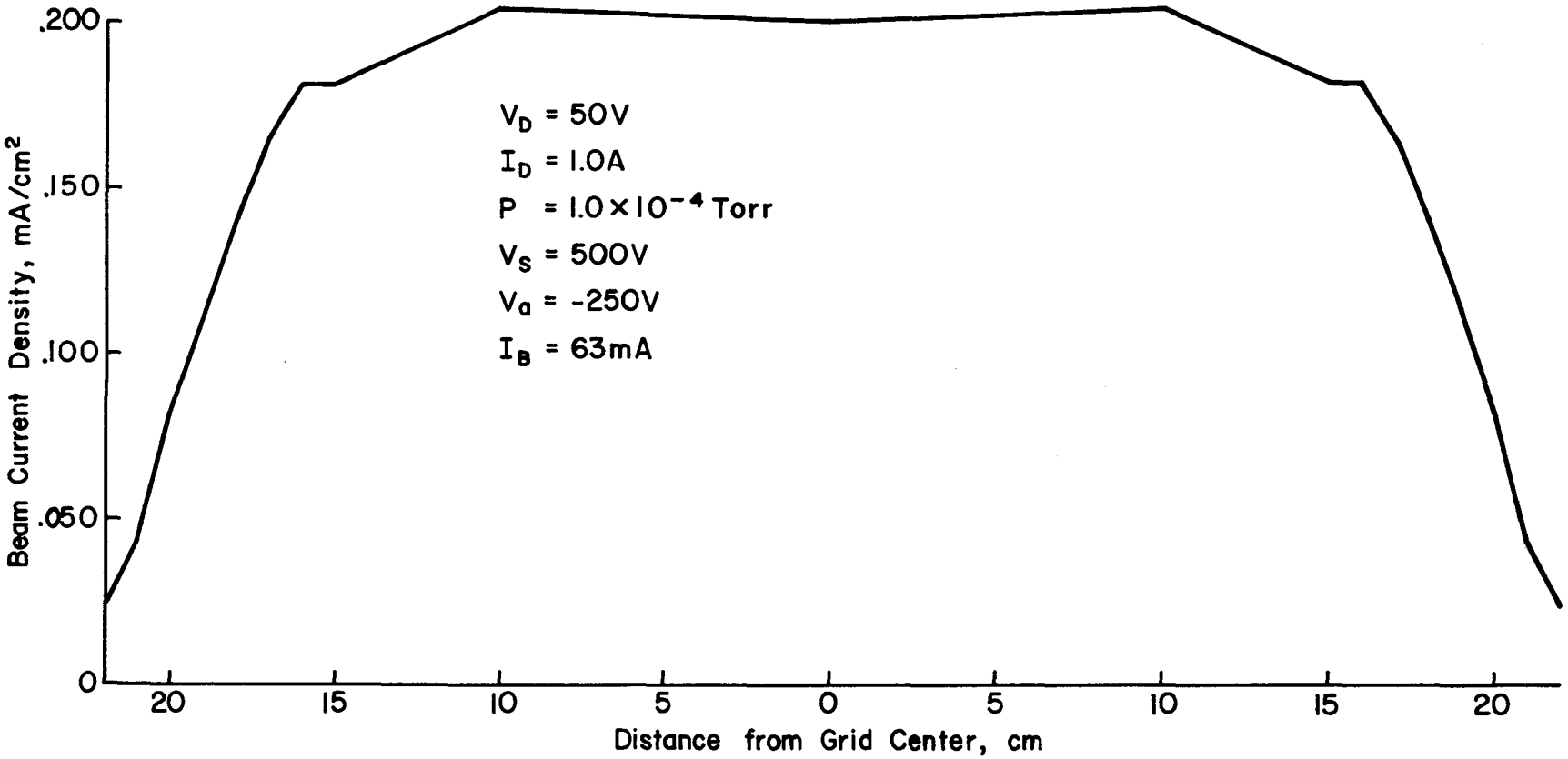

Fig. 4-15. Ion beam current density profile taken along the 40 cm direction at a distance of 10 cm from the grids.

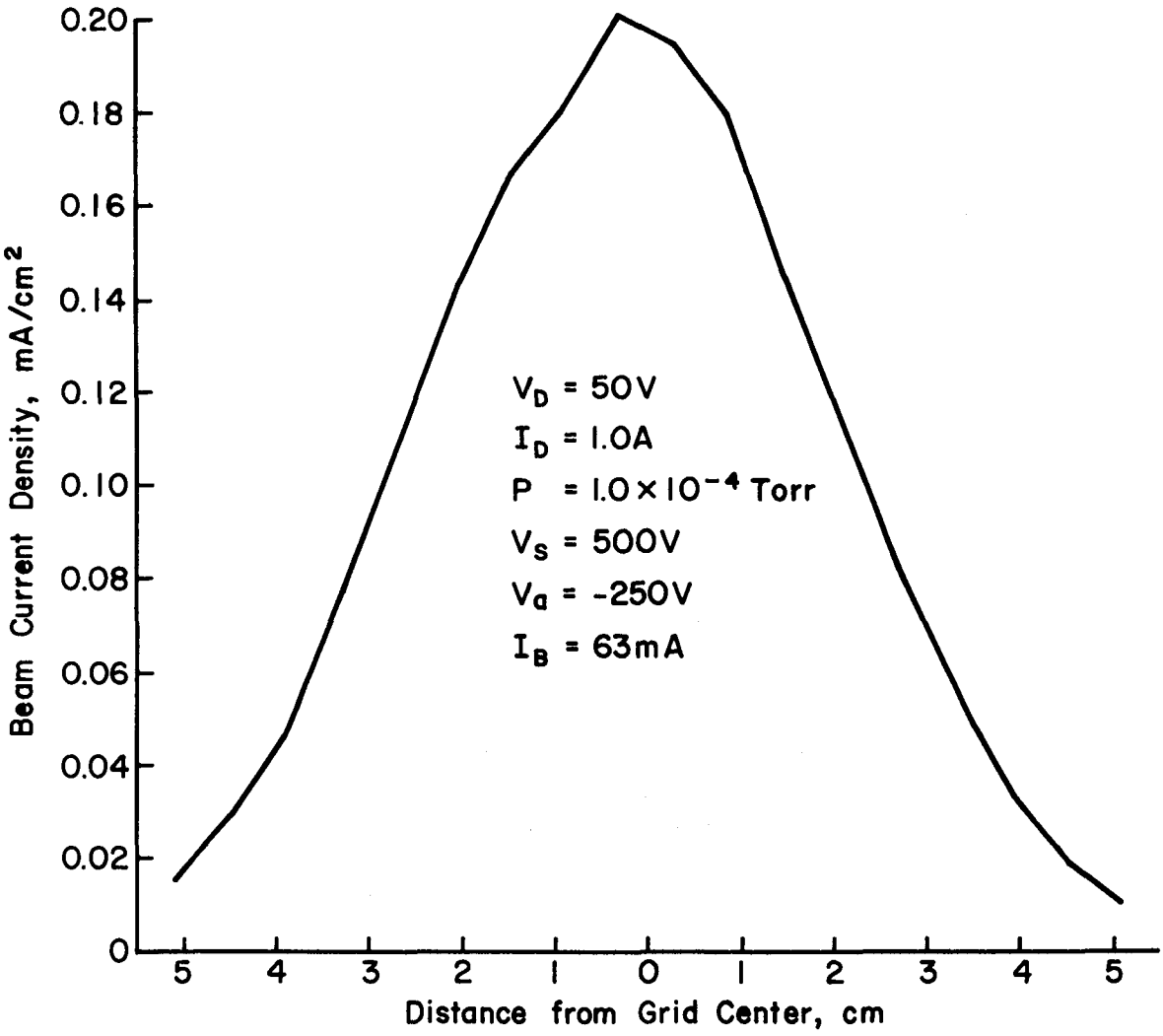

Fig. 4-16. Ion beam current density profile taken across the 5 cm direction at a distance of 10 cm from the grids.

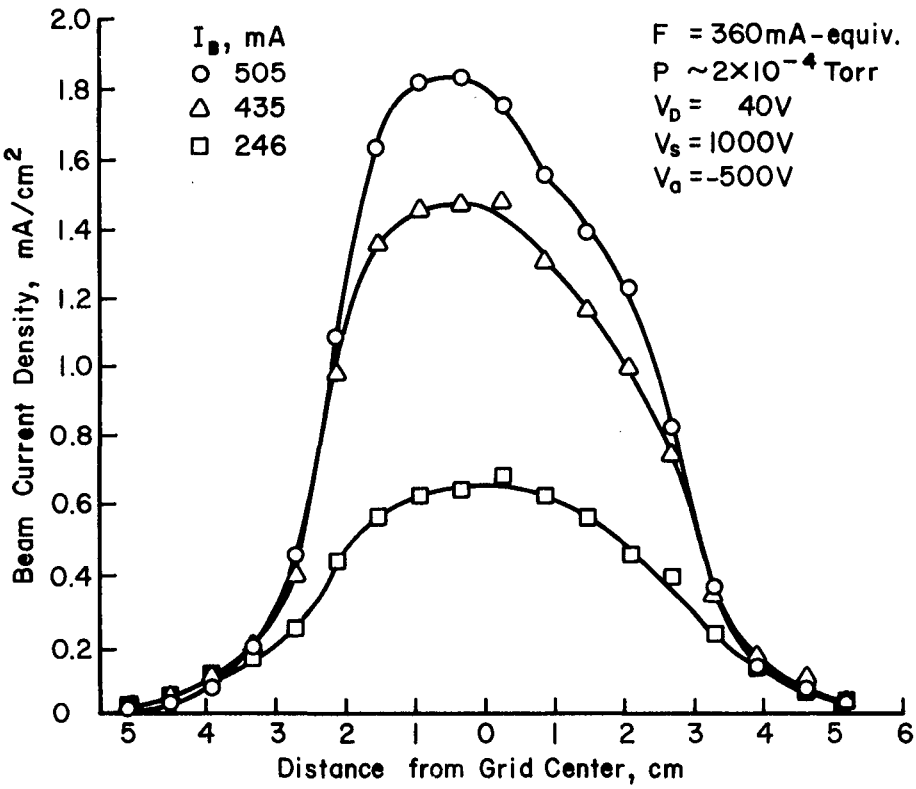

Fig. 4-17. Ion beam current density profiles taken across the 5 cm direction at a distance of 10 cm from the grids at high total beam currents.

V. USE OF MULTIPLE SOURCES FOR WIDE PROCESSING PATHS

As discussed in the Introduction (see Fig. 1-1 in that section), multiple sources can be used to process wider paths than would be possible with a single source. A crucial parameter in the use of multiple sources is the amount of overlap required for uniform coverage. This overlap should be chosen to minimize departures from uniformity across the path width. The means of evaluating this uniformity and the experimental evaluation for various operating conditions and amounts of overlap are the subject of this section.

The ion source used for the data of this section was the final configuration of the preceding section (small magnetic field integral). This configuration was operated at a discharge potential difference of 50 V and discharge currents of 1-4 A. Bell-jar pressures during operation were 0.6, 1.0, 1.9, and 6.0×10^{-4} Torr. The ion energy was held constant at 500 eV. The accelerator was operated at -55, -250, and -500 V, which corresponded to net-to-total voltage ratios (R) of 0.90, 0.67, and 0.50. The decelerator grid was held constant at 0 V for all tests.

Beam profiles were taken with a Faraday probe consisting of 20 elements (biased +18 V) encased within a screen (biased -24 V) to exclude beam-plasma electrons. This probe was located 10 cm from the ion-source grids.

The Faraday probe survey positions and probe element placements are indicated in Fig. 5-1. The "x" direction in this figure is assumed to be the direction of substrate motion. The concern for uniformity, then, is in the "y" direction. In moving through the ion beam in the x direction, an object being processed will see an ion beam profile

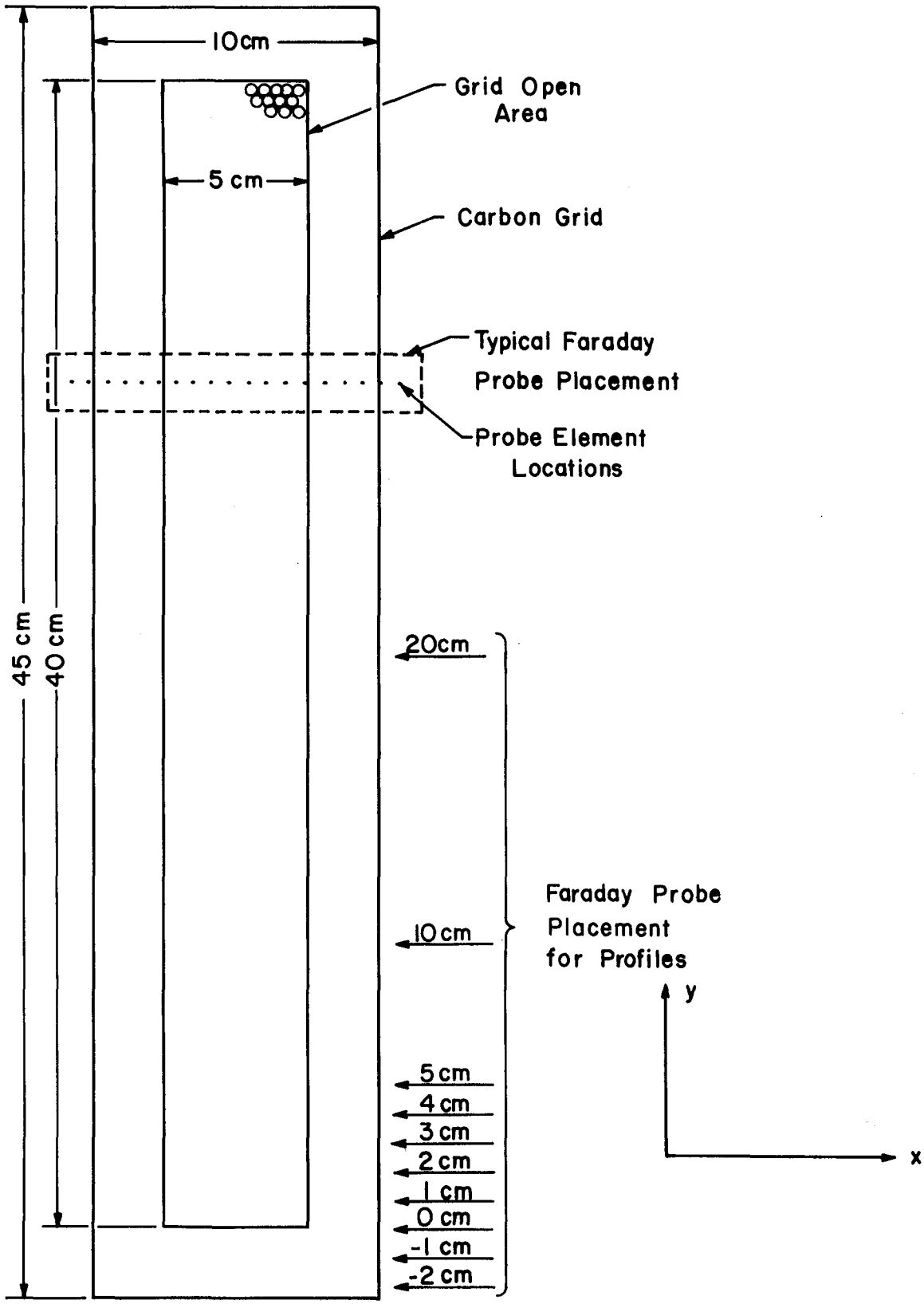

Fig. 5-1. Probe placement for beam profile measurements.

(as indicated in Fig. 4-7 of the preceding section), obtained from the probe oriented as indicated in Fig. 5-1. What is of interest in this profile is the integrated dose of bombardment that would be received in passing through in the x direction. For the purposes of this study, the integral of current density over distance will be used, with units of mA/cm. This integral must be divided by velocity to obtain the ion-beam dose in the usual units of mA-min/cm^2 or mA-hr/cm^2.

The y locations for determining the beam profiles are also shown in Fig. 5-1. These locations are spaced closer near the end of the ion beam, where the variation with distance is more pronounced. A typical plot of integrated profiles is shown in Fig. 5-2. The abcissa in this figure represents the y direction. while the ordinate is the integrated value of a profile in the x direction. With the beam 40 cm long in the y direction, the location 20 cm from the center of the grids in Fig. 5-2 corresponds to 0 cm in Fig. 5-1.

Beam profiles were superimposed to determine the effect of different amounts of overlap. Because the data were obtained in 1 cm intervals in the y direction, overlaps were investigated in steps of 1 cm, as shown in Figs. 5-3 through 5-6 for the overlap regions. For the operating conditions used for Figs. 5-2 through 5-6, the most uniform processing would be expected with 0 cm of overlap. The overall integral profile for two ion sources is shown for this amount of overlap in Fig. 5-7.

Note that the ion sources are symmetrical in the y direction. The investigation of overlap therefore only needs to be carried out with two similar sources to be applicable to any number of sources.

Overall integral profiles for optimum overlap, similar to Fig. 5-7, were also found for other operating conditions. These profiles are

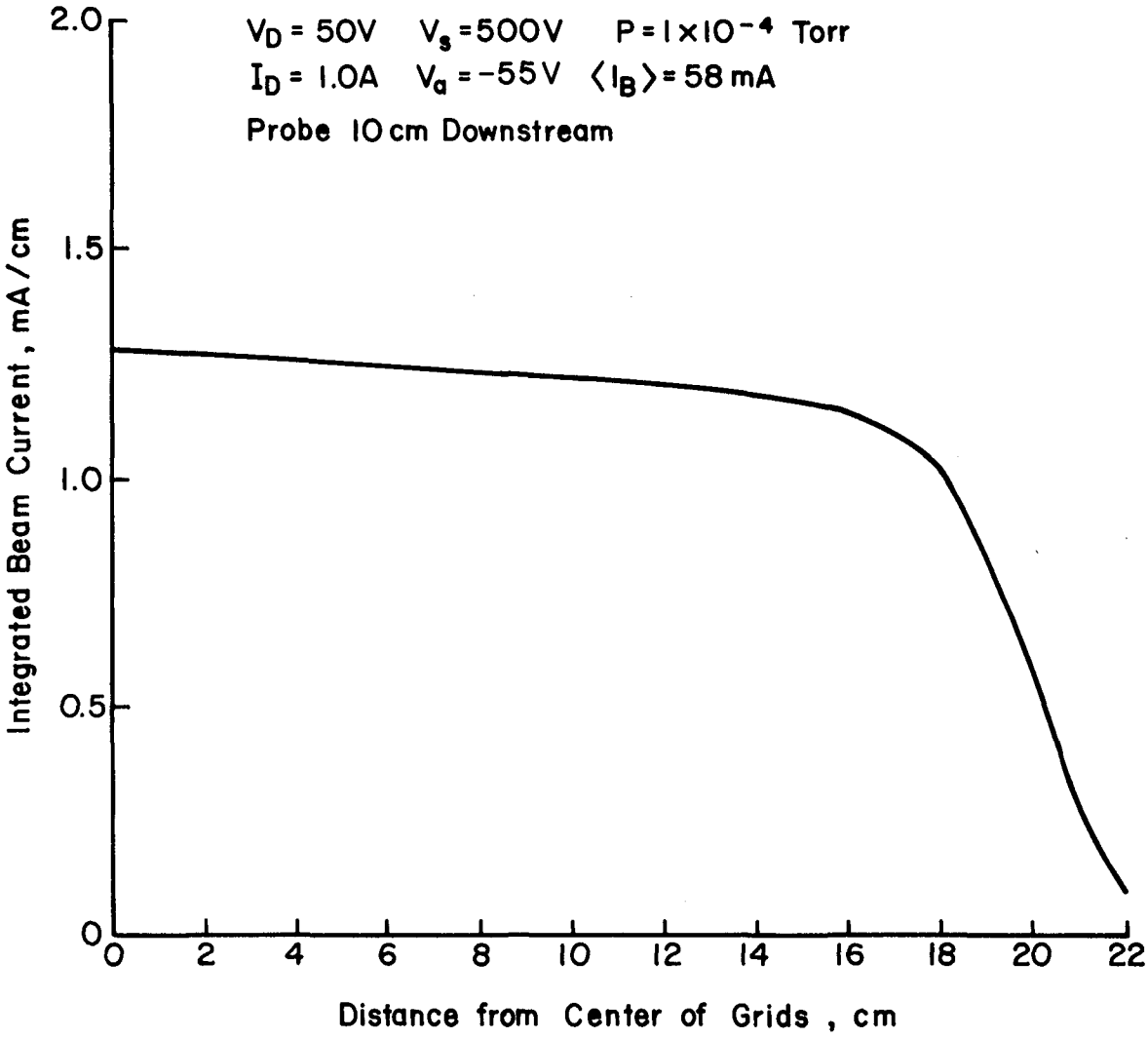

Fig. 5-2. Integrated beam current measured along the 40 cm direction.

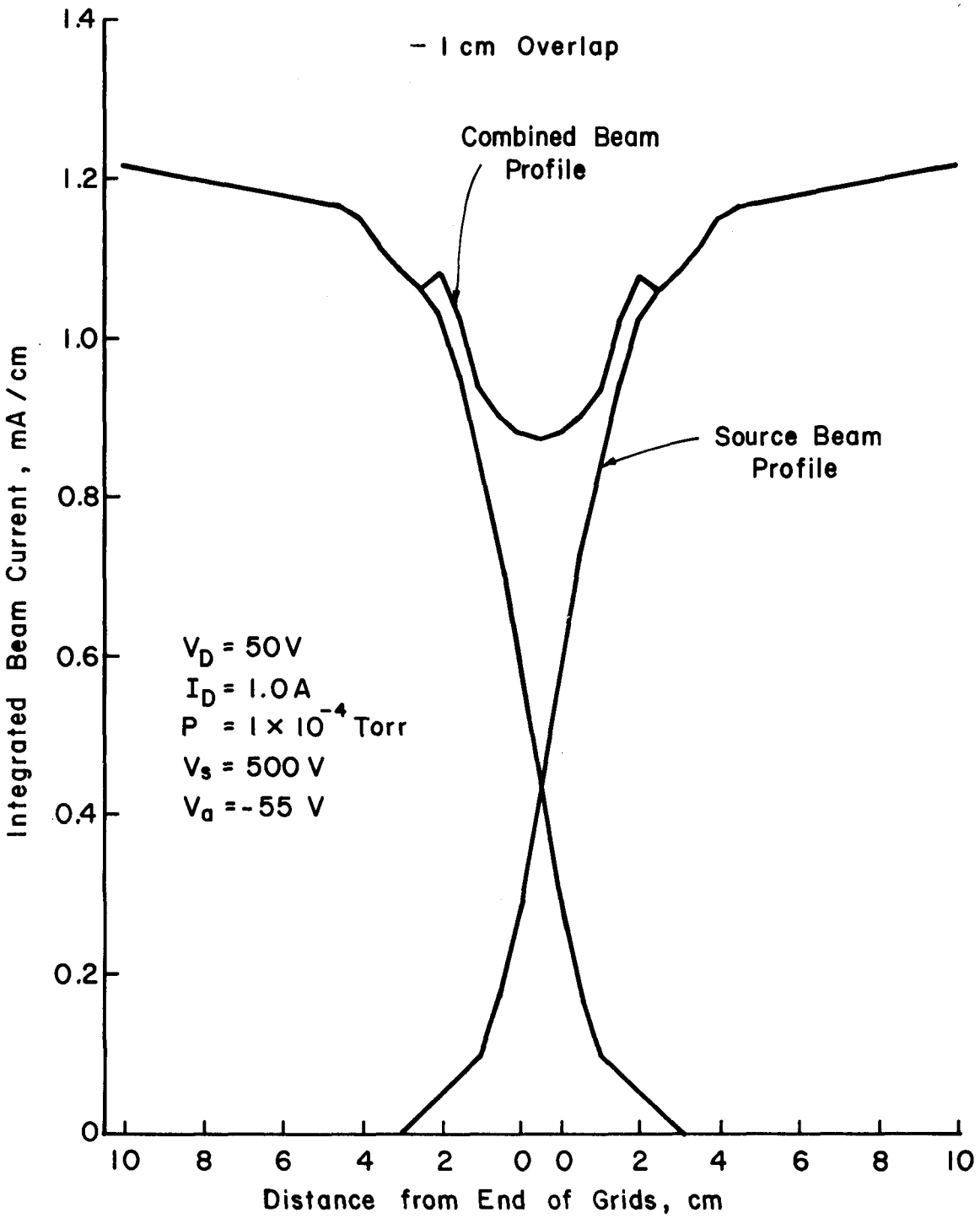

Fig. 5-3. Ion source integrated beam current profile with the grid ends separated by 1.0 cm.

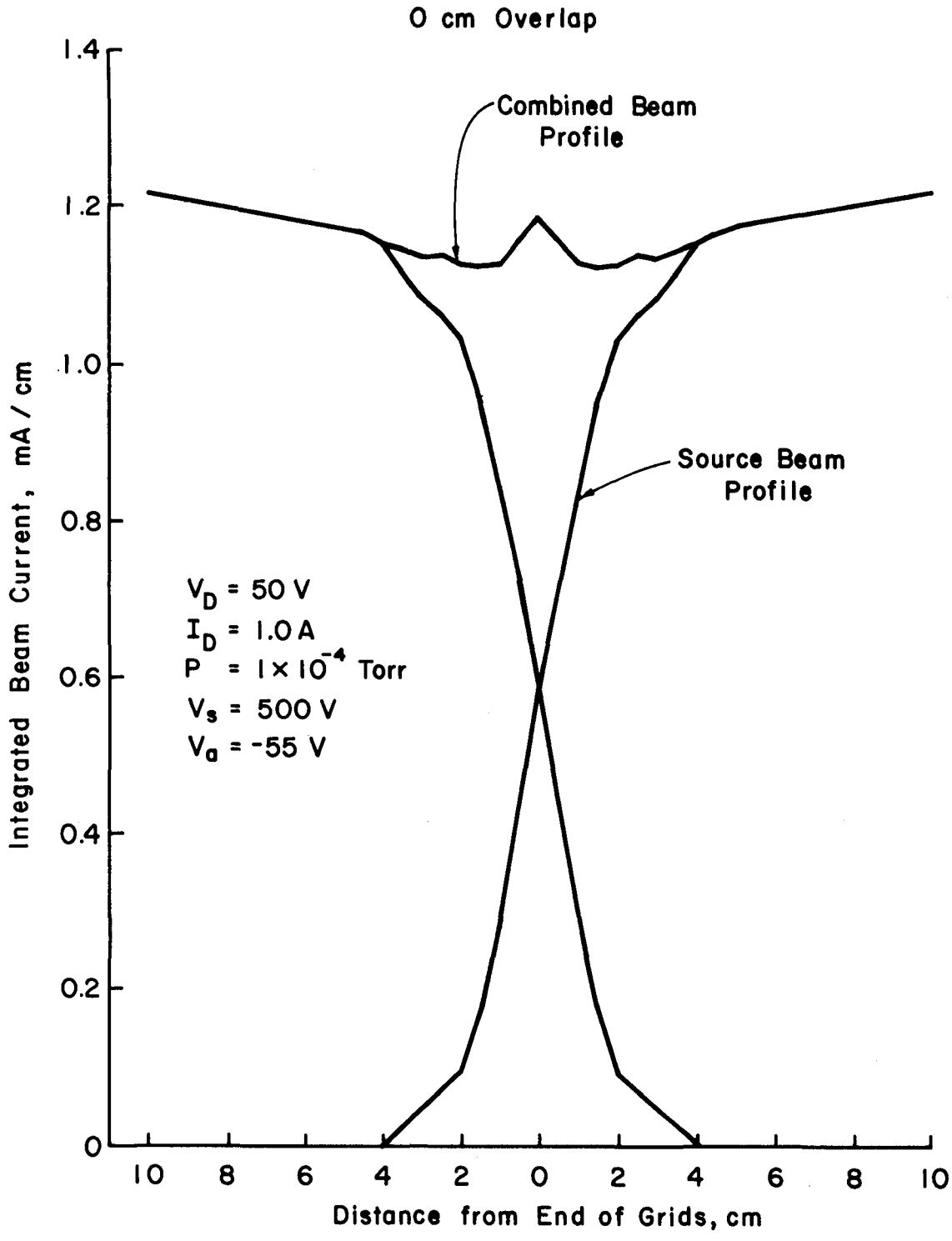

Fig. 5-4. Ion source integrated beam current profile at no overlap.

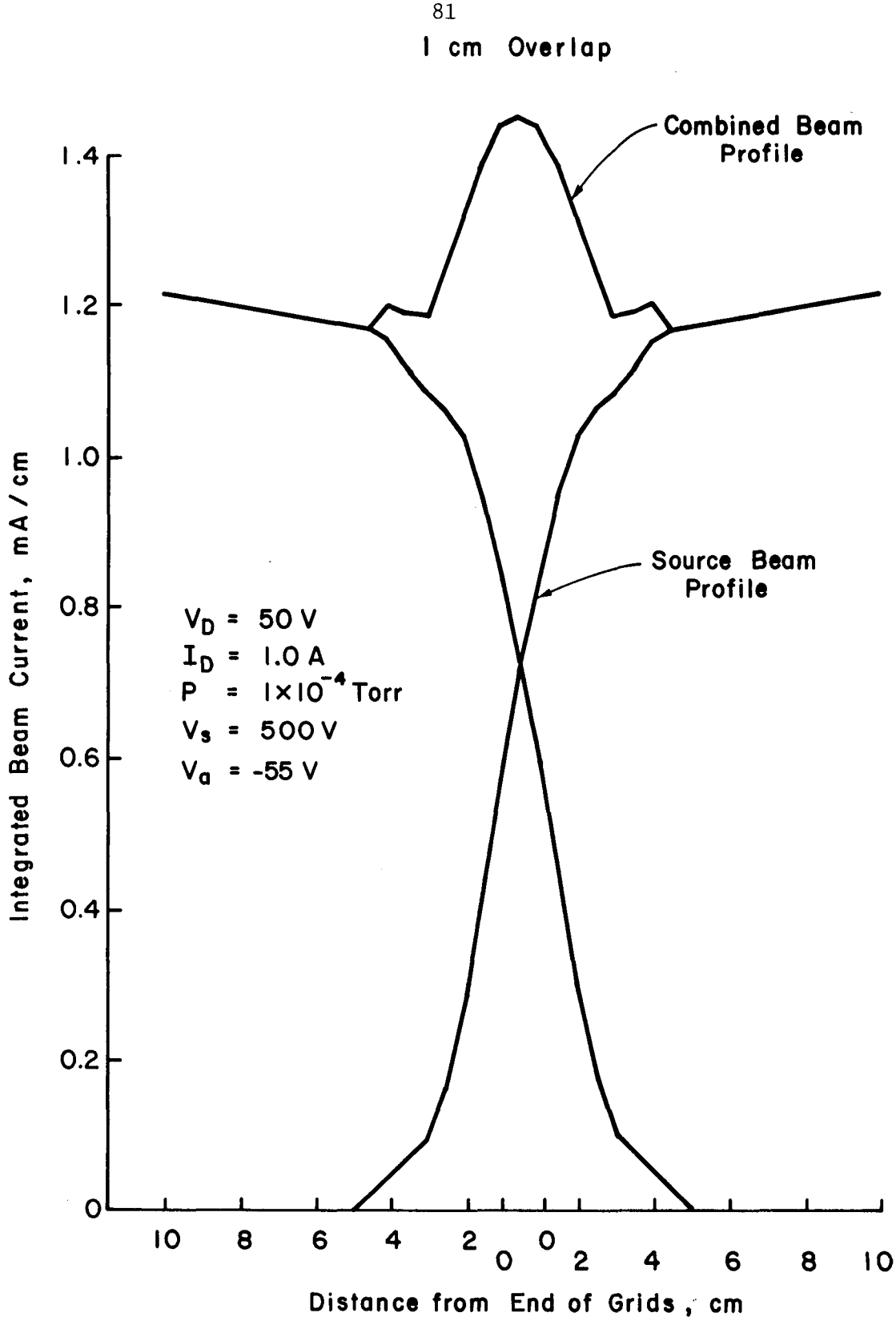

Fig. 5-5. Overlapped ion source integrated beam current profile at 1.0 cm overlap.

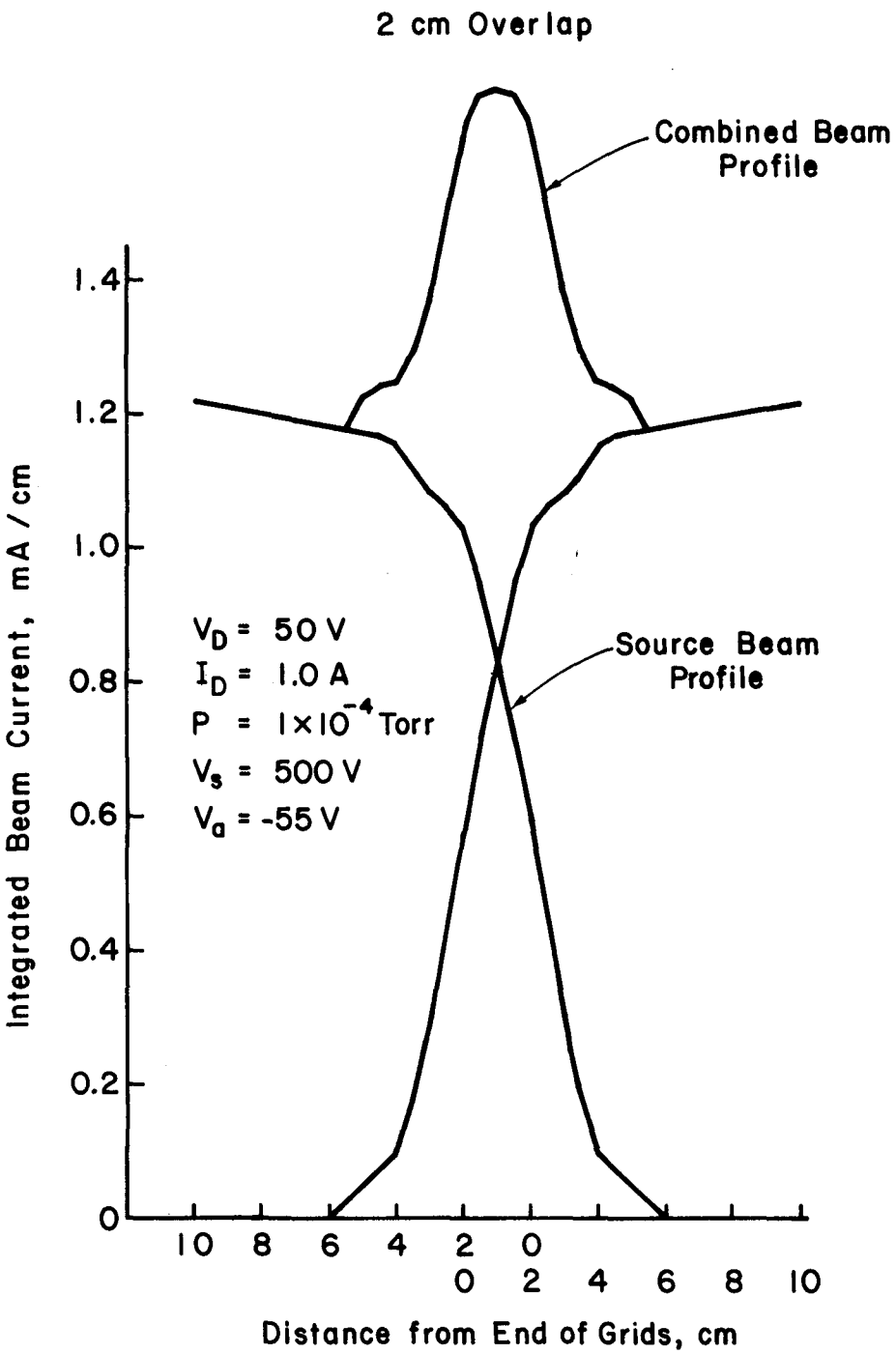

Fig. 5-6. Overlapped ion source integrated beam current profile at 2.0 cm overlap.

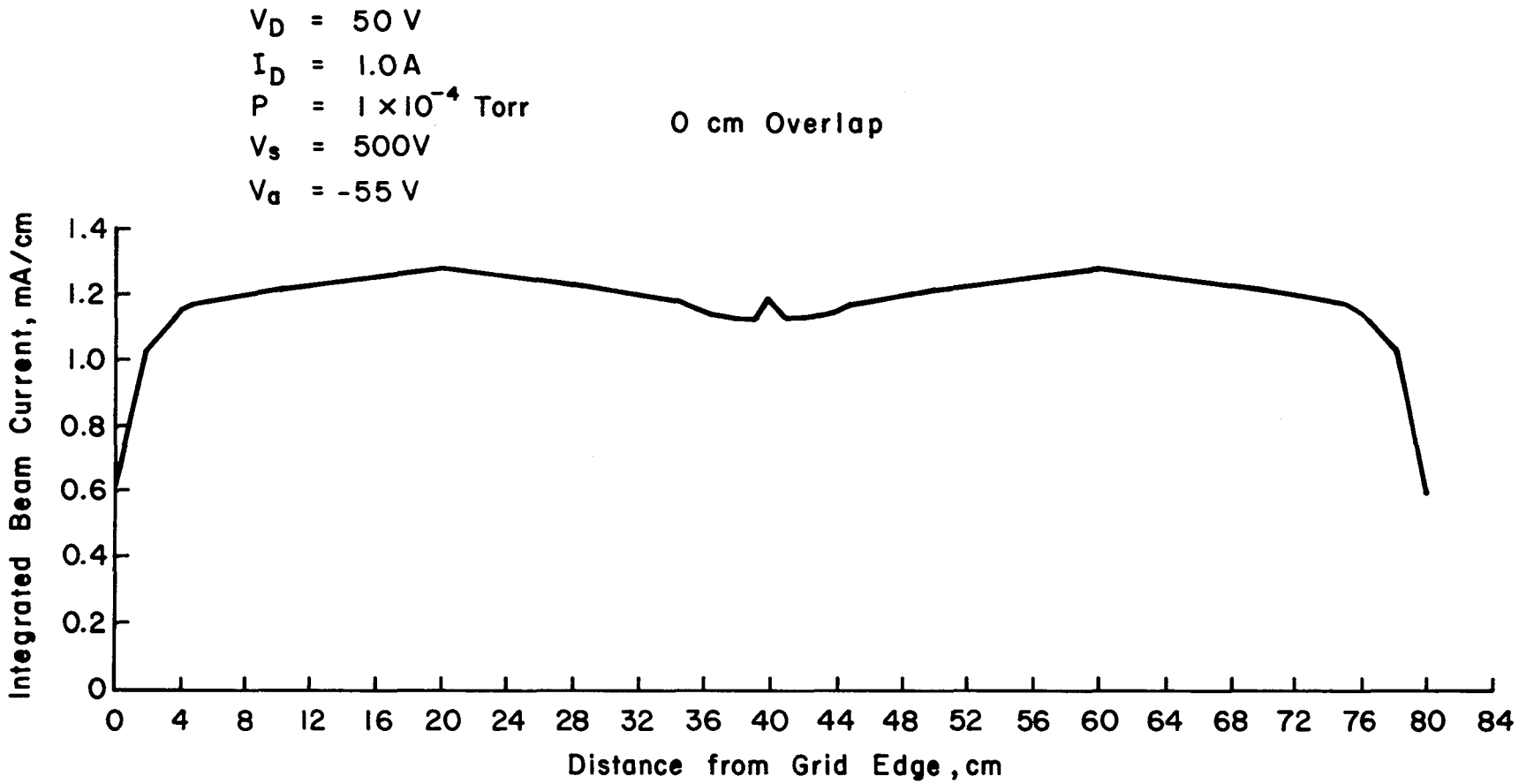

Fig. 5-7. Integrated beam current profile for the best overlap position at 1×10^{-4} Torr and R = 0.90.

shown in Figs. 5-8 through 5-15. The maximum deviations from uniformity, together with the optimum overlaps (± 1/2 cm) used, are shown in Table 5-1 for the same operating conditions. Data were also obtained at 1.9×10^{-4} Torr, as indicated at the beginning of this section, but were similar to those obtained at 1.0×10^{-4} Torr.

Table 5-1. Maximum Deviation in Integrated Beam Current for Overlapped Rectangular Ion Sources.

Pressure (Torr):	6×10^{-5}	1×10^{-4}	6×10^{-4}
R (V_{net}/V_{total})			
0.90	+4%	0%	+15%
	-14%	-7%	-7%
	(1 cm)	(0 cm)	(1 cm)
0.67	+3%	+8%	0%
	-11%	-9%	-9%
	(2 cm)	(2 cm)	(1 cm)
0.50	0%	+6%	+9%
	-15%	-15%	-7%
	(2 cm)	(2 cm)	(2 cm)

A general comparison can be made of the results obtained with what might be expected from a theoretical viewpoint. Assume that the ion current density is completely uniform at the plane of the ion optics. Also assume that the angular distribution of ion trajectories is exactly the same for all ion-optics apertures. For these assumptions, a completely uniform integrated profile would, at all times, be obtained at 0 cm overlap.

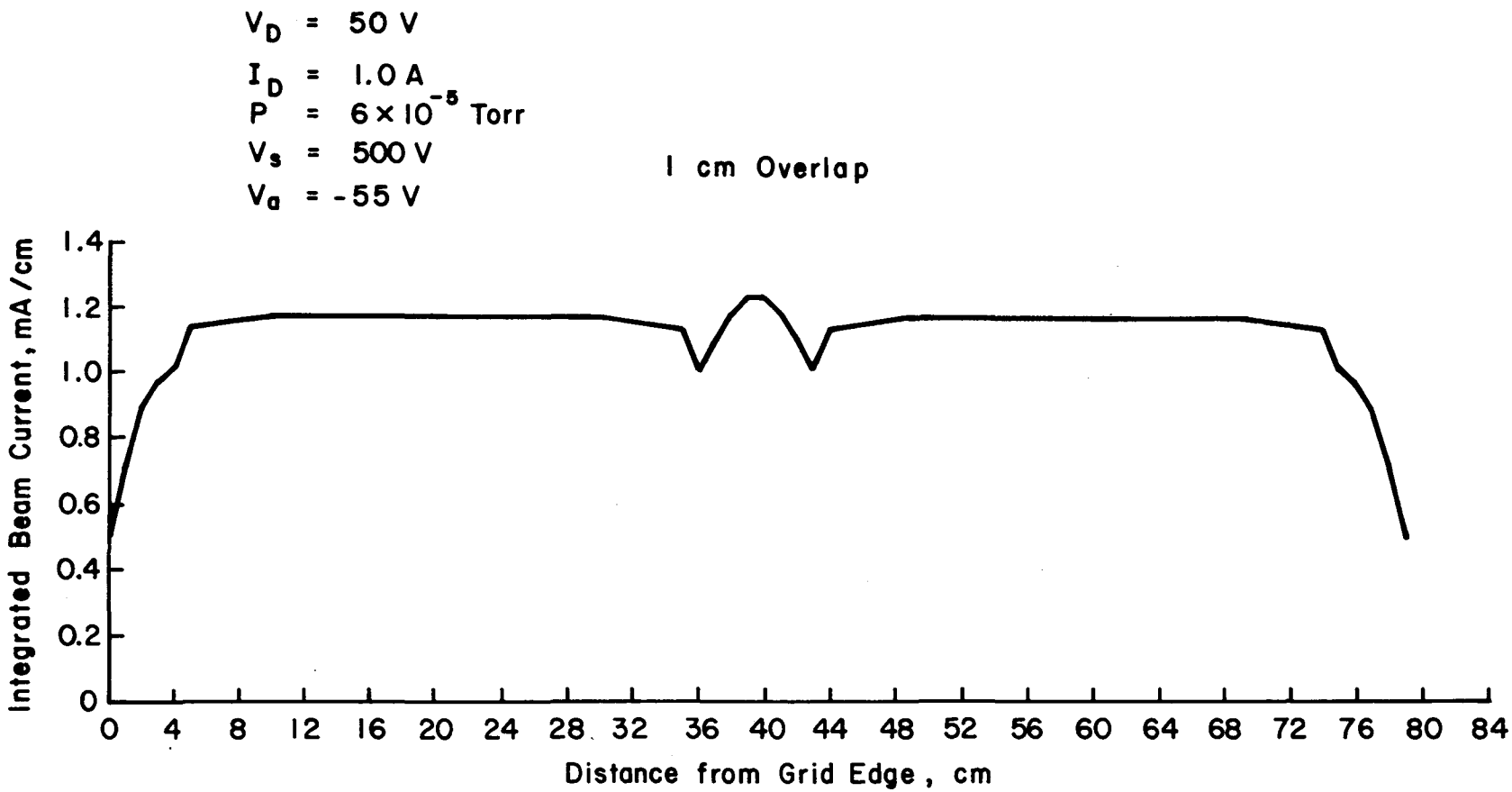

Fig. 5-8. Integrated beam current profile for the best overlap position at 6×10^{-5} Torr and R = 0.90.

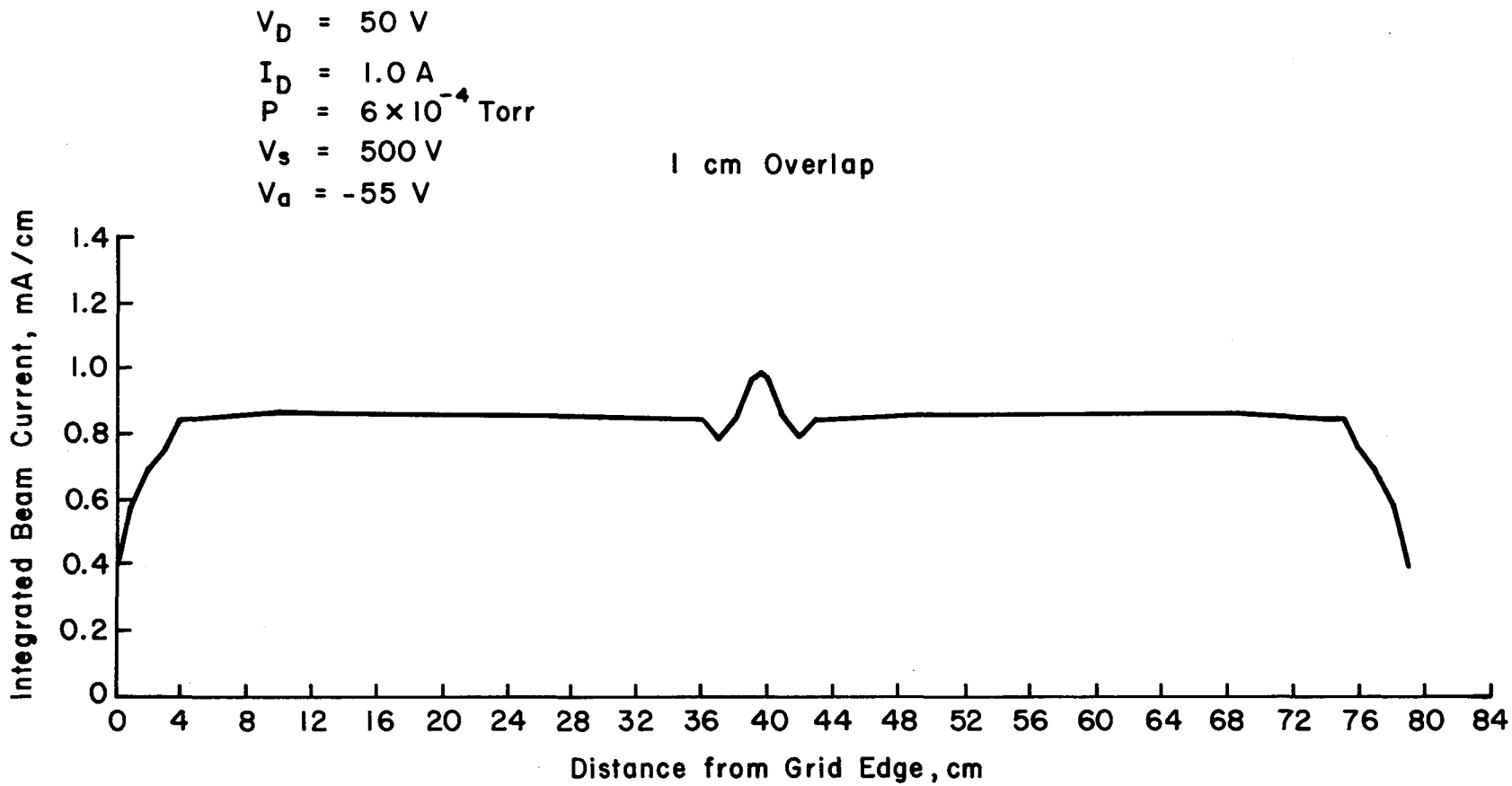

Fig. 5-9. Integrated beam current profile for the best overlap position at 6×10^{-4} Torr and R = 0.90.

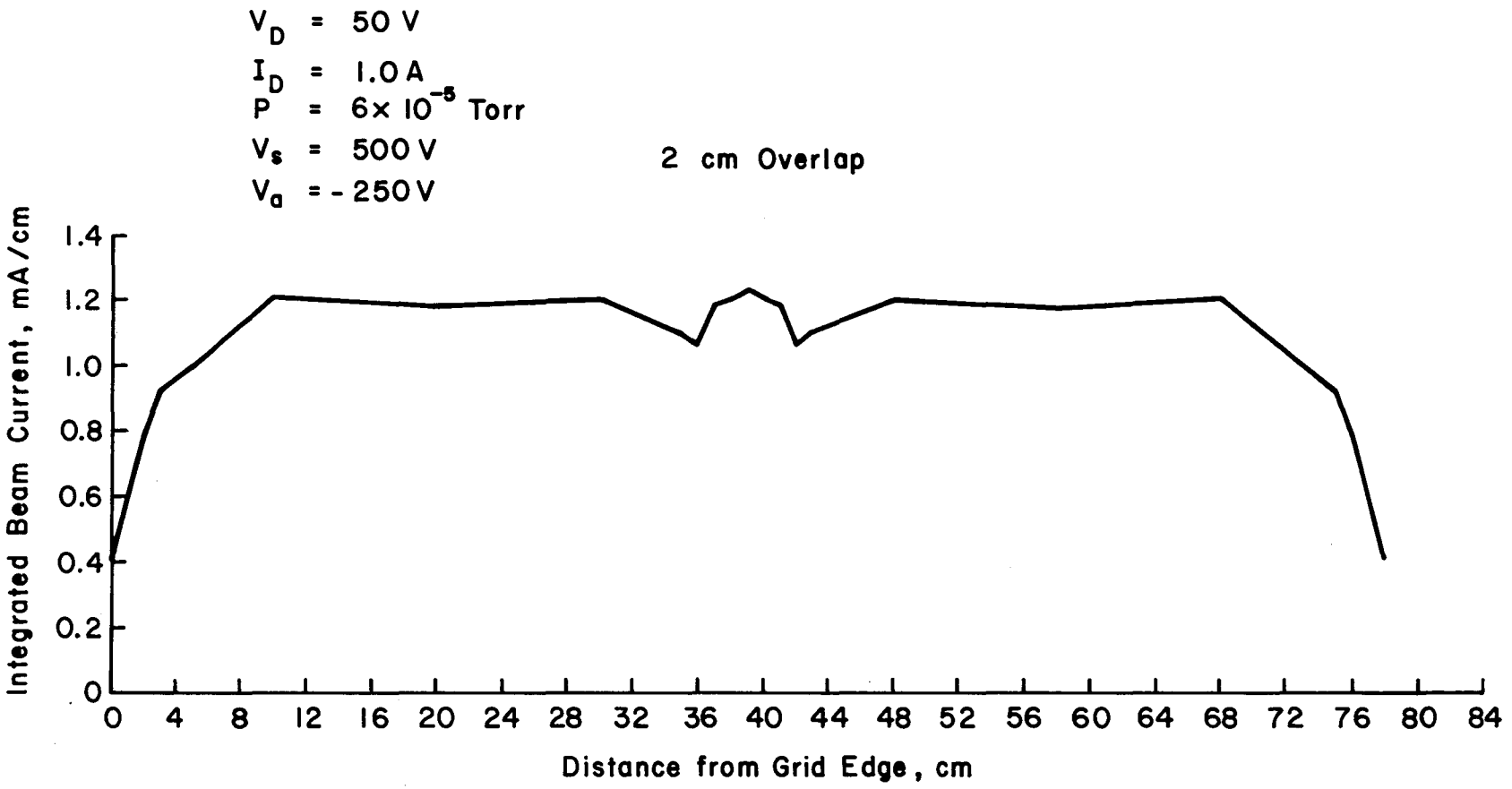

Fig. 5-10. Integrated beam current profile for the best overlap position at 6×10^{-5} Torr and R = 0.67.

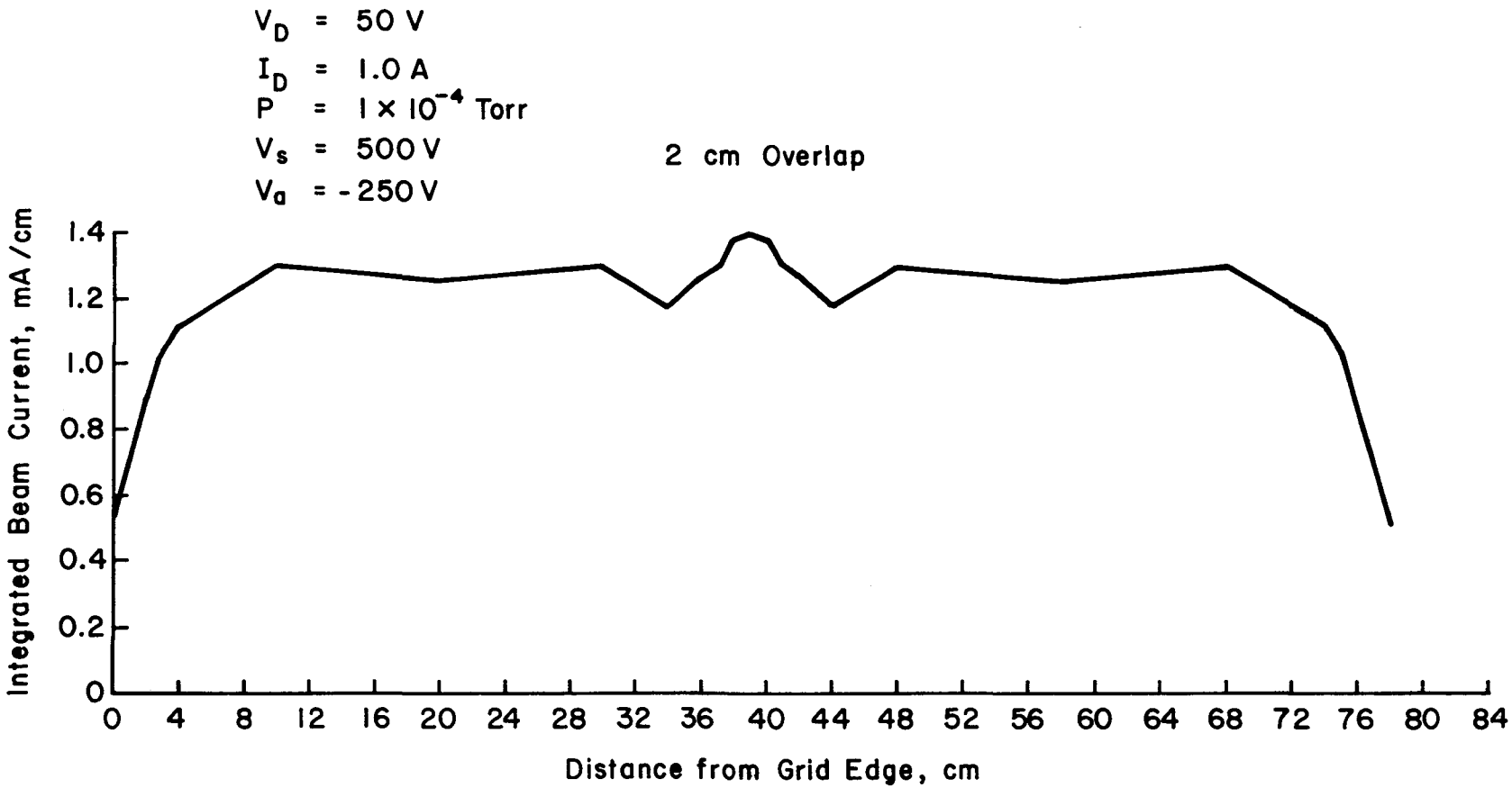

Fig. 5-11. Integrated beam current profile for the best overlap position at 1 × 10^{-4} Torr and R = 0.67.

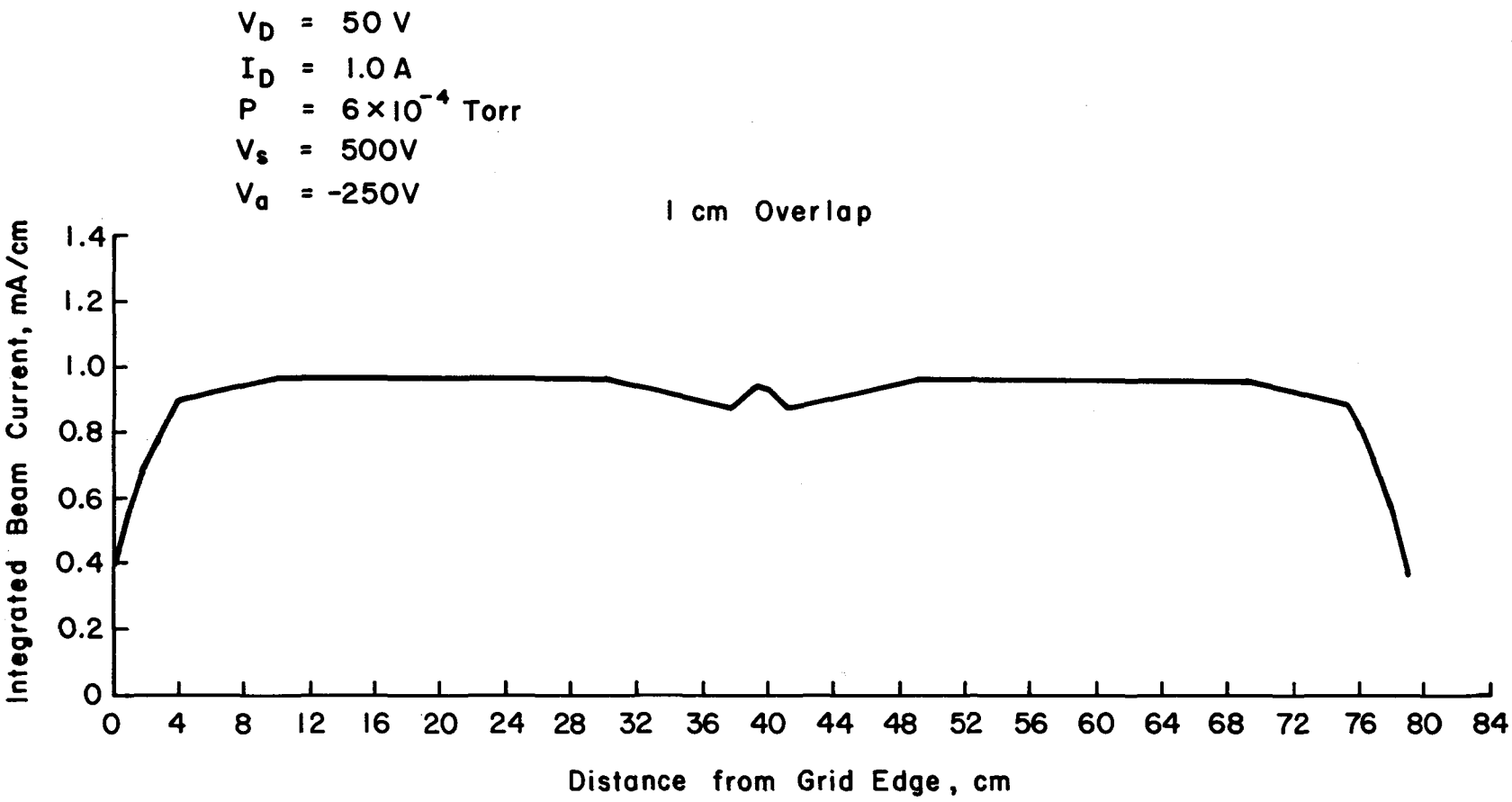

Fig. 5-12. Integrated beam current profile for the best overlap position at 6×10^{-4} Torr and R = 0.67.

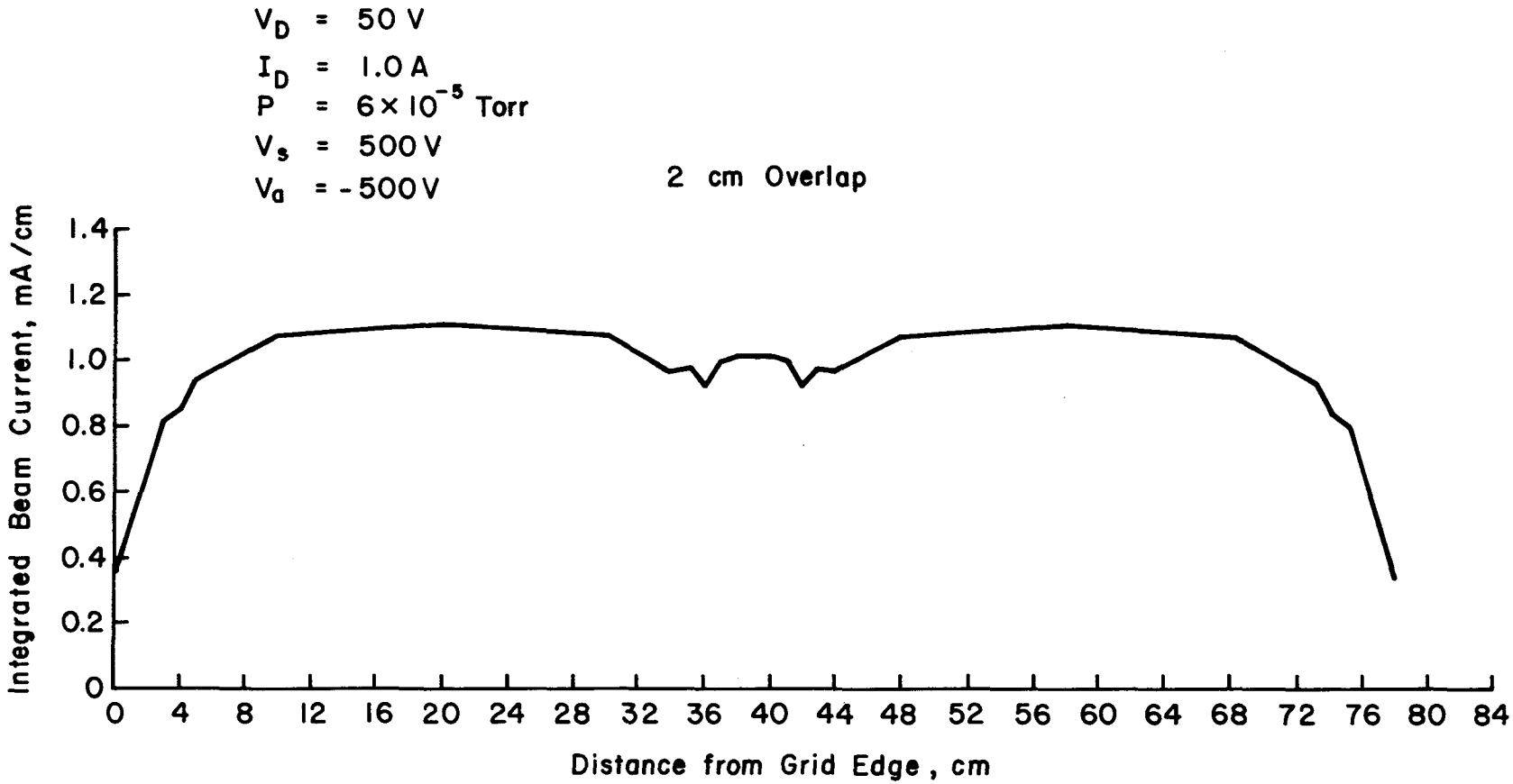

Fig. 5-13. Integrated beam current profile for the best overlap position at 6×10^{-5} Torr and R = 0.50.

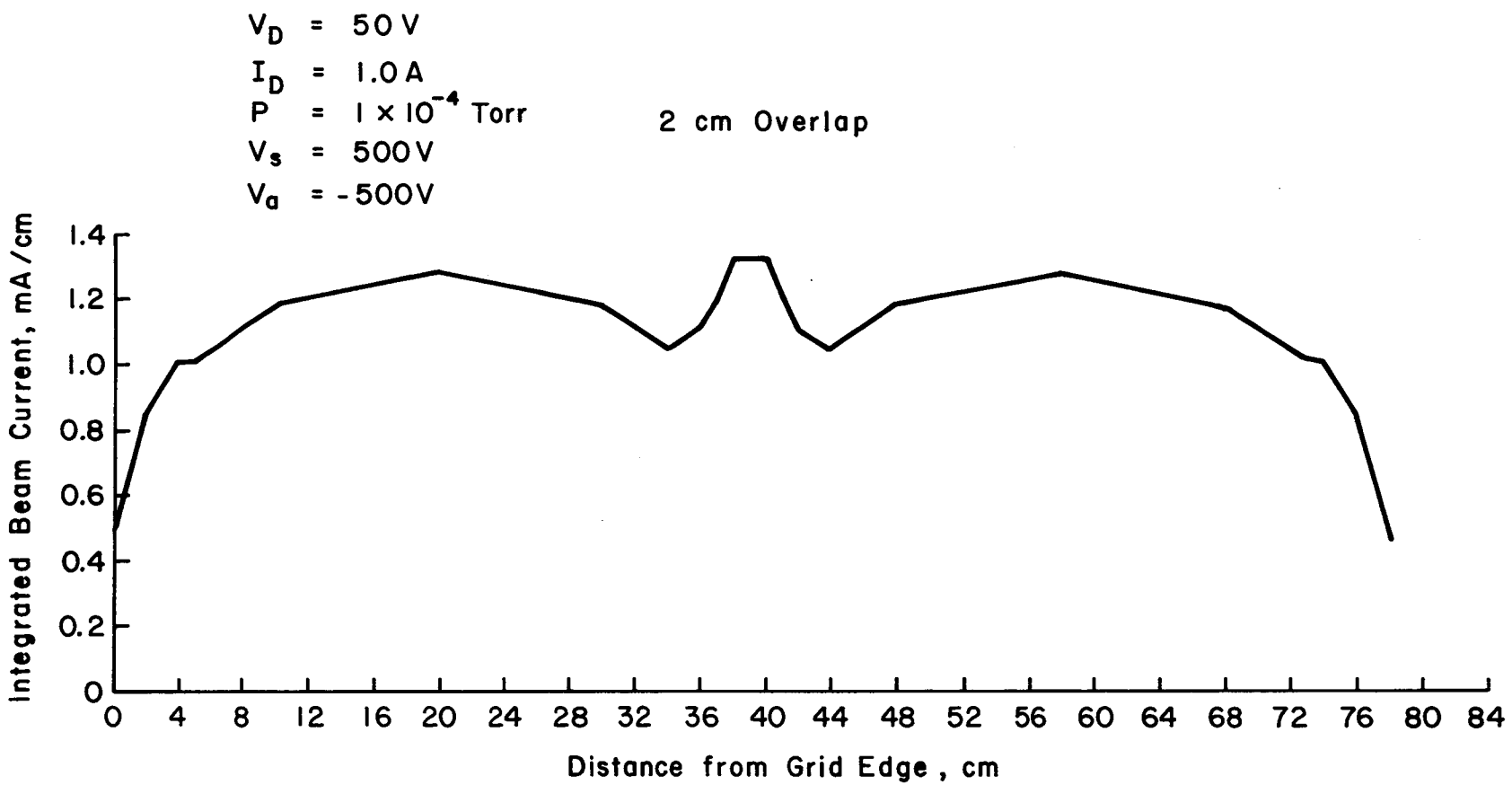

Fig. 5-14. Integrated beam current profile for the best overlap position at 1×10^{-4} Torr and R = 0.50.

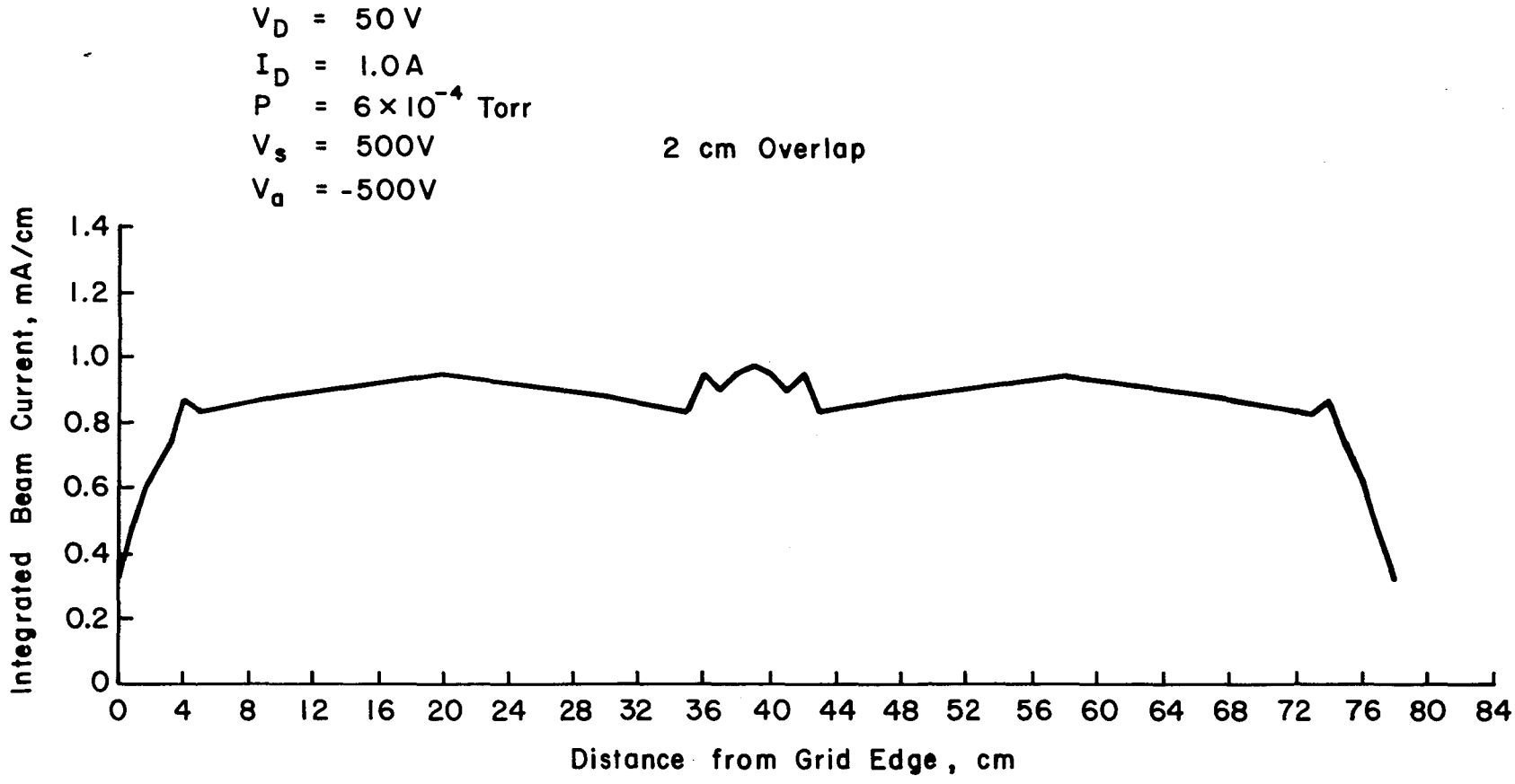

Fig. 5-15. Integrated beam current profile for the best overlap position at 6×10^{-4} Torr and R = 0.50.

Returning to Table 5-1, the optimum overlap ranges from 0-2 cm. This small amount of overlap suggests that the beam has a high degree of uniformity at the ion optics. Lengthening the discharge chamber beyond the 45 cm used herein would move the discharge-chamber end walls farther from the ends of the ion beam. This lengthening would be expected to improve uniformity at the ion optics, hence reduce the optimum overlap distance. But, as indicated, the nonuniformity obtained with the design tested was not felt to be a serious problem.

The data presented in this section were not corrected for charge exchange. The integrated beam current at the survey plane (10 cm from ion source) was less than the ion beam current measured at the ion source by the factors 0.855, 0.778, and 0.434 for 0.6, 1.0, and 6.0×10^{-4} Torr. For inert gas sputtering, for example, the energetic neutrals are about as effective as ions. The integrated values in Figs. 5-7 through 5-15 should therefore be divided by the above factors to obtain a measure of the sputtering capability.

IV. CONCLUSION

A rectangular-beam ion source was designed and fabricated. A multipole magnetic field configuration was used to facilitate design of the modular rectangular chamber, while a three-grid ion optics system was used for increased ion current densities.

For the multipole chamber, a magnetic integral of 5.6×10^{-5} Tesla-m was used to contain the primary electrons. This integral value was reduced from the initial design value, with the reduction found necessary for discharge stability. The final value of magnetic integral resulted in discharge losses at typical operating conditions which ranged from 600 to 1000 eV/ion, in good agreement with the design value of 800 eV/ion.

The beam current density at the ion optics was limited to about 3.2 mA/cm^2 at 500 eV and to about 3.5 mA/cm^2 at 1000 eV. The design value of 6 mA/cm^2 at 500 eV was not achieved. Some reduction from optimum is usually expected for large ion optics, due to both nonuniform ion current and tolerance effects over the large beam dimensions. The large reduction from 6 to 3.2-3.5 mA/cm^2 probably indicates additional effects due to grid thermal warping which tended to increase accelerator and decelerator grid impingment currents and grid arcing. The current densities of 3.2 and 3.5 mA/cm^2 were obtained at net-to-total voltage ratios of 0.33 and 0.67. The larger current density at 1000 eV and R = 0.67 was close to an impingement limit, but was actually limited by the accelerator power supply capability.

The use of multiple rectangular-beam ion sources to process wider areas than would be possible with a single source was also studied. Beam profiles were surveyed at a variety of operating conditions and

the results of various amounts of beam overlap calculated. In all cases investigated a very uniform ion beam resulted with the most uniform coverage being obtained using a 0-2 cm overlap. The maximum departure from uniform processing at optimum overlap was found to be ±15%. This small departure was felt to be very good for a chamber length of 45 cm. If a higher degree of uniformity is required in the long dimension the chamber could be made longer to decrease end affects.

APPENDIX

The discharge chamber plasma was probed using a moveable electrostatic (Langmuir) probe to determine plasma properties as a function of operating conditions. The probe was moved parallel to the ion optics along the center of the chamber at a distance of 2.4 cm from the screen grid. Plasma potential, Maxwellian electron density and temperature and primary electron density and temperature were determined at 2 cm intervals from the center of the chamber to one end. The plasma potential averaged 6.6 V positive to the anode potential for an electron temperature of 8.5 eV. The primary electron density averaged about 5.3 percent of the plasma density with an average energy of 42 eV. The plasma density as a function of position is shown in Fig. A-1. The density is quite uniform as expected for the field-free region a mutli-pole ion source with some tendency toward diminished density as a cathode potential wall is approached. The beam current density extracted through the accelerator system will reflect the variations in plasma density along the accelerator system. Extracted beam current density was measured using a moveable Faraday cup. The beam current density profile shown in Fig. 4-15 exhibits the same qualitative trends as the plasma density measured inside the chamber.

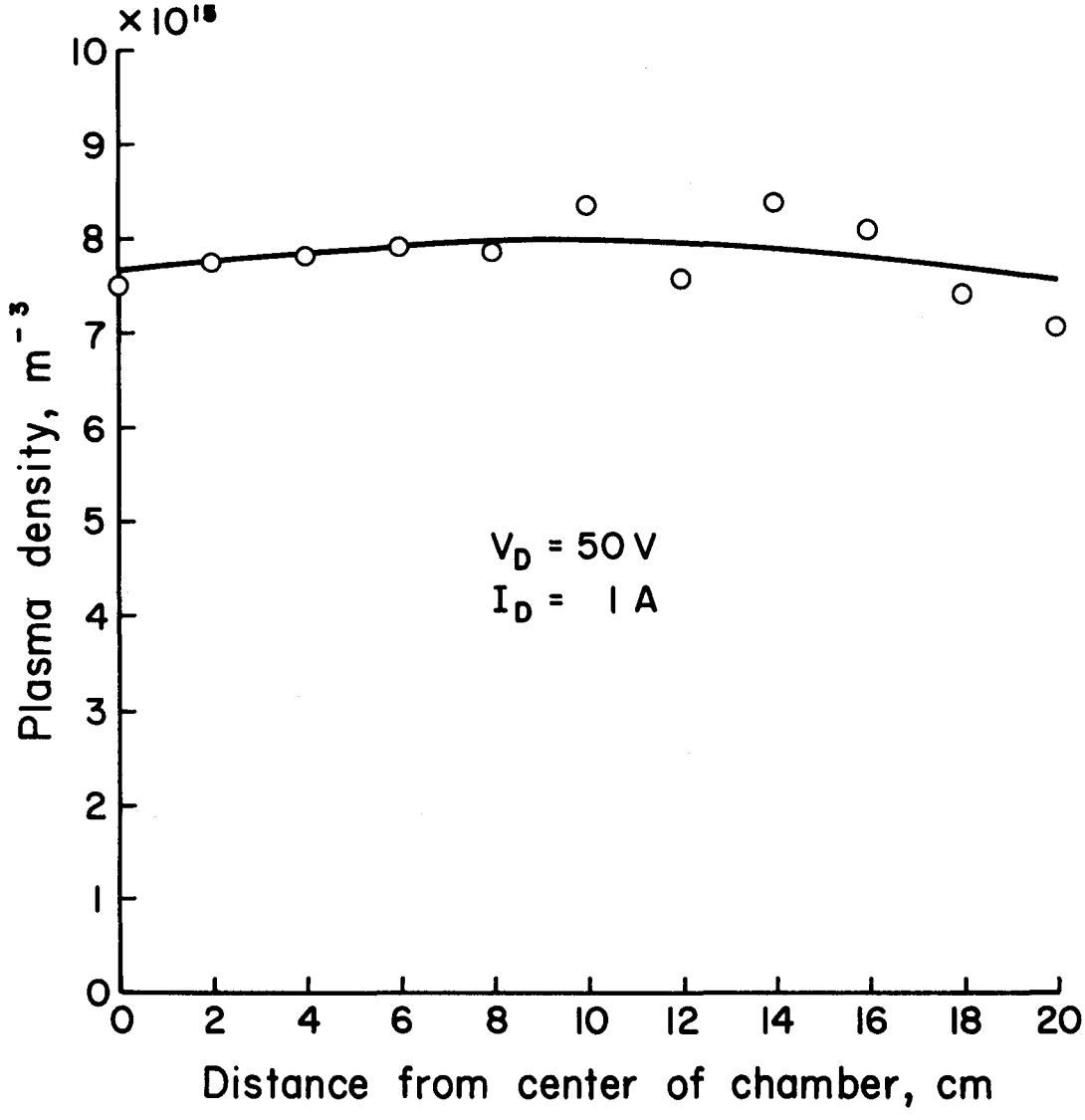

Fig. A-1. Plasma density inside operating rectangular ion source as a function of distance from the center of the chamber.

REFERENCES

1. H. R. Kaufman, "Technology of Ion Beam Sources Used in Sputtering," J. Vac. Sci. Technol., Vol. 15, No. 2, March/April 1978.

2. H. R. Kaufman, "Industrial Ion Source Technology," NASA Contr. Report CR-135353, Nov. 1977.

3. G. C. Isaacson, "Multipole Gas Thruster Design," NASA Contr. Report CR-135101, pp. 60-75, June 1977.

4. R. S. Robinson, "Thirty CM Ion Source," in Ind. Ion Source Tech. (H. R. Kaufman, ed.), NASA Contr. Report CR-135149, pp. 1-59, Nov. 1976.

5. H. R. Kaufman, "Accelerator System Solutions for Electron Bombardment Ion Sources," AIAA Paper #75-430, Mar. 1975.

6. G. Aston and H. R. Kaufman, "The Ion-Optics of a Two-Grid Electron-Bombardment Thruster," AIAA Paper 76-1029, Nov. 1976.

7. G. Aston and H. R. Kaufman, "Ion Beam Divergence Characteristics of Three-Grid Accelerator Systems," AIAA Paper 78-669, Apr. 1978.

8. G. Aston, "Ion Extraction from a Plasma," NASA Contr. Report CR-159849, June 1980.

9. H. R. Kaufman and R. S. Robinson, "Industrial Ion Source Technology," NASA Contr. Report CR-159877, Dec. 1979.

10. N. Laegreid and G. K. Wehner, J. Appl. Phys., Vol. 32, pp. 365-369 (1961).

11. A. L. Southern, W. R. Willis, and M. T. Robinson, J. Appl. Phys., Vol. 34, pp. 153-163 (1963).

12. H. R. Kaufman, "Technology of Electron-Bombardment Ion Thrusters," in Advances in Electronics and Electron Physics, Academic Press, 1974.

13. H. R. Kaufman and R. S. Robinson, "Inert Gas Thrusters," NASA Contr. Report CR-159813, Nov. 1979.

14. G. C. Isaacson, "Multipole Gas Thruster Design," NASA Contr. Report CR-135101, June 1977.

15. R. S. Robinson, "Physical Processes in Directed Ion Beam Sputtering," NASA Contr. Report CR-159567, March 1979.

16. J. R. Beattie, "Cusped Magnetic Field Mercury Ion Thruster," NASA Contr. Report CR-135047, July 1976.

17. H. R. Kaufman and A. J. Cohen, "Maximum Propellant Utilization in an Electron-Bombardment Thruster," in Proc. Symp. Ion Sources and Form. Ion Beams (Th. J. M. Sluyters, ed.), pp. 61-68, Brookhaven Nat. Lab. (Oct. 1971).

18. H. R. Kaufman, "Ion-Thruster Propellant Utilization," Ph.D. Thesis, Colorado State University, June 1971.

19. D. Bohm, "Minimum Ionic Kinetic Energy for a Stable Sheath," in The Characteristics of Electrical Discharges in Magnetic Fields," (A. Guthrie and R. K. Wakerling, ed.), McGraw-Hill Book Co., Inc., pp. 77-86, (1949).

20. T. D. Masek, "Plasma Characteristics of the Electron Bombardment Ion Engine," Jet Propulsion Lab., Calif. Inst. Tech. TR-32-1271, 1968.

21. S. S. Attwood, Electric and Magnetic Fields, Dover Publishing, Inc., New York, 1967.

22. G. Aston, "Ion Beam Divergence Characteristics of Two-Grid Accelerator Systems," in Mercury Ion Thruster Research-1977 (P. J. Wilbur, ed.), NASA Contr. Report CR-135317, pp. 1-41, Dec. 1977.

23. G. Aston, "Ion Beam Divergence Characteristics of Three-Grid Accelerator Systems," in Mercury Ion Thruster Research-1977 (P. J. Wilbur, ed.), NASA Contr. Report CR-135317, pp. 42-60, Dec. 1977.

DISTRIBUTION LIST

	Copies
National Aeronautics and Space Administration Washington, DC 20546	
Attn: RS/Mr. Dell Williams, III	1
RTS-6/Mr. Wayne Hudson	1
RTS-6/Mr. Jerome Mullin	1
MT/Mr. Ivan Bekey	1
National Aeronautics and Space Administration Lewis Research Center 21000 Brookpark Road Cleveland, OH 44135	
Attn: Research Support Procurement Section	
Mr. G. Golinski, MS 500-306	1
Technology Utilization Office, MS 3-19	1
Report Control Office, MS 5-5	1
Library, MS 60-3	2
Mr. N. Musial, MS 500-113	1
Dr. M. Goldstein, Chief Scientist, MS 5-3	1
Mr. T. Cochran, MS 501-8	1
Mr. D. Petrash, MS 501-5	1
Mr. N. Grier, MS 501-7	1
Mr. M. Mirtich, MS 501-7	1
Mr. R. Finke, MS 77-4	1
Mr. B. Banks, MS 501-7	1
Mr. D. Byers, MS 501-7	1
Mr. W. Kerslake, MS 501-7	30
National Aeronautics and Space Administration Lyndon B. Johnson Space Center Houston, TX 77058	
Attn: Mr. Hu Davis	1
National Aeronautics and Space Administration Marshall Space Flight Center Huntsville, AL 35812	
Attn: Mr. Jerry P. Hethcoate	1
Mr. John Harlow	1
Mr. John Brophy	1
Mr. Robert T. Bechtel	1
NASA Scientific and Technical Information Facility P.O. Box 8757 Baltimore, MD 21240	
Attn: Accessioning Department	1

National Aeronautics and Space Administration
Goddard Space Flight Center
Greenbelt, MD 20771
Attn: Mr. W. Isley, Code 734 1
Mr. A. A. Vetman 1
Dr. David H. Suddeth 1

National Aeronautics and Space Administration
Ames Research Center
Moffett Field, CA 94035
Attn: Technical Library 1

National Aeronautics and Space Administration
Langley Research Center
Langley Field Station
Hampton, VA 23365
Attn: Technical Library 1
Mr. B. Z. Henry 1

The Aerospace Corporation
P.O. Box 95085
Los Angeles, CA 90045
Attn: Dr. B. A. Haatunion 1
Mr. A. H. Silva 1

The Aerospace Corporation
Space Sciences Laboratory
P.O. Box 92957
Los Angeles, CA 90009
Attn: Dr. Y. T. Chiu 1

Bell Laboratories
600 Mountain Avenue
Murray Hill, NJ 07974
Attn: Dr. Edward G. Spencer 1
Dr. Paul H. Schmidt 1

Boeing Aerospace Company
P.O. Box 3999
Seattle, WA 98124
Attn: Mr. Donald Grim, MS 8K31 1
Mr. Russell Dod 1

Case Western Reserve University
10900 Euclid Avenue
Cleveland, OH 44106
Attn: Dr. Eli Reshotko 1

C.E.N.-F.A.R.
Service Du Confinement Des Plasmas
BP6
92260 Fontenay-Aux-Roses,
FRANCE
Attn: J. F. Bonnal 1

Circuits Processing Apparatus, Inc.
725 Kifer Road
Sunnyvale, CA 94086
Attn: Spencer R. Wilder 1

Commonwealth Scientific Corporation
500 Pendleton Street
Alexandria, VA 22314
Attn: George R. Thompson 1

Computing Center of the USSR Academy of Sciences
Vavilova 40
117333 Moscow, B-333
USSR
Attn: Dr. V. V. Zhurin 1

Comsat Corporation
950 L'Enfant Plaza, S.W.
Washington, DC 20024
Attn: Mr. Sidney O. Metzger 1

COMSAT Laboratories
P.O. Box 115
Clarksburg, MD 20734
Attn: Mr. B. Free 1
Mr. O. Revesz 1

CVC Products
525 Lee Road
P.O. Box 1886
Rochester, NY 14603
Attn: Mr. Georg F. Garfield, Jr. 1

DFVLR - Institut fur Plasmadynamik
Technische Universitat Stuttgart
7 Stuttgart-Vaihingen
Allmandstr 124
WEST GERMANY
Attn: Dr. G. Krulle 1

DFVLR - Institut fur Plasmadynamik
33 Braunschweig
Bienroder Weg 53
WEST GERMANY
Attn: Mr. H. Bessling 1

EG & G Idaho
P.O. Box 1625
Idaho Falls, ID 83401
Attn: Dr. G. R. Longhurst, TSA-104 1

Electro-Optical Systems, Inc.
300 North Halstead
Pasadena, CA 91107
Attn: Dr. R. Worlock 1
Mr. E. James 1
Mr. W. Ramsey 1

Electrotechnical Laboratory
1-1-4, Umezono, Sakura-Mura,
Niihari-Gun
Ibaraki,
JAPAN
Attn: Dr. Katsuya Nakayama 1

Fairchild Republic Company
Farmingdale, NY 11735
Attn: Dr. Domenic J. Palumbo 1

Ford Aerospace Corporation
3939 Fabian Way
Palo Alto, CA 94303
Attn: Mr. Robert C. Kelsa 1

General Dynamics
Kearney Mesa Plant
P.O. Box 1128
San Diego, CA 92112
Attn: Dr. Ketchum 1

Giessen University
1st Institute of Physics
Giessen,
WEST GERMANY
Attn: Professor H. W. Loeb 1

Hughes Aircraft Company
Space and Communication Group
P.O. Box 92919
Los Angeles, CA 90009
Attn: Dr. M. E. Ellison 1
Dr. B. G. Herron 1

Hughes Research Laboratories
3011 Malibu Canyon Road
Malibu, CA 90265
Attn: Mr. J. H. Molitor 1
Dr. R. L. Poeschel 1
Dr. Jay Hyman 1
Mr. R. Vahrenkamp 1
Dr. J. R. Beattie 1
Dr. W. S. Williamson 1

IBM Corporation
Thomas J. Watson Research Center
P.O. Box 218
Yorktown Heights, NY 10598
Attn: Dr. Jerome J. Cuomo 1
Dr. James M. E. Harper 1

IBM East Fishkill
D/42K, Bldg. 300-40F
Hopewell Junction, NY 12533
Attn: Mr. James Winnard 1

Ion Beam Equipment, Inc.
P.O. Box 0
Norwood, NJ 07648
Attn: Dr. W. Laznovsky 1

Ion Tech, Inc.
P.O. Box 1388
1807 E. Mulberry
Fort Collins, CO 80522
Attn: Dr. Gerald C. Isaacson 1

Jet Propulsion Laboratory
4800 Oak Grove Drive
Pasadena, CA 91102
Attn: Dr. Kenneth Atkins 1
Technical Library 1
Mr. Eugene Pawlik 1
Mr. James Graf 1
Mr. Dennis Fitzgerald 1
Dr. Graeme Aston 1

Joint Institute for Laboratory Astrophysics
University of Colorado
Boulder, CO 80302
Attn: Dr. Gordon H. Dunn 1

Kirtland Air Force Base
Office of Assistant for Study Support
Albuquerque, NM 87117
Attn: Dr. Berhart Eber OAS Ge 1

Kyoto University
The Takagi Research Laboratory
Department of Electronics
Yoshidahonmachi Sakyo-ku
Kyoto 606,
JAPAN
Attn: Dr. Toshinori Takagi 1

Lawrence Livermore Laboratory
Mail Code L-437
P.O. Box 808
Livermore, CA 94550
Attn: Dr. Paul Drake 1

Lockheed Missiles and Space Company
Sunnyvale, CA 94088
Attn: Dr. William L. Owens
Propulsion Systems, Dept. 62-13 1
Mr. Carl Rudey 1

Marshall Spaceflight Center
Huntsville, AL 35812
Attn: M. Ralph Carruth, Jr., MS EC35 1

Massachusetts Institute of Technology
Room 13-3061
77 Massachusetts Avenue
Cambridge, MA 02139
Attn: Henry I. Smith 1

New Mexico State University
Department of Electrical and Computer Engr.
Las Cruces, NM 88003
Attn: Dr. Robert McNeil 1

Optic Electronics Corporation
11477 Pagemill Road
Dallas, TX 75243
Attn: Bill Hermann, Jr. 1

Physicon Corporation
221 Mt. Auburn Street
Cambridge, MA 02138
Attn: H. von Zweck 1

Princeton University
Princeton, NJ 08540
Attn: Mr. W. F. Von Jaskowsky 1
Dean R. G. Jahn 1
Dr. K. E. Clark 1

Research and Technology Division
Wright-Patterson AFB, OH 45433
Attn: (ADTN) Mr. Everett Bailey 1

Rocket Propulsion Laboratory
Edwards AFB, CA 93523
Attn: LKDA/Mr. Tom Waddell 1
LKDH/Dr. Robert Vondra 1

Royal Aircraft Establishment
Space Department
Farnborough, Hants
ENGLAND
Attn: Dr. D. G. Fearn 1

Sandia Laboratories
Mail Code 5743
Albuquerque, NM 87115
Attn: Mr. Ralph R. Peters 1

Tektronix, 50-324
P.O. Box 500
Beaverton, OR 97077
Attn: Curtis M. Haynes 1

Texas Instruments, Inc.
MS/34
P.O. 225012
Dallas, TX 75265
Attn: Larry Rehn 1

TRW Inc.
TRW Systems
One Space Park
Redondo Beach, CA 90278
Attn: Dr. M. Huberman 1
Mr. H. Ogawa 1
Mr. Sid Zafran 1

United Kingdom Atomic Energy Authority
Culham Laboratory
Abingdon, Berkshire
ENGLAND
Attn: Dr. P. J. Harbour 1
Dr. M. F. A. Harrison 1
Dr. T. S. Green 1

University of Tokyo
Department of Aeronautics
Faculty of Engineering
7-3-1, Hongo, Bunkyo-ku
Tokyo,
JAPAN
Attn: Prof. Itsuro Kimura 1

Veeco Instruments, Inc.
Terminal Drive
Plainview, NY 11803
Attn: Norman Williams 1